Study on the structure formation and transport properties of nanoparticulate, nanoporous media using particle-based stochastic methods

Cumulative Doctoral Thesis
(Kumulative Dissertation)
to be awarded the degree of
Doctor of Engineering
(Dr.-Ing.)

Submitted by
Hector Fernando
Rusinque Olaya
from Bogota, Colombia

approved by the Faculty of Mathematics/Computer Science and
Mechanical Engineering,
Clausthal University of Technology

Date of oral examination
Nov. 15, 2021

Dean: Prof. Dr. J. P. Müller

Chairperson of the Board of Examiners: Prof. Dr.-Ing. Thomas Turek

Supervising Tutor: Prof. Dr.-Ing. Gunther Brenner

Reviewer: Prof. Dr. rer. nat. Alfred Weber

Reviewer: Jun.-Prof. Dr. Nina Merkert (geb. Gunkelmann)

Acknowledgements

First, I would like to thank my supervisors, Professor Gunther Brenner, Professor Alfred Weber as well as Junior Professor Nina Gunkelmann, whose expertise was invaluable in formulating the research questions and methodology.

I would also like to thank my colleagues Eugenia Barthelmie, Helena Fedianina, and Aurina Martinez for their immense support and feedback as co-authors on the publications. Of course, I cannot be more grateful to Heidi Andresen-Tanumihardja, who always assisted me and did not let me forget my organizational duties.

I could not have made this long journey without the unconditional support of my dear parents and my lovely, annoying siblings. Finally, I would like to thank my beloved wife, Juliana Rivas Botero, for her stimulating discussions, wise advice and sympathetic ear. You are always there for me.

Abstract

Porous materials are used in several technical applications such as filtration, engineering, geosciences and biophysics. This work focuses on the modeling of mass transport phenomena occurring in the pore network and during the formation of nanoparticulate nanoporous clusters using particle-based stochastic methods. Traditionally, macroscopic quantities such as the porosity and tortuosity [1] are used in models as average global parameters to estimate the transport properties of porous media. However, these macroscopic approaches fail to quantify the influence of structural heterogeneities of the medium on mass transport phenomena. This effect can be taken into account by resolving the computational domain on the pore-scale, as it is done in particle-based approaches [2, 3]. One of the advantages of particle-based methods is their efficient use on modern multicore hardware architectures due to their good scalability [4, 5]. In this thesis, a Brownian dynamics solver used to model the motion of tracers in porous media was developed and optimized for parallel computing using the OpenMP and MPI libraries. A further particle-based model used, known as fast lubrication dynamics, is implemented in the open-source software LAMMPS. With the help of this software, the motion of colloidal nanoparticles is modeled. For this purpose, a customized pairwise interaction modeling screened Coulomb forces between particles had to be developed. In addition, different external fields (e.g. velocity fields, electric fields, pressure fields, etc.) are computed using open-source applications such as Fenics and an in-house lattice Boltzmann solver in order to evaluate their influence on the motion of nanoparticles or tracers.

In this work, mass transport phenomena in porous media are addressed, where the effect of heterogeneities in the porous structure and the hindering effect of narrow pores on the mass transport properties of the aforementioned media are studied. Among the main achievements of this work is the development of a particle-based model capable of computing the diffusivity of nanoporous media. In addition, the formation and structure properties of nanoparticulate clusters are investigated. One of the highlights of this study is a proposed formation mechanism of nanoparticulate clusters produced via spray-drying.

Contents

1 Introduction 1

1.1 Publication 1: Confinement effect on the mass transport properties and porous structure of porous media . . . 6

1.2 Publication 2: Hindering effect of pore size on the mass transport properties of porous media . . . 6

1.3 Publication 3: Effect of electric forces on the formation of nanoparticulate, nanoporous clusters via spray-drying . . . 11

1.4 Publication 4: Effect of an external electric field on the formation of nanoparticulate, nanoporous clusters via electro deposition . . . 11

2 Theory and Methods 13

2.1 Fundamentals of diffusion . . . 13

2.1.1 Transport diffusion and self-diffusion . . . 13

2.2 External fields: Velocity field . . . 16

2.2.1 Liouville's equation . . . 16

2.2.2 Boltzmann equation . . . 16

2.2.3 Lattice Boltzmann Method . . . 19

2.2.4 Calculation of macroscopic quantities . . . 21

2.2.5 NavierStokes equations . . . 21

2.3 External fields: Electric field . . . 22

2.3.1 Hard-sphere-like colloids . . . 24

3 Confinement effects on mass transport and packing arrangement 27

3.1 German abstract . . . 27

3.2 Abstract . . . 29

3.3 Introduction . . . 29

3.4 Modeling and numerical approach . . . 30

3.4.1 Computation of the velocity field . . . 30

3.4.2 Computation of the mass transport . . . 31

3.5 Results and discussion . . . 35

3.5.1 Mass transport in homogeneous porous media: Comparison of the MVA and BD approaches . . . 35

3.5.2 Mass transport in heterogeneous porous media: Confinement effects 39

3.6 Conclusions 43

4 Hindering effect of pore size on mass transport in porous media 47

4.1 German abstract 47

4.2 Abstract 48

4.3 Introduction 49

4.4 Modeling and Numerical Approach 50

4.4.1 Equation of Motion of a Particle Ensemble: Mass Transport in Pores 50

4.4.2 Multiscale Numerical Approach 62

4.5 Conclusions 68

4.6 Notation 70

5 Effect of electric forces on the formation of nanoparticulate clusters 71

5.1 German abstract 71

5.2 Abstract 72

5.3 Introduction 72

5.4 Results and Discussion 74

5.4.1 Clusters of hard-sphere-like silica NPs 76

5.4.2 Clusters produced in two evaporation stages: Effect of the electric forces 80

5.5 Conclusions 86

5.6 Numerical and experimental methods 87

5.7 Methods 87

5.7.1 Materials 87

5.7.2 Characterization 87

5.7.3 Particle simulation 88

5.8 Supporting information 90

5.8.1 Simulation details 90

5.8.2 Materials characterization 91

5.8.3 Electric potential 91

6 Effect of an electric field on the formation of nanoparticulate clusters 95

6.1 German abstract 95

6.2 Abstract 96

6.3 Introduction 97

6.4 Modeling and numerical approach 98

6.5 Results and discussion 101

6.5.1 Verification 102

6.5.2 Effect of size and charge of the nanoparticles 104
6.5.3 Effect of the electric field: Variation of the potential difference . . 105
6.5.4 Effect of the electric field: Changes due to geometry modifications 105
6.5.5 Dimensional analysis 107
6.6 Conclusions 112
6.7 Notation 113

7 Final discussion and conclusions 115

8 Outlook 119

List of Figures 121

List of Tables 127

129

1 Introduction

Porous materials have a wide range of applications in practice. All applications of these materials are based on their property of being traversed by cavities or pores, and thus providing a large fluid/solid interface per unit volume. Therefore, porous systems are used e.g. in adsorption processes, gas-solid reactions or in heterogeneous catalysis. For heterogeneous catalysis, the catalytically active components are usually applied to the inner surface of porous substrates. It is at these reactive centers that the conversions of reactants to products take place. Apart from the reaction kinetics, the mass transport of the components to and from these catalytic sites plays an important role in the overall kinetics of the heterogeneously catalyzed reaction. This mass transport is influenced to a considerable extent by the pore structure of the porous medium.

Due to the complex structure of engineered porous materials, an exact prediction of the mass transport through the pore system is infeasible. Experimental methods for its determination are very time-consuming and labor-intensive, so that attempts are often made to estimate the mass transport on the basis of more easily accessible characteristic quantities of the porous materials. In this context, the porosity and the pore size are the focus of interest. However, the experimental methods for determining these quantities usually require simplified models of the porous structure in order to be able to evaluate the measurement results.

When manufacturing porous materials for chemical reaction engineering, it is essential to provide sufficient surface area for the catalyzed reaction or for the adsorption process. Moreover, the reactants should be able to reach the reactive centers as quickly as possible, i.e. the diffusive mass transport inside the porous materials should be optimized. For the optimization of the manufacture of such materials, there is therefore great interest in procedures for characterizing the pore structure and in methods for determining the influence of this structure on mass transport.

Previous attempts to estimate the influence of the pore structure on mass transport have been made using model systems to describe porous materials on the basis of experimentally determined values for the porosity and the pore size distribution. Pore systems have often been assumed to be cylindrical capillaries with different spatial arrangements. The parallel pore model describes the cavity of porous materials as a bundle of parallel capillaries with uniform and constant radius. This idea has been extended with the addition of a distribution of capillary diameters corresponding to the experimentally determined pore size distribution,[6] as well as with a random orientation of the capillaries,[7] and the introduction of converging and diverging capillaries.[8]

An alternative method of modeling porous materials consists of replicating the solid material instead of the pore space. For this purpose, clusters of spheres have often been numerically generated, whose porosity and/or particle size distribution match those of the porous material of interest. The resulting pore geometry is irregular and thus no longer easily describable. The porous media hereby considered are mostly sphere packings, i.e. clusters of spherical particles, which are packed into compact arrangements. If a sphere packing is randomly formed, two characteristic regions can be identified according to their structural order degree. While a highly ordered, structured arrangement dominates the region near to the boundaries of the structure, a random unstructured arrangement predominates in the inner bulk region of the structure far away from the packing boundaries. The presence of these two regions with different porous structures introduces a further challenge in both the characterization and modeling of such heterogeneous porous media. On the one hand, a porous medium can be characterized, for instance, by its porosity or transport properties such as permeability, tortuosity and diffusive hindrance (a measure of the inhibition of diffusion due to finite size effects). However, the characterization of porous materials is usually complex, since their intrinsic transport properties correlate strongly with the intricate pore structure of the medium. On the other hand, continuous models, which consider porous materials as effective media, use global properties as descriptors for the modeled material. Particle-based methods have been used to simulate particle trajectories in order to determine the mass transport properties of the porous structure.

Nanoporous materials are of particular interest for this work, as they offer exceptional catalytic properties due to their large surface area to volume ratio. This can be exploited to increase the catalytic activity of a material in heterogeneous catalysis, since the number of active sites, at which the desired reaction takes place, increases. However, if the pore size narrows to the same order of magnitude as the molecule size, the mobility of the molecules becomes dramatically hindered. This slows down the overall kinetics of the catalysis as the reactants can hardly reach the active sites inside the porous structure and the products can barely escape the intricate and narrow pore network. Thus, when designing a catalytic nanoporous material, a pore size has to be chosen so that a balance/compromise is maintained between the associated surface-to-volume ratio and the mobility of the molecules. A further strategy to address hindered mass transport induced by narrow pore sizes is to reduce the fraction of nanopores by using a hierarchical-porous structure. In this way, the larger pores serve as transport channels for the diffusing molecules to reach the narrower reaction pores faster.[9–11] In the case of adsorption applications, hindered mass transport phenomena can be utilized to capture and remove pollutants such as CO_2 and HCl from a gas or liquid mixture with the help of a nanoporous medium such as zeolites .[12]

---

[6] H. W. HAYNES JR. & L. F. BROWN. *AIChE Journal*, **17**: 491–494, 1971.

[7] MARVIN F.L. JOHNSON & WARREN E. STEWART. *J. of Catalysis*, **4**: 248–252, 1965.

[8] RICHARD N. FOSTER & JOHN B. BUTT. *AIChE Journal*, **12**: 180–185, 1966.

In this work, mass transport processes occurring during the formation of porous structures and within their pore network are modeled using particle-based stochastic approaches. Stochastic methods such as Langevin dynamics, Brownian dynamics and fast lubrication dynamics used in the present study are based on classical Newtonian dynamics with the addition of a random force, which is used to reproduce Brownian motion. Although these particle-based techniques are computationally more complex in comparison to continuum approaches, they enable us to spatially resolve local heterogeneities that play an important role in mass transport processes. This also allows us to couple different kind of fields or pairwise interactions together in the same model in a rather straightforward way by superposition. For instance, external fields such as a bulk velocity field or an electric field are computed in a previous step e.g. solving numerically the Navier-Stokes equations or the Boltzmann equation for the flow, and solving the Poisson equation for the electric field. These external fields are given as input for the particle solver, which superimposes them to the stochastic thermal force in order to describe the mass transport of a particle ensemble at a nano-scale.

In order to reduce the time required to generate the results, an algorithm was developed to run the simulations on parallel computers. Parallel computers offer the possibility to distribute the computational work, which is performed on a PC or a workstation on one processor, to several processors and to perform it there in parallel, i.e. simultaneously. The time gain that can be achieved in this way is known as the speed-up. Thus, on high-performance computers, namely the North-German Supercomputing Alliance (HLRN), a considerable time gain can be achieved. However, the maximum speed-up is limited by the communication between the processes for the purpose of data exchange and synchronization as well as by work that cannot be parallelized.

The fundamental condition for the use of a parallel computer is therefore to have parallelizable computational work, so that the work on the respective processor is as independent as possible from the work on the other processors. This condition is fulfilled in the Browninan and Langevin dynamics solvers used in this study, as the simulated particle trajectories depend only on the structure of the porous material and the particle properties. The influence of other particles in the system is taken into account only by the

---

[9] ROBERT GÜTTEL & THOMAS TUREK. *Energy Technol.*, **4**: 44–54, 2016.
[10] LI CHEN et al. *Chem. Eng. J.*, **349**: 428–437, 2018.
[11] JIAN YIN et al. *J. Mater. Chem. A*, **6**: 8441–8448, 2018.
[12] RAVI SHARMA et al. *Chem. Eng. J.*, **381**: 122512, 2020.

Stokes-Einstein relation .[13]

Thus, the above algorithms, which serially simulate a number of particles, were parallelized by having several processors share this number of particles. For this purpose, the so-called master-slave principle was used, i.e. there is one processor (the master) which distributes the work to the other processors and collects the results. Each slave processor takes over the simulation of the flight of a particle. The master is notified by the slave when the simulation is complete and hands over the next particle to the slave for simulation. This ensures that none of the processors used is idle by having to wait for another processor to do its work. The speed gain from this approach is proportional to the number of processors used minus the master. The MPI (Message Passing Interface) programming tool was used to implement this algorithm.

One of the priorities of this study is to use in-house or open-source software. Open-source tools are used to generate random sphere packings (i.e. porous media) as well as to calculate external fields such as electric and velocity fields and to compute mass transport via a continuum model, which constitutes an alternative approach to the particle-based models mainly used in the mass transport calculations carried out.

The main objective of this work is to address the above described issues using particle-based stochastic methods, which can be synthesized in the following overarching scientific question: *How are the structure formation and transport properties of nanoparticulate, nanoporous media affected by changes in pore size, external and pairwise interactions?*

The structure formation and transport properties of nanoparticulate clusters produced by evaporation of aerosols has been studied by several authors.[14–20] Nevertheless, the interactions considered in the numerical models of this work differ from previous works in that, for example, long-range interactions such as electrostatic forces and hydrodynamic interactions (HIs), i.e., forces resulting from momentum transfer between NPs through the solvent, are often not considered in numerical models due to the dramatic increase in computational complexity that they imply.

The above question is approached by studying the effect of confinement and pore size on mass transport, as well as the effect of pairwise electric interactions (i.e. electric forces) and an external electric field on the formation of nanoparticulate, nanoporous media as follows

---

[13] A. Einstein. *Ann. d. Phys.*, **322**: 549–560, 1905.
[14] M. Mezhericher et al. *Chem. Eng. Sci.*, **66**: 884–896, 2011.
[15] Michael P. Howard et al. *J. Chem. Phys.*, **149**: 094901, 2018.
[16] Katarzyna Jabłczyńska et al. *Adv. Powder Technol.*, **29**: 3542–3551, 2018.
[17] Sabrina Zellmer et al. *ACS Nano*, **9**: 10749–10757, 2015.
[18] Thomas Breinlinger et al. *J. Am. Ceram. Soc.*, **98**: 1778–1786, 2015.
[19] Thomas Breinlinger et al. *Powder Technol.*, **283**: 1–8, 2015.
[20] Wendong Liu et al. *ACS Nano*, **13**: 4972–4979, 2019.

- Publication 1: Confinement effect on the mass transport properties and porous structure of porous media.

- Publication 2: Hindering effect of pore size on the mass transport properties of porous media.

- Publication 3: Effect of electric forces on the formation of nanoparticulate, nanoporous clusters via spray-drying.

- Publication 4: Effect of an external electric field on the formation of nanoparticulate, nanoporous clusters via electro deposition.

Here, Brownian dynamics (BD) are used to model mass transport within the pore network of a particulate cluster. The model is presented in the first publication, where the confinement effect on the packing process of a cluster is also addressed. Based on the presented BD approach, a novel model to capture the hindering effect of narrow pores on the mass transport within nano-pores is presented in the second publication. The knowledge gathered in the first and second publications are the basis for the proposed formation mechanism of nanoparticulate spray-dried clusters, presented in Chapter 5. The formation of nanoparticulate clusters is a complex process that involves a variety of packing mechanisms resulting in structured or unstructured arrays. In this work, it will be shown that by adding metallic salts during the cluster formation, the pore size of a nanoparticulate cluster can be adjusted. This effect on the pore size is caused by both mass transport, which is affected by hindered diffusion, and by the formation/crystallization of the added salt within the pores of the cluster. For this Chapter the more complex model, namely Fast Lubrication dynamics, is used in order to consider hydrodynamic interactions and electrostatic (DLVO) interactions between the NPs. A further method for the formation of nanoparticulate clusters using Langevin dynamics with an external electrostatic field is presented in the third publication.

1.1 Publication 1: Confinement effect on the mass transport properties and porous structure of porous media

There are different types of external fields that can affect the motion of nanoparticles, e.g. shear flow, electric, laser-optical and magnetic fields as well as confinement. In this publication titled *Numerical study of dispersive mass transport in homogeneous and heterogeneous porous media*,[21] the influence of confinement on the porous structure and mass transport properties of porous media is addressed. In addition, the performance of a particle-based stochastic approach, in this case Brownian dynamics, is compared to that of a continuum approach, namely the method of volume averaging. See graphical abstract in Fig. 1.1 and Chapter 3. One of the highlights and

Contribution as main author Writing, literature research and numerical calculations.

1.2 Publication 2: Hindering effect of pore size on the mass transport properties of porous media

In this publication titled *Mass transport in porous media at the micro- and nanoscale: A novel method to model hindered diffusion*,[22] the hindering effect of pore size on the diffusivity in the pore structure of porous media. This effect arises from the pairwise interaction between the diffusing molecules and the wall atoms of the porous medium. See graphical abstract in Fig. 1.2 and Chapter 4.

Contribution as main author Writing, literature research and numerical calculations.

---

[21] HECTOR RUSINQUE et al. *Comm. Compu. Inf. Sci.*, **1199**: 104–121, 2020.

[22] HECTOR RUSINQUE & GUNTHER BRENNER. *Microporous Mesoporous Mater.*, **280**: 157–165, 2019.

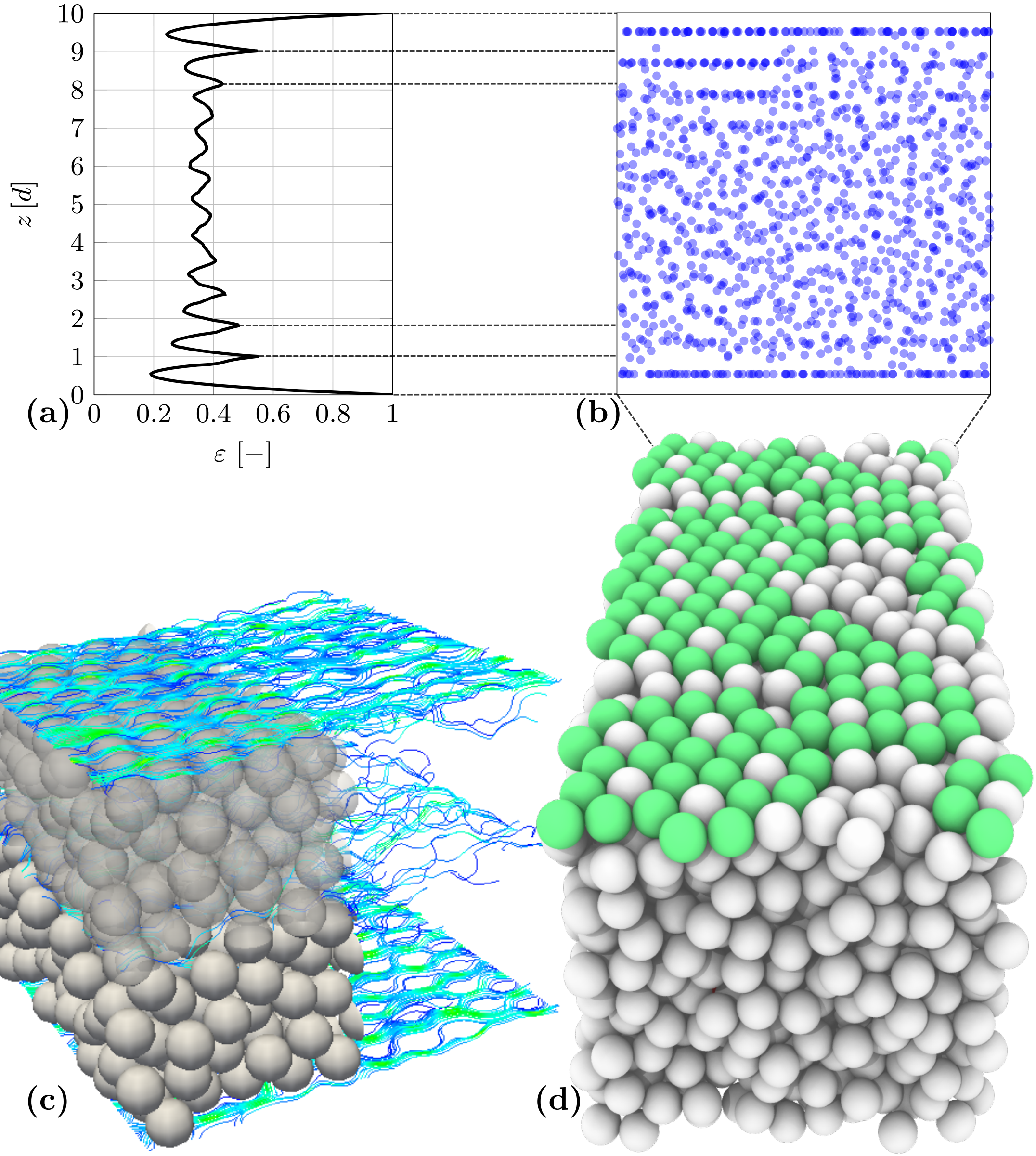

Figure 1.1: Graphical abstract of publication 1. (a) Porosity profile of a heterogeneous random sphere-packing along the vertical axis. (b) Projection of the particle-center coordinates on the plane perpendicular to the flow. (c) Streamlines through the sphere packing near the top and bottom confining walls as well as in the center of the packing. (d) Green-highlighted hexagonal configurations induced by the confining walls.

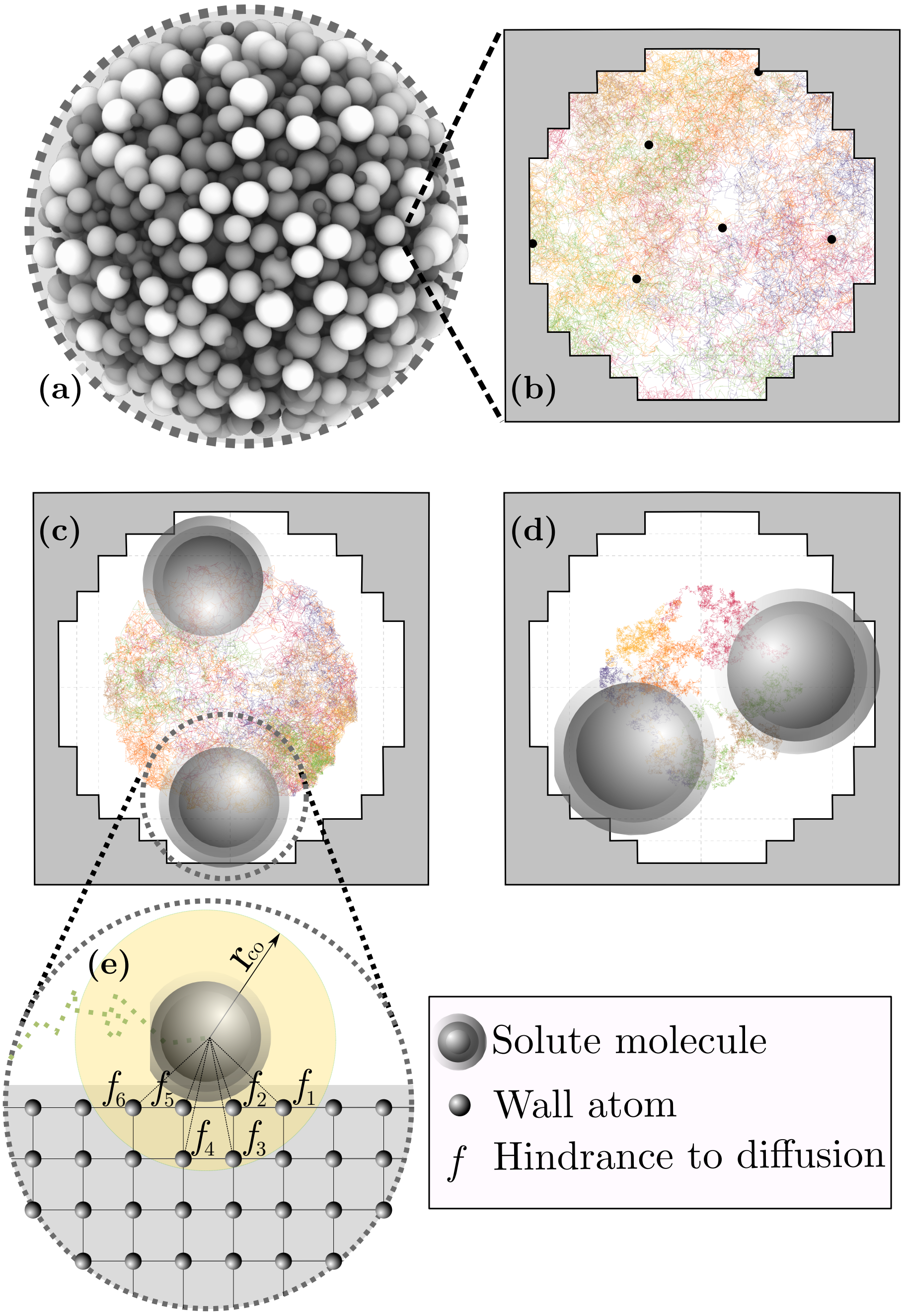
(a)
(b)
(c)
(d)
(e)
r_{co}
f_6
f_5
f_4
f_3
f_2
f_1
Solute molecule
Wall atom
f Hindrance to diffusion

Figure 1.2: Graphical abstract of publication 2. (a) Nanoparticulate cluster. (b),(c),(d) Molecules with different sizes diffusing in individual pores and random walks of these molecules. (e) Schematic representation of the pairwise interactions between a diffusing molecule and the wall atoms hindering diffusion.

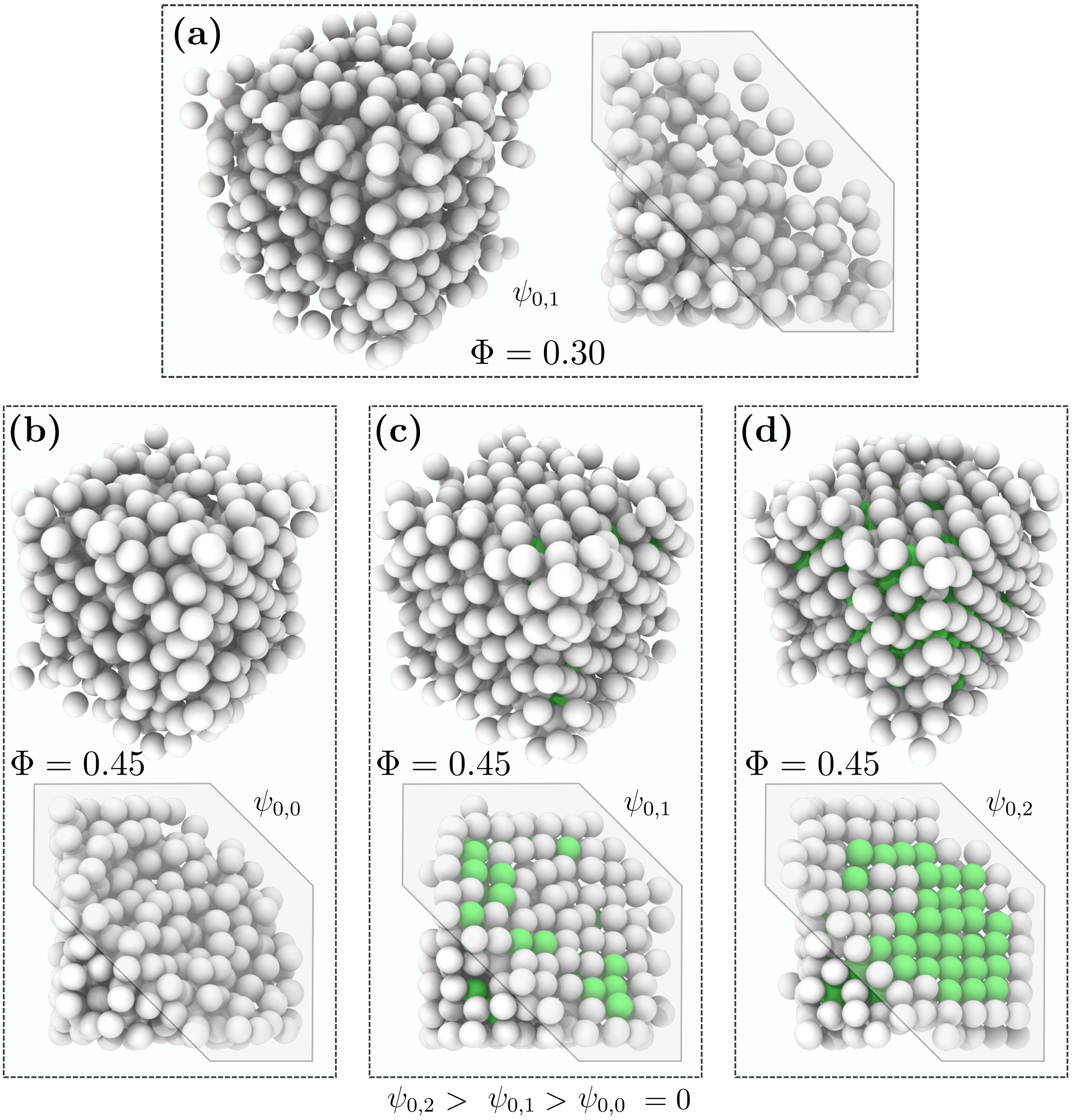
(a)
$\psi_{0,1}$
$\Phi = 0.30$
(b)
$\Phi = 0.45$
$\psi_{0,0}$
(c)
$\Phi = 0.45$
$\psi_{0,1}$
(d)
$\Phi = 0.45$
$\psi_{0,2}$
$\psi_{0,2} > \psi_{0,1} > \psi_{0,0} = 0$

Figure 1.3: Graphical abstract of publication 3. Bulk structure of nanoparticulate clusters at two different solid volume fractions, $\Phi = 0.30$ and $\Phi = 0.45$ and three different electric surface potentials $\psi_{0,2} = 115\,\mathrm{mV}$, $\psi_{0,1} = 50\,\mathrm{mV}$ and $\psi_{0,0} = 0\,\mathrm{mV}$.

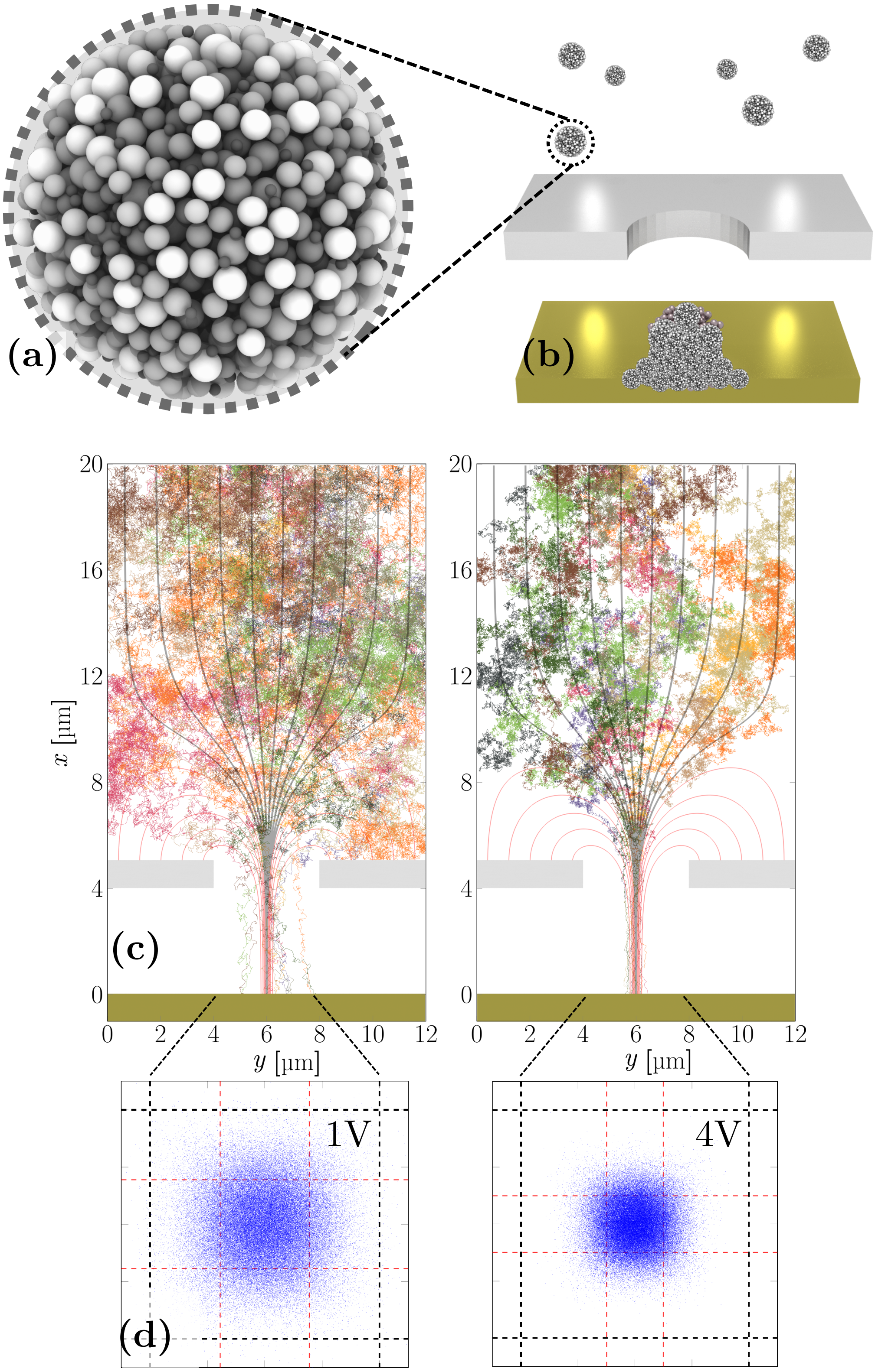

Figure 1.4: Graphical abstract of publication 4. (a) Nanoparticulate cluster (b) Schematic representation of the charged particles, the deposit and the electrodes of the deposition chamber. (c) Random walks of the charged particles. (d) Deposit pattern on the lower electrode (substrate).

1.3 Publication 3: Effect of electric forces on the formation of nanoparticulate, nanoporous clusters via spray-drying

In this Chapter titled the mechanism of formation of nanoparticulate clusters via spray-drying is presented and discussed. Further, confinement effects and pore-size hindering effects are also discussed. Here, the focus of the numerical calculations is on the effect of the pairwise electric interactions on the bulk structure of the clusters, which dominates the global structure of the clusters produced in the experiments. See graphical abstract in Fig. 1.3.

Contribution as main author Main writer, literature research, numerical calculations and interpretation of the experiments. The experiments were conducted mainly by Aurina Martinez-Arias at the Institute of Particle Technology at the TU Clausthal. Further co-authors are Juliana Rivas-Botero who conducted the particle size characterization using DLS and professor Alfred Weber from the Institute of Particle Technology, as well as professor Gunther Brenner from the Institute of Applied Mechanics, who as supervisors supported me by giving advice and observations.

1.4 Publication 4: Effect of an external electric field on the formation of nanoparticulate, nanoporous clusters via electro deposition

In this publication titled *Numerical study of the controlled electrodeposition of charged nanoparticles in an electric field*,[23] the effect of an external electric field on the formation of nanoparticulate clusters is studied. See graphical abstract in Fig. 1.4 and Chapter 6.

Contribution as main author Writing, literature research and numerical calculations.

As mentioned above, the papers published in the context of this work are presented in the following chapters, with a final chapter devoted to a final discussion.

---

[23] HECTOR RUSINQUE et al. *J. Aerosol Sci.*, **129**: 28–39, 2018.

2 Theory and Methods

2.1 Fundamentals of diffusion

2.1.1 Transport diffusion and self-diffusion

In principle, a distinction can be made between two diffusion phenomena: Transport diffusion and self-diffusion. Transport diffusion results phenomenologically from a concentration gradient of particles in a system, while self-diffusion results from the permanent change of microdynamic interactions of particles uniformly distributed in a system: thermal or Brownian motion.

Quantitatively, the process of self-diffusion is observable either by measuring the local change of a small amount of labeled particles in the total aggregate of all particles or by observing the local change of all individual particles in a defined time interval and subsequently calculating the mean square of displacement of these particles. In the process of self-diffusion, no macroscopic concentration gradient is needed. The 1st Fick's law provides the fundamental definition of diffusion

$$J_{A,i} = -D_\infty \frac{\partial C_A}{\partial x_i}\,, \tag{2.1}$$

where $J_{A,i}$ represents the diffusion flux of component A in the direction i, D_∞ the diffusion coefficient and the last term of this equation symbolizes the concentration gradient of the component A with respect to the coordinate x_i. Although the concentration gradient is responsible for the diffusion taking place in a system, the thermal (Brownian) force acting on a given diffusing particle (e.g. a solute molecule of A) from a thermodynamic point of view is the gradient of the chemical potential μ_i with respect to a spatial coordinate x_i;[13] for low concentrations of A (i.e. activity coefficient equals 1) it applies

$$F_i^{\mathrm{B}} = -\frac{\partial \mu}{\partial x_i} \approx -\frac{\partial}{\partial x_i}(k_{\mathrm{B}} T \ln C_A)\,, \tag{2.2}$$

k_B and T are the Boltzmann constant and the absolute temperature, respectively.

Alternatively to this thermodynamic and deterministic approach, a stochastic model of the thermal force can be used as follows

---

[13] A. EINSTEIN. *Ann. d. Phys.*, **322**: 549–560, 1905.

$$\left\langle F_i^{\mathrm{B}} \right\rangle = 0\,, \tag{2.3}$$

$$\left\langle F_j^{\mathrm{B}}(0) F_i^{\mathrm{B}}(t) \right\rangle = 2k_{\mathrm{B}}TR_{ij}\delta(t)\,. \tag{2.4}$$

The angle brackets indicate an ensemble average and $\delta(t)$ the Dirac delta function. R_{ij} stands for the hydrodynamic resistance tensor.

In case of free (unbounded) diffusion in an isotropic medium, taken into account the Einstein's relationship for the Diffusion coefficient,

$$D_\infty = \frac{k_{\mathrm{B}}T}{R}\,, \tag{2.5}$$

where the scalar/isotropic version of R is known as the (hydrodynamic) drag coefficient. For low Reynolds numbers, this coefficient is given by the Stoke's law $R = 6\pi\eta r_s$, where η stands for the viscosity of the unbounded solvent and r_s for the hydrodynamic radius of the diffusing particle or solute molecule. For this case, one can represent the stochastic Brownian Force as follows

$$F_i^{\mathrm{B}} = \sqrt{2D_\infty}\, W_i(t)\,, \tag{2.6}$$

which includes Gaussian white noise $W_i(t)$. Numerically, this is realized by generating for each Cartesian coordinate a normally distributed random number with zero mean $\mu = 0$ and variance $s^2 = 1$.[24,25]

As in other methods based on Newtonian N-body dynamics, such as Langevin and Brownian dynamics, the external forces acting on the particles can be distinguished into conservative forces F^{P} and the interactions with the solvent. The latter are described by the fluctuation-dissipation theorem, namely the fluctuating Brownian force F^{B} and its counterpart, the dissipative hydrodynamic force F^{H}, the force exerted on the particle by the fluid. This results in the following equation of motion for the NPs

$$m\frac{dU_i}{dt} = F_i^{\mathrm{H}} + F_i^{\mathrm{B}} + F_i^{\mathrm{P}}\,, \tag{2.7}$$

where U_i is the particle translational/rotational velocity vector and F^{P} is a conservative force arising from interparticle or external potentials.

When the particle Reynolds number is small, the hydrodynamic force exerted on the particles in a suspension in the absence of bulk shear flow is, i.e. fluid velocity $v_i = 0$

---

[24] H G Schuster & Wolfam Just. *Deterministic Chaos*. Wiley, 1994.

[25] Giorgio Volpe & Giovanni Volpe. *Am. J. Phys.*, **81**: 224–230, 2013.

$$F_i^H = -R_{ij}U_j \,, \tag{2.8}$$

where the hydrodynamic interactions are directly proportional to the particle translational/rotational velocities U.

In absence of neighbor particles (i.e. in absence of momentum transfer between neighbor particles via the solvent/medium), the resistance tensor of the medium can be simplified to reciprocal value of the drag coefficient, so that we obtain the following equation

$$F_i^H = -6\pi\eta r_s |U_i - v_i| \,, \tag{2.9}$$

where v_i is the fluid velocity at the center of the particle position.

Depending on the constraints and/or simplifications made to the Eq 2.7, the numerical approach considered receives different names. If the hydrodynamic forces are simplified by not considering the hydrodynamic exchange with neighboring particles, then this approach is called Langevin dynamics (LD), see Chapter 6. If to this simplification/constraint the inertial term (on the left hand of the equation) can be neglected, then it is given the name of Brownian dynamics (BD), see Chapters 3 & 4. This is very often the case for Brownian particles moving on a relatively long time scale, e.g. colloids in time scales of practical experiments, i.e. $t > 1\,\mu\mathrm{s}$, see Chapter 6.

In the case where hydrodynamic interactions with neighboring particles are considered, Stoksean dynamics (SD) is used. For this case, simplified/accelerated approaches have been developed, such as accelerated Stoksean dynamics (ASD) or Fast Lubrication dynamics (FLD), see Chapter 5.

In this work, various external fields like the velocity field v_i or electric field F^P are calculated to be given as input for the particle transport simulations: i.e. the Brownian or Langevin dynamics solvers, which describe the effective mass transport of a particle ensemble on a pore scale. These fields are determined using different methods, e.g. by numerically solving the Navier-Stokes equations or the Boltzmann equation for the flow and by solving the Poisson equation for the electric field. Since the theory behind the methods for determining the external fields is not described in detail in the studies published in the framework of this dissertation, the theoretical support for these topics is presented.

2.2 External fields: Velocity field

2.2.1 Liouville's equation

There is a system consisting of N particles. Each of these particles has m degrees of freedom, i.e. each has m location and momentum coordinates. Each particle (the k-th particle) can be defined by general position and momentum coordinates $x_i^{(k)} = \left(x_1^{(k)}, x_2^{(k)}, ..., x_m^{(k)}\right)$ or $p_i^{(k)} = \left(p_1^{(k)}, p_2^{(k)}, ..., p_m^{(k)}\right)$ with $k = 1, 2, ..., N$. The N particle system can be understood as a point with $2n = 2mN$ coordinates of this hyperspace (higher dimensional space), called phase space, at any time.[26]

The N-particle distribution density $f^{(N)}$ in phase space can be used to characterize an ensemble, i.e. the totality of quantum states of the physical N particle system. The N particle distribution density determines the probability $f^{(N)}(x_i, p_i)\mathrm{d}^n x \cdot \mathrm{d}^n p$ that the system is located in the infinitesimal volume element of the phase space $\mathrm{d}^n x \cdot \mathrm{d}^n p$.[26]

According to Liouville's theorem any volume element of this phase space

$$\mathrm{d}\mu = \mathrm{d}^n x \cdot \mathrm{d}^n p = \mathrm{d}x_1 \mathrm{d}x_2 ... \mathrm{d}x_n \cdot \mathrm{d}p_1 \mathrm{d}p_2 ... \mathrm{d}p_n = \mathrm{d}x_i^{(1)} \mathrm{d}x_i^{(2)} ... \mathrm{d}x_i^{(N)} \cdot \mathrm{d}p_i^{(1)} \mathrm{d}p_i^{(2)} ... \mathrm{d}p_i^{(N)},$$

is conserved over time. Due to this incompressibility, the distribution density along a trajectory remains constant and, analogous to the continuity equation for incompressible flow $\frac{\mathrm{d}}{\mathrm{d}t}\rho(t, x_i(t)) = 0$, their total differential disappears, this can be represented with index notation by,[26,27]

$$\frac{\mathrm{d}}{\mathrm{d}t} f^{(N)}(t, x_i(t), p_i(t)) = \frac{\partial f^{(N)}}{\partial t} + \sum_{i=1}^{n} \left[\frac{\partial f^{(N)}}{\partial x_i} \cdot \frac{\mathrm{d}x_i}{\mathrm{d}t} + \frac{\partial f^{(N)}}{\partial p_i} \cdot \frac{\mathrm{d}p_i}{\mathrm{d}t} \right] = 0\,. \tag{2.10}$$

If the redundant sum characters in the index notation are omitted and the corresponding variables are replaced by $p_i = m u_i$, $\frac{\mathrm{d}x_i}{\mathrm{d}t} = u_i$ bzw. $\frac{\mathrm{d}p_i}{\mathrm{d}t} = F_i$, the Liouville equation is reduced to

$$\frac{\partial f^{(N)}}{\partial t} + u_i \cdot \frac{\partial f^{(N)}}{\partial x_i} + \frac{F_i}{m} \cdot \frac{\partial f^{(N)}}{\partial u_i} = 0\,. \tag{2.11}$$

2.2.2 Boltzmann equation

The system of equations of the Liouville equation consists of a gigantic number of variables in the order of Avogadro's constant. Consequently, a numerical solution of the Liouville equation is impractical at the current state of the art.[27] Various approaches can be used to simplify the Liouville equation, including the linear response function and the Boltzmann equation.[26] A simplification of the latter is applied in the context of this work.

---

[26] G. CHEN. *MIT-Pappalardo Seri. Mech. Eng.*, Oxford University Press, 2005.

[27] S. HARRIS. *Dover Books on Physics*, Dover Publications, 2012.

In Boltzmann's transport equation, the $2n$-dimensional phase space is reduced to six dimensions by introducing a one-particle distribution function by averaging the N-particle distribution function over the remaining $(N-1)$ particles in the system.[26]

$$f^{(1)} = \frac{N!}{(N-1)!} \int \cdots \int f^{(N)} \mathrm{d}x_2 ... \mathrm{d}x_n \cdot \mathrm{d}p_2 ... \mathrm{d}p_n \,. \tag{2.12}$$

After determining the averaged single particle distribution density, the Liouville equation can be averaged over the spatial and momentum coordinates of the remaining $(N-1)$ particles. After averaging, the Boltzmann equation is obtained with $f^{(1)} = f$ [4,5,28]

$$\frac{\partial f}{\partial t} + \frac{\partial f}{\partial x_i} \cdot \frac{\mathrm{d}x_i}{\mathrm{d}t} + \frac{\partial f}{\partial p_i} \cdot \frac{\mathrm{d}p_i}{\mathrm{d}t} = \left(\frac{\partial f}{\partial t}\right)_{\text{Stoss}} \,. \tag{2.13}$$

If one sets the equation as a function of location and velocity coordinates, the following equation results

$$\left(\frac{\partial}{\partial t} + u_i \cdot \frac{\partial}{\partial x_i} + \frac{F_i}{m} \cdot \frac{\partial}{\partial u_i}\right) f = \left(\frac{\partial f}{\partial t}\right)_{\text{Stoss}} \,. \tag{2.14}$$

Here the left side of the equation is the total differential of f with particle mass m, particle velocity u_i and external force F_i consisting of the accumulation, transport and field terms, respectively, while $\left(\frac{\partial f}{\partial t}\right)_{\text{Stoss}}$ is the scattering or collision integral which detects the collisions of the individual particles. A rigorous treatment of the collision integral consists in the use of the Boltzmann collision term (Stosszahlansatz).

The Stosszahlansatz is a multidimensional integral in which f is non-linearly related

$$\begin{aligned}\left(\frac{\partial f}{\partial t}\right)_{\text{Stoss}} &= -\int \cdots \int f(\vec{x},\vec{u},t) f(\vec{x},\vec{u}_A,t) W(\vec{u},\vec{u}_A \longrightarrow \vec{u}^*,\vec{u}_A^*) \mathrm{d}^3\vec{u}^* \mathrm{d}^3\vec{u}_A \mathrm{d}^3\vec{u}_A^* \\ &+ \int \cdots \int f(\vec{x},\vec{u}^*,t) f(\vec{x},\vec{u}_A^*,t) W(\vec{u}^*,\vec{u}_A^* \longrightarrow \vec{u},\vec{u}_A) \mathrm{d}^3\vec{u}^* \mathrm{d}^3\vec{u}_A \mathrm{d}^3\vec{u}_A^* \,. \end{aligned} \tag{2.15}$$

Here, the first term on the right-hand side represents the transition rate of the particles that change from quantum states $\vec{u}, \vec{u}_A$ to $\vec{u}^*, \vec{u}_A^*$ when they collide. The second term stands for the transition rate of the particles into the quantum states $\vec{u}, \vec{u}_A$.

The transition rate W can be determined using the Fermis Golden Rule from quantum mechanical perturbation theory. It is assumed that at any given time the number of particles with velocities before the impact ($\vec{u}$, $\vec{u}_A$ and afterwards $\vec{u}^*$, $\vec{u}_A^*$) is uncorrelated. This is known as the assumption of molecular chaos. In addition, it is assumed that the mean free path length of the particles is large, i.e. that the volume fraction of the gas particles is so small that only two collisions can be considered. One of the properties of the transition

---

[4] A. A. MOHAMAD. , Springer–Verlag London, 2011.

[5] DIETER HÄNEL. , Springer–Verlag Berlin Heidelberg, 2004.

[28] M.C. SUKOP & D.T. THORNE. , Springer Berlin Heidelberg, 2010.

rate includes the interchangeability of the particles, from which the above equation can be reduced to[5,26]

$$\left(\frac{\partial f}{\partial t}\right)_{\text{Stoss}} = \int \cdots \int W(\vec{u}, \vec{u}_A \longrightarrow \vec{u}^*, \vec{u}_A^*)\{f(\vec{x}, \vec{u}, t) f(\vec{x}, \vec{u}_A, t) - f(\vec{x}, \vec{u}^*, t) f(\vec{x}, \vec{u}_A^*, t)\} \mathrm{d}^3\vec{u}^* \mathrm{d}^3\vec{u}_A \mathrm{d}^3\vec{u}_A^* \,. \tag{2.16}$$

However, the solution of the Stosszahlansatz is too complex, which is why the relaxation time approximation is usually used instead

$$\left(\frac{\partial f}{\partial t}\right)_{\text{Stoss}} \approx -\frac{f - f^{\text{eq}}}{\tau} \,, \tag{2.17}$$

where τ stands for the relaxation time and f^{eq} for the equilibrium distribution, which in the case of molecules can be described by the Maxwell distribution f^{Mw}. It gives the probability density that the energy carriers (the molecules) at an absolute temperature T have an energy level E.[5,26]

$$f^{\text{Mw}}(E) = A e^{\left(\frac{-E}{k_B T}\right)} \,, \tag{2.18}$$

where k_B stands for the Boltzmann constant.

Monoatomic gases can only store energy in the form of kinetic energy and have 3 degrees of freedom (translation velocities) u_x, u_y and u_z. From this follows

$$f^{\text{Mw}}(u_i) = A \exp\left(-\frac{1/2 m(u_x^2 + u_y^2 + u_z^2)}{k_B T}\right) . \tag{2.19}$$

Here m is the mass of a molecule.

To calculate the factor A the distribution density f^{Mw} is normalized.

$$\int_0^\infty \int_0^\infty \int_0^\infty f^{\text{Mw}}(u_i) \mathrm{d}u_x \mathrm{d}u_y \mathrm{d}u_z = 1 \,. \tag{2.20}$$

If spherical coordinates are used, the following equation is obtained

$$\int_0^\infty \int_0^{2\pi} \int_0^\pi f^{\text{Mw}}(u_i) u_i^2 \sin(\theta) \mathrm{d}\varphi \mathrm{d}\theta \mathrm{d}u_i = 1 \,, \tag{2.21}$$

$$\int_0^\infty 4\pi u_i^2 f^{\text{Mw}}(u_i) \mathrm{d}u_i = 1 \,, \tag{2.22}$$

$$\left(\frac{2\pi k_B T}{m}\right)^{3/2} A = 1 \xrightarrow{\text{to } A} A = \left(\frac{m}{2\pi k_B T}\right)^{3/2} . \tag{2.23}$$

If the mean velocity of the particles v_i is not zero, the Maxwell distribution shifts by this mean value. Multiplying the distribution given by the equation 2.18 with the particle density $n = N/V$ (the ratio of particle number to volume) and replacing the specific gas constant $R_s = k_B/m$ (from $R = N_A k_B$, $M = N_A m$ or $R_s = R/M$, where R, N_A

and M stand for the universal gas constant, the Avogadro number and the molar mass respectively), the equilibrium distribution[5,26] is obtained

$$f^{\text{eq}}(n, u_i) = \frac{n}{(2\pi R_s T)^{3/2}} \exp\left(-\frac{(u_i - v_i)^2}{2R_s T}\right). \tag{2.24}$$

In the literature one can find different variants of the relaxation time approximation, where the relaxation of the system into equilibrium takes place in one or more steps (relaxation times). Different relaxation parameters are used for each moment of the distribution function. In addition, the equilibrium distribution depends on the type of energy carriers, e.g. phonons (elementary excitations of the elastic field) and electrons can be described by the Bose-Einstein or Fermi-Dirac distributions.[26]

The Boltzmann equation[5]

- applies to general non-equilibrium processes,
- describes gas dynamic flow processes,
- applies from the continuum range with Knudsen numbers $\mathrm{Kn} \ll 1$ to the free molecular flow with $\mathrm{Kn} \gg 1$.
- Their moments lead to the conservation equations for mass, momentum and energy of a frictionless and heat conduction-free flow (Euler equations).
- For small deviations from the thermodynamic equilibrium the Navier-Stokes equations can be obtained with the help of the Chapman-Enskog development.[5]
- Using the Boltzmann H-theorem, the Maxwell distribution can be derived and the entropy defined.[5]

2.2.3 Lattice Boltzmann Method

The Lattice Boltzmann method (LBM) can be seen both as a further development of the Lattice Gas methods and as a direct discretization of the Boltzmann equation. In the following, the Boltzmann equation (2.14) is introduced with the relaxation time approximation of the collision integral (2.17) while neglecting the field term (no external forces). First, the phase space of the equation is discretized by introducing discrete velocity vectors and then the equilibrium distribution 2.24 is discretized by Taylor series expansion of the Maxwell distribution.[4,28,29]
Discretization of the velocity space u_i via the index α

$$\frac{\partial f_\alpha}{\partial t} + u_{i,\alpha} \cdot \frac{\partial f_\alpha}{\partial x_i} = -\frac{f_\alpha - f_\alpha^{\text{eq}}}{\tau}, \qquad \alpha = 0, 1, ..., N-1. \tag{2.25}$$

---

[29] D. Arumuga Perumal & Anoop K. Dass. *Alex. Eng. J.*, **54**: 955 –971, 2015.

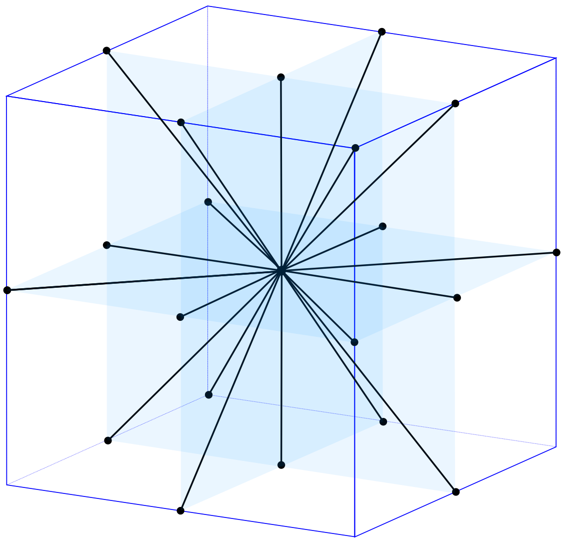

Figure 2.1: Velocity directions of a fluid cell in the D3Q19 model

Here $f(x_i, u_i, t)$ changes to $f(x_i, u_{i,\alpha}, t) = f_\alpha(x_i, t)$. While nine discrete velocities (D2Q9 model) are usually used for LBM calculations of two-dimensional flows, both 15 and 19 discrete velocities (D3Q15/D3Q19 model) are often used for three-dimensional flows. In this work, the D3Q19 model is used (see Fig. 2.1).

Discretization of the equilibrium distribution 2.24 by Taylor series expansion

$$f_\alpha^{\mathrm{eq}}(n, u_i) = w_i n \left\{ 1 + \frac{u_{i,\alpha} v_i}{a_s^2} + \frac{(u_{i,\alpha} v_i)^2}{2a_s^4} + \frac{v_i v_i}{2a_s^2} \right\}, \tag{2.26}$$

with $a_s = \sqrt{2R_sT}$. The normalization factors of the Maxwell distribution are combined into a direction-dependent weighting factor w_i. For the correct representation of the hydrodynamic behavior, the second-order term of the Taylor series must be taken into account. Nevertheless, the discrete Maxwell distribution should only be used for relatively low flow velocities (Low Mach Number Approximation).[29]

To solve the system of partial differential equations, the LBM can be interpreted as two successive steps: The collision step

$$f_\alpha(x_i, t + \Delta t) = f_\alpha(x_i, t) + \frac{f_\alpha^{eq} - f_\alpha}{\tau}, \tag{2.27}$$

and the propagation step

$$f_\alpha(x_i + u_{i,\alpha}\Delta t, t + \Delta t) = f_\alpha(x_i, t + \Delta t). \tag{2.28}$$

Initial and boundary conditions

Due to their intrinsic kinetic nature, the boundary conditions of the Lattice-Boltzmann method cannot be directly compared with those of the macroscopic approaches.[4] For this purpose, suitable microscopic observations must be applied which, on a macroscopic level, reproduce the corresponding behaviour of Dirichlet or Neumann boundary conditions.

Since the distribution functions in the complex porous geometry are a priori unknown, in the present work each fluid cell of the three-dimensional lattice is initialized in the state of equilibrium at zero velocity. Periodic boundary conditions are set at inlet and outlet edges and the flow is driven by a force field (no pressure gradient) acting only in the direction of flow. The density, viscosity and magnitude of the external force are specified taking into account the physical and numerical limitations.[4,5]

The realisation of the no-slip condition can be achieved in the simplest case with the help of the so-called bounce-back rule. Here, the distribution function penetrating a cell defined as a solid is reflected in the next time step with opposite direction and thus returned to the origin node of the fluid cell. Extrapolation and interpolation-based variants of the bounce-back rule are available in the literature,[4,5] which provide a better representation of the collisions with the walls. In contrast to the simple bounce-back rule, these do not guarantee complete mass conservation. For the simulations in this study only the simple bounce-back rule was used.[5]

2.2.4 Calculation of macroscopic quantities

The moments of the distribution function lead to macroscopic quantities as follows

$$\rho(x_i,t) = \iiint\limits_{-\infty}^{+\infty} (u_i)^0 \, f(x_i,u_i,t)\mathrm{d}u_i \,, \qquad \text{density as zero moment,} \tag{2.29}$$

$$\rho(x_i,t)v_i(x_i,t) = \iiint\limits_{-\infty}^{+\infty} (u_i)^1 \, f(x_i,u_i,t)\mathrm{d}u_i \,, \qquad \text{momentum as first moment.} \tag{2.30}$$

In the case of discrete distribution functions, the macroscopic quantities are given by

$$\rho(x_i,t) = \sum_{\alpha} (u_i)^0 \, f(x_i,u_i,t) \,, \tag{2.31}$$

$$\rho(x_i,t)v_i(x_i,t) = \sum_{\alpha} (u_i)^1 \, f(x_i,u_i,t) \,. \tag{2.32}$$

2.2.5 NavierStokes equations

The Navier-Stokes equations (NSE) are the base for second method used in this work to compute the bulk flow, specifically in Chapter 3.[21] In this approach, fluids are treated as a continuum, i.e. when the Knudsen number is significantly less than one ($\mathrm{Kn} \ll 1$), which is fulfilled in practice when the mean free path length is significantly shorter than the characteristic length of the system.

---

[21] HECTOR RUSINQUE et al. *Comm. Compu. Inf. Sci.*, **1199**: 104–121, 2020.

The flow of Newtonian fluids and gases at a continuum level is described using the NSE with specified initial and boundary conditions

$$\frac{\partial \rho}{\partial t} + \frac{\partial(\rho u_i)}{\partial x_i} = 0 \,, \qquad \text{continuity equation,} \tag{2.33}$$

$$\frac{\partial \rho u_i}{\partial t} + \frac{\partial \rho u_i u_j}{\partial x_j} = \rho k_i + \frac{\partial \sigma_{ij}}{\partial u_j} \,, \qquad \text{momentum equation.} \tag{2.34}$$

The splitting of the stress tensor consists of normal stresses caused by pressure forces and shear stresses induced by viscous, frictional forces, as follows

$$\sigma_{ij} = -p\delta_{ij} + \tau_{ij} \,, \tag{2.35}$$

The momentum equation in differential form for the components x_1, x_2 and x_3 is

$$\frac{\partial \rho u_i}{\partial t} + \frac{\partial \rho u_i u_j}{\partial x_j} = \rho k_i - \frac{\partial p}{\partial x_i} + \mu \frac{\partial^2 u_i}{\partial x_j^2} \,. \tag{2.36}$$

It is considered here that a pressure p acts on a fluid of density ρ and that fluid layers located next to each other exert a dissipative force on each other during relative movement, the amount of which is proportional to the viscosity μ. The contributions of other external inertial forces are summarized under k_i. Thus, an incompressible flow is completely described by a partial differential equation system with two equations for the two variables velocity u_i and pressure p as a function of position and time.
The flow is incompressible if the density ρ remains constant along a trajectory. Gravity g_i can be assumed as the only external inertial force. From this follows

$$\frac{\mathrm{d}}{\mathrm{d}t}\rho(t, x_i(t)) = 0 \Rightarrow \frac{\partial u_i}{\partial x_i} = 0 \,, \qquad \text{continuity equation,} \tag{2.37}$$

$$\rho \left(\frac{\partial u_i}{\partial t} + u_i \frac{\partial u_i}{\partial x_j} \right) = \rho g_i - \frac{\partial p}{\partial x_i} + \mu \frac{\partial^2 u_i}{\partial x_j^2} \,, \qquad \text{momentum equation.} \tag{2.38}$$

2.3 External fields: Electric field

Microscopic Maxwell's equations

The microscopic Maxwell's equations link the electric field strength $\mathbf{E}$ and the magnetic flux density $\mathbf{B}$ with the charge density ρ (charge per volume) and the electric current density $\mathbf{J}$ (current per area, across which the charges of the electric current flow).

Gauss's law

$$\nabla \cdot \mathbf{E} = \frac{\rho}{\epsilon_0}\,. \tag{2.39}$$

Physical implications: Electric field lines diverge from each other at positive electric charges and converge to negative charges, i.e. negative charges are sources of the electric field, while positive charges act as sinks of the electric field.

Gauss's law for magnetism

$$\nabla \cdot \mathbf{B} = 0\,. \tag{2.40}$$

Physical impications: Magnetic field lines do not diverge, i.e. they have no sources; no magnetic monopoles exist.

Faraday's law of induction and extended Ampère's law

$$\nabla \times \mathbf{E} = -\frac{\partial \mathbf{B}}{\partial t}\,, \tag{2.41}$$

$$\nabla \times \mathbf{B} = \mu_0 \left(\mathbf{J} + \epsilon_0 \frac{\partial \mathbf{E}}{\partial t} \right)\,. \tag{2.42}$$

Physical implications: Electric and magnetic fields are generated by moving electric charges; changes in the magnetic field induce a vortex of the electric field (see Eqn. 2.41); changes in the electric field generate vortex of magnetic field (see Eqn. 2.42); the electric and magnetic fields induce forces on electric charges.

Electrostatic force

The electromagnetic force, known after the Dutch mathematician and physicist Hendrik Antoon Lorentz as Lorentz force, is the force that a particle of charge q experiences in a magnetic or electric field. A magnetic field exerts force on moving charges , while an electric field acts equally on moving and stationary charges.

$$\mathbf{F} = q\mathbf{E} + q\mathbf{v} \times \mathbf{B}\,. \tag{2.43}$$

Here, the charged particle moves with a velocity $\mathbf{v}$; the electromagnetic force can be seen as the resulting force of two forces: a magnetic force $q\mathbf{v} \times \mathbf{B}$, and an electric force $q\mathbf{E}$. The latter is also known as Coulomb force when the magnetic contribution to the Lorentz force is neglected. For the magnetic force to be negligible, the charges must be stationary in relation to each other; for slow movements the influence of the magnetic force is minimal and the Coulomb's law can still be regarded as approximately correct, but if the charges move faster in relation to each other, then the full electrodynamic laws (including the magnetic force) must be taken into account. This consideration is known as electrostatic approximation. Further, the charges on the particle must have a spherically symmetric distribution, i.e. they should be isotropic.

$$\mathbf{F} = q\mathbf{E} + q\mathbf{v} \times \mathbf{B} \tag{2.44}$$

The electric field can be derived from the electric potential φ as follows

$$\mathbf{E} = -\nabla\varphi \tag{2.45}$$

From Gauss's law 2.39, the Poisson's equation in the electrostatic approximation is obtained as follows

$$\nabla \cdot \mathbf{E} = \nabla \cdot (-\nabla\varphi) = -\nabla^2\varphi = \frac{\rho}{\epsilon}, \tag{2.46}$$

$$\nabla^2\varphi = -\frac{\rho}{\epsilon}. \tag{2.47}$$

Solving the Poisson equation boils down to finding the electric potential φ for a given charge distribution ρ.

2.3.1 Hard-sphere-like colloids

Additional information is provided in order to bring more clarity and theoretical background to the formation of clusters from colloidal dispersions. Here, we consider the colloidal particles as hard-sphere-like colloids with parameters similar to those used in earlier works .[15,30–32] The long-time self-diffusivity of colloidal dispersions of hard-sphere-like particles at different volume fractions is computed and graphically represented in Fig. 2.2.

Here, we used two established values for Φ_{max}, namely the glass transition and the melting volume fraction at $\Phi_g = 0.58$ and $\Phi_m \approx 0.63$, respectively .[33–35] Further, the solid line in Fig. 2.2 represents the analytical prediction of Brady [33] for the long-time self-diffusivity when the volume fraction approaches the random-close-packing limit, $\Phi \to \Phi_m \lessapprox \Phi_{\mathrm{rcp}}$. Strictly speaking, the configuration at the melting volume fraction Φ_m corresponds to a loose rcp-like structure. Although there is no general consensus about the exact value of $\Phi_{\mathrm{rcp}} \approx 0.65$ for monodisperse hard-sphere packings, one of the conditions imposed

---

[15] Michael P. Howard et al. *J. Chem. Phys.*, **149**: 094901, 2018.

[30] Pieter J. In't Veld et al. *Phys. Rev. E*, **79**: 10–13, 2009.

[31] P. R. Schunk et al. *J. Rheol.*, **56**: 353–384, 2012.

[32] Dan S Bolintineanu et al. *Comput. Part. Mech.*, **1**: 321–356, 2014.

[33] John F. Brady. *J. Fluid Mech.*, **272**: 109–133, 1994.

[34] Clara Weis et al. *Sci. Rep.*, **6**: 1–15, 2016.

[35] Heather M. Shewan & Jason R. Stokes. *J Non-Newton Fluid*, **222**: 72–81, 2014.

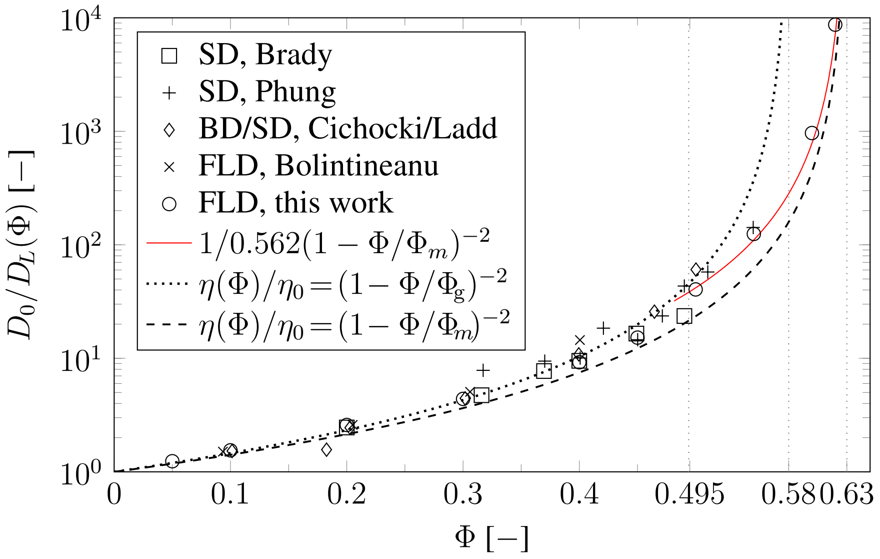

Figure 2.2: Relative diffusivity vs. solid fraction. Hard-sphere case, the most studied case in literature.

to the rcp structure is mechanical stability .[36,37] This fundamental condition is not fulfilled by a colloidal rcp-like structure or crystal, as they still have vibrational degrees of freedom .[37–40]

From Fig. 2.2, as the colloidal dispersion approaches the freezing volume fraction $\Phi_f \approx 0.495$, the long-time self-diffusivity moves from the upper viscosity curve that diverges to the glass transition volume fraction Φ_g, down to the lower curve that diverges at the melting volume fraction Φ_m, passing through the analytical prediction of Brady. Notice that at the glass transition volume fraction, the dispersion switches from a solid dispersed in a continuous liquid phase to a liquid dispersed in a continuous solid phase, meaning that the mechanical behavior of the system switches from being dominated by viscous regions to elastic regions .[34] Thus, the homogeneous dispersion present below the freezing volume fraction diverges to Φ_g, whereas the heterogeneous dispersion of NPs and larger rcp-like clusters that are formed above the freezing volume fraction Φ_f, diverges to Φ_m.

---

[36] VASILI BARANAU & ULRICH TALLAREK. *Soft Matter*, **10**: 3826–3841, 2014.
[37] VASILI BARANAU et al. *Soft Matter*, **12**: 3991–4006, 2016.
[38] JÖRG BAUMGARTL et al. *Soft Matter*, **4**: 2199, 2008.
[39] ZHENGDONG CHENG et al. *Phys. Rev. Lett.*, **85**: 1460–1463, 2000.
[40] R. S. PENCIU et al. *Europhys. Lett.*, **58**: 699–704, 2002.

3 Confinement effects on mass transport and packing arrangement

This chapter was published in the form of a full paper in the proceedings of the conference Simulation Science 2019

Hector Rusinque, Eugenia Barthelmie, & Gunther Brenner (2020).
Numerical study of dispersive mass transport in homogeneous and heterogeneous porous media
Communications in Computer and Information Science
Simulation Science 2019, 1199, 104–121.
DOI: 10.1007/978-3-030-45718-1_7 .

3.1 Zusammenfassung

Vielfältige Anwendungen wie z.B. die Ausbreitung eines Schadstoffs in einem Grundwasserleiter, der gezielte Wirkstoff-Transport und Lieferung eines Medikaments in ein gewünschtes Gewebe sowie die Effizienz einer Chromatographiesäule können anhand mathematischer hochskalierter Modelle abgebildet werden, bei denen die Vorkenntnis von effektiven materialabhängigen Modellparametern vorausgesetzt ist. Zur Erfüllung dieser Voraussetzung ist eine umfassende Charakterisierung der zu untersucheden porösen Medien unerlässlich. Dies ist in der Regel aufwändig, da die Stofftransporteigenschaften stark mit der komplexen Porenstruktur des porösen Mediums korrelieren. Als Modellparameter wurden mehrere Deskriptoren vorgeschlagen, wie z.B. die hydraulische Tortuosität in der Kozeny-Carman-Gleichung und die diffusive Tortuosität, deren reziproker Wert in der deutschen Literatur häufig als Laberynth-Faktor bezeichnet wird. Zur Ermittlung dieser Parameter können hochaufgelöste Modelle in Einsatz kommen. Allerdings, wenn das poröse Medium eine heterogene Porenstruktur aufweist, dann scheitern hochaufgelöste Kontinuumsmodelle und empirische Korrelationen daran, den anisotropen Charakter solcher Medien zu erfassen. Zur Beschreibung von Transportphänomenen in porösen Medien auf der Porenskala stehen mehrere Modelle zur Verfügung wie zum Beispiel die Methode der Volumenmittelung (MVA),[41–43] die Homogenisierung,[44] und die

---

[41] STEPHEN WHITAKER. *The Method of Volume Averaging*. **volume** 13 Theory and Applications of Transport in Porous Media Kluwer Academic Publishers, 1999. 219

[42] F.J. VALDES-PARADA & C.G. AGUILAR-MADERA. *Chem. Eng. Trans.*, **24**: 1453–1458, 2011.

[43] HELEN D. LUGO-MÉNDEZ et al. *Transport Porous Med.*, **107**: 683–716, 2015.

[44] ULRICH HORNUNG, **editor**. *Homogenization and Porous Media*. **volume** 6 Interdisciplinary Applied Mathematics New York: Springer, 1991. 1–279

thermodynamisch eingeschränkte Mittelwertbildungstheorie,[45] welche von einem Kontinuumsmedium ausgehen, sowie partikelbasierte Methoden wie Brownsche Dynamik (BD), Langevin Dynamik unter anderen.[22,46–48] In dieser Studie werden die MVA- und BD-Ansätze zur Modellierung des Stofftransportes im Hohlraum von homogenen bzw. heterogenen porösen Materialien eingesetzt. Dabei werden nach Lösung der in jedem Ansatz involvierten Differentialgleichungen effektive Transportparameter bzw. Deskriptoren der porösen Struktur aus den gewonnenen porenskaligen Informationen des Mediums bestimmt.

In diesem Kapitel werden zunächst die oben genannten Ansätze vorgestellt und verglichen. AnschlieSSend werden heterogene poröse Medien betrachtet, wobei der Einfluss von Wänden (d.h. räumlichen Einschränkungen) auf die Struktur von eingeschlossenen Zufallskugelpackungen untersucht wird und wie diese die Massentransporteigenschaften der porösen Kugelpackung beeinflussen. Darüber hinaus wird die hydraulische Tortuo sität berechnet und ihre Aussagekraft als Deskriptor für poröse Medien mit der der diffusiven Tortuosität verglichen.

Wie man im Ergebnissteil zeigen wird, ist in der strukturierten Geometrie des homogenen Mediums eine deutliche Korrelation der dispersiven Transporteigenschaften der Medien mit ihren Tortuositäts- und effektiven Porositätswerten zu erkennen, im Gegensatz zum heterogenen Medium, in dem keine direkte Korrelation zwischen den betrachteten Parametern besteht. Dies liegt daran, dass es sich bei den verwendeten Deskriptoren um Effektivwerte handelt, die nicht in der Lage sind, den dispersiven Effekt zu erfassen, der durch die ausgeprägte Heterogenität in der mikroskopischen Porenstruktur hervorgerufen wird. Anstelle von effektiven Parametern wird die Verwendung einer lokalen hydraulischen Tortuosität vorgeschlagen, deren Implementierung zukünftigen Arbeiten überlassen wird.

Darüber hinaus wurde im Vergleichsabschnitt der MVA- und BD-Ansätze im Fall homogener poröser Medien festgestellt, wie der MVA-Ansatz die Brownsche Dynamik sowohl hinsichtlich der Genauigkeit als auch der Rechenzeit übertrifft. Daraus wird geschlussfolgert, dass diese Methode bei der Beschreibung von homogenen Porenstrukturen vorteilhaft ist. Wie bereits erwähnt, ist ein solches Kontinuumsmodell jedoch nicht in der Lage, die Anisotropie einer heterogenen Porenstruktur (wie z.B. die einer räumlich eingeschränkten Zufallskugelpackungen) zu reproduzieren.

---

[45] William G. Gray & Cass T. Miller. *Adv. Water Res.*, **28**: 161–180, 2005.
[22] Hector Rusinque & Gunther Brenner. *Microporous Mesoporous Mater.*, **280**: 157–165, 2019.
[46] Tobias Heidig et al. *Chem. Ing. Tech.*, **86**: 554–560, 2014.
[47] Siarhei Khirevich et al. *J. Chromatogr. A*, **1217**: 4713–4722, 2010.
[48] Harun Koku et al. *J. Chromatogr. A*, **1237**: 55–63, 2012.

3.2 Abstract

A modular simulation approach is used to compute the flow of a fluid and the mass transport of tracers in the void space of computer-generated porous packings. Effective transport properties such as the diffusive tortuosity and the dispersion tensor are determined. First, we present and compare two different approaches to model mass transport in homogeneous porous media. Subsequently, heterogeneous porous media are considered, where we investigate the effect of walls on the structure of confined random sphere packings and how it affects the mass transport properties of a sphere packing. In addition, the hydraulic tortuosity is computed and its performance as a descriptor of porous media is compared with that of the diffusive tortuosity.

3.3 Introduction

A rigorous characterization of porous media is important for the determination of parameters needed in mathematical models that can describe e.g. the spreading of a contaminant in an aquifer, the successful delivery of a drug in a desired tissue or the efficiency of a separation process as in column chromatography. Such a characterization is usually complex, since mass transport properties correlate strongly with the intricate pore structure of the porous medium. Usually, upscaled models and correlations failed to capture the anisotropic nature of heterogeneous porous media,[49] several descriptors have been proposed such as the hydraulic tortuosity in the Kozeny-Carman equation.[49–53] There are several models capable of describing transport phenomena in porous media such as the method of volume averaging (MVA),[41–43] Brownian dynamics (BD),[22,46–48] homogenization,[44] and the thermodynamically constrained averaging theory.[45] In this study, we used the MVA and BD approaches in order to describe the motion of molecules diffusing in the void space of homogeneous and heterogeneous porous materials. After solving the differential equations involved in each approach, effective transport parameters and descriptors of the porous structure are determined from the obtained information of the system as will be explained in detail in the modeling section of this work.

Further, both methods are described and compared considering transport in homogeneous porous media. Finally, wall effects on mass transport are studied. For this purpose, confined sphere packings were computer-generated and their mass transport properties were obtained using the BD approach.

---

[49] Behzad Ghanbarian et al. *Soil Sci. Soc. Am. J.*, **77**: 1461, 2013.

[50] P.C. Carman. *Chem. Eng. Res. Des.*, **75**: S32 –S48, 1937.

[51] J. Bear. *Dynamics of Fluids In Porous Media*. v. 1 American Elsevier, 1972.

[52] Carl Fredrik Berg. *Transport Porous Med.*, **103**: 381–400, 2014.

[53] S. M.Rezaei Niya & A. P.S. Selvadurai. *Transport Porous Med.*, **121**: 741–752, 2018.

3.4 Modeling and numerical approach

We commence by describing the general system with domain $\Omega \subset \mathbb{R}^3$ or in some simulation cases $\Omega \subset \mathbb{R}^2$. It is considered a rigid porous medium (a solid phase Ω_s) completely filled with a fluid phase with domain Ω_f. The fluid flows through the porous medium carrying a solute (passive point-wise species), which in turn moves via diffusion. The solid phase is assumed impermeable to mass transport.

We combined two simulation steps in both computational approaches (MVA and BD). In the first step, the velocity field is computed. In the second step, we simulate the mass transport using the velocity field obtained in the first step, as input.

3.4.1 Computation of the velocity field

We obtained the velocity fields from the numerical solution of the Stokes equation[54,55] or the Boltzmann equation, using the Lattice Boltzman method (LBM).[29,56] As all the porous structures considered are periodic in at least two directions, we used periodic boundary conditions for the velocity field on the respective boundaries. The no-slip condition for viscous flow was applied on the walls and solid-fluid interface. A constant external force was used as driving force inducing the flow. For the LBM, we chose a force so that the Reynolds number is kept low enough, i.e., $\mathrm{Re} \ll 1$, to assure creeping flow. Advective inertial forces are not considered in the Stokes equations per default, resulting in the following equations

$$\sum_{i=1}^{3} \frac{\partial u_i}{\partial x_i} = 0\,, \tag{3.1}$$

$$\frac{\partial p}{\partial x_j} - \sum_{i=1}^{3} \left(\mu \frac{\partial^2 u_j}{\partial x_i^2} \right) = f_j \quad \text{for } j = 1, 2, 3. \tag{3.2}$$

---

[54] B.J. Kirby. *Micro- and Nanoscale Fluid Mechanics: Transport in Microfluidic Devices.* Cambridge University Press, 2010.

[55] L.G. Leal. *Advanced Transport Phenomena: Fluid Mechanics and Convective Transport Processes.* Cambridge Series in Chemical Engineering Cambridge University Press, 2010.

[29] D. Arumuga Perumal & Anoop K. Dass. *Alex. Eng. J.*, **54**: 955 –971, 2015.

[56] Xiaowen Shan. *IMA J. Appl. Math.*, **76**: 650–660, 2011.

We used the open-source computing platform FEniCS[57,58] for solving the Stokes equation and an in-house solver for the LBM.[59–61]

3.4.2 Computation of the mass transport

The two different approaches presented in this part can be used to simulate mass transport in porous media. The first approach, the MVA is based on the solution of the volume-averaged convection-diffusion equation.[41–43] The second approach uses Brownian dynamics and is based on the solution of the Langevin equation for passive tracers.[22,46–48]

Dispersion via the method of volume averaging

Here, we considered the fluid domain Ω_f with boundary $\partial\Omega_f = \partial\Omega_{fe} \cup \partial\Omega_{fs}$. $\partial\Omega_{fe}$ stands for the entrances and exits of the fluid phase, whereas $\partial\Omega_{fs}$ represents the fluid-solid interface. For the fluid domain, the microscale convection-diffusion equation for mass transport of a scalar (i.e., point-wise) species A is given by

$$\frac{\partial C_A}{\partial t} + \sum_{i=1}^{3} u_i \frac{\partial C_A}{\partial x_i} = \sum_{i=1}^{3} D_\infty \frac{\partial^2 C_A}{\partial x_i^2}, \text{ in } \Omega_f \tag{3.3}$$

$$-\sum_{i=1}^{3} n_i D_\infty \frac{\partial C_A}{\partial x_i} = 0\,, \text{ at } \partial\Omega_{fs} \tag{3.4}$$

$$C_A = C_e(x_i, t)\,, \text{ on } \partial\Omega_{fe} \tag{3.5}$$

$$C_A = C_0(x_i)\,, \text{ when } t = 0 \tag{3.6}$$

In the above equations, C_A is the molar concentration of species A, D_∞ the unbounded diffusion coefficient (or mixture diffusion coefficient in case of a mixture), u_i the velocity field. The subindex i represents the elements of the velocity vector in Cartesian coordinates, e.g. $u_i = (u_x, u_y, u_z)$.

After applying the MVA to the microscopic convection-diffusion equation,[41] we obtain the following upscaled equation for the case of a homogeneous porous medium[41,43]

---

[57] Martin S. Alnæs et al. *ACM T. Math. Software*, **40**: , 2014.

[58] Martin S. Alnæs et al. *Arch. Num. Software*, **3**: , 2015.

[59] Xiaoyi He & Li Shi Luo. *Phys. Rev. E*, **55**: 6811–6820, 1997.

[60] Sauro Succi. *The Lattice Boltzmann Equation for Fluid Dynamics and Beyond (Numerical Mathematics and Scientific Computation)*. Numerical mathematics and scientific computation Oxford University Press, USA, 2001.

[61] Dieter A. Wolf-Gladrow. *Lattice-gas cellular automata and lattice Boltzmann models : an introduction*. Springer, 2000. 308

$$\frac{\partial \langle C_A \rangle^f}{\partial t} + \sum_{i=1}^{3} \langle u_i \rangle^f \frac{\partial \langle C_A \rangle^f}{\partial x_i} = \sum_{i=1}^{3} \frac{\partial}{\partial x_i} \left(D_{ij}^* \frac{\partial \langle C_A \rangle^f}{\partial x_j} \right) , \tag{3.7}$$

with $j = 1, 2, 3$, and dispersion tensor D_{ij}^*

$$D_{ij}^* = D_\infty \left(\delta_{ij} + \frac{1}{\Omega_f} \int\limits_{\partial \Omega_{fs}} n_i b_j^* \, dA \right) - \langle \tilde{u}_i b_j^* \rangle . \tag{3.8}$$

where $\tilde{u}$ stands for the spatial deviation of the velocity field, b_i^* is the associated closure variable and δ_{ij} the identity matrix.

Closure variable The closure variable solves the following boundary-value problem in a representative periodic cell.[42,43]

$$\sum_{i=1}^{3} u_i \frac{\partial b_j^*}{\partial x_i} = \sum_{i=1}^{3} \left(D_\infty \frac{\partial^2 b_j^*}{\partial x_i^2} \right) - \tilde{u}_j, \ \text{ in } \Omega_f \tag{3.9}$$

with boundary and periodicity conditions for the fluid phase

$$-\sum_{i=1}^{3} n_i D_\infty \frac{\partial b_j^*}{\partial x_i} = n_j D_\infty, \ \text{ at } \partial \Omega_{fs} \tag{3.10}$$

$$b_j^*(x_k + l^k) = b_j^*(x_k), \ \ k = 1, 2, 3, \tag{3.11}$$

and following constraint, which is needed for numerical stability and consistency

$$\langle b_j^* \rangle^f = 0. \tag{3.12}$$

This closure problem (Eq. 3.9-3.12) can be interpreted as a transport equation describing the convective and diffusive transport of the vectorial entity b_i^* with two sources. On the one hand, we have a convective volume source being the velocity deviation field $\tilde{u}$. This source can be negative or positive depending on the deviation of the local velocity with respect to the average velocity. In fact, its average over the volume of the fluid phase Ω_f is zero.[41] On the other hand, we have a diffusive surface source $n_i D_\infty$ whose sign depends on the orientation of the normal vector n_i. Similarly, the average value of the surface source over $\partial \Omega_{fs}$ is zero.[41]

The effective diffusivity D_{ij}^{eff} and diffusive tortuosity τ_{ij} are defined using the MVA with the diffusion equation, i.e., Eq. 3.3-3.6 for the case of no convection $u_i = 0$, as follows (see averaging procedure by Whitaker in[41])

$$D_{ij}^{\text{eff}} = \frac{D_\infty}{\tau_{ij}} = D_\infty \left(\delta_{ij} + \frac{1}{\Omega_f} \int\limits_{\partial\Omega_{fs}} n_i b_j \, dA \right) , \tag{3.13}$$

where the closure variable b_i is obtained from the boundary-value problem

$$0 = \sum_{i=1}^{3} \left(D_\infty \frac{\partial^2 b_j}{\partial x_i^2} \right) , \text{ in } \Omega_f \tag{3.14}$$

$$-\sum_{i=1}^{3} n_i D_\infty \frac{\partial b_j}{\partial x_i} = n_j D_\infty, \text{ at } \partial\Omega_{fs} \tag{3.15}$$

$$b_i(x_k + l^k) = b_i(x_k), \;\; k = 1, 2, 3, \text{ periodicity.} \tag{3.16}$$

Note that this implies that the diffusive tortuosity only depends on the geometry of the porous structure. Further, from the definition of the dispersion tensor (Eq. 3.8), one can conclude that dispersion not only depends on the geometry of the porous medium but also on the spatial deviation of the velocity. In fact, for high Péclet numbers, the axial component of the dispersion tensor (here D_{xx}) is strongly dominated by the velocity deviation, as shown in the results section of this paper. Notice that dispersive transport is not directly the superposition of convective and diffusive transport but rather the combined dispersive effect of the spatial deviation of the velocity and diffusion. A simple scenario to illustrate this phenomenon is a (non-viscous) plug flow where we will not observe any enhancement of the dispersive effect by increasing the Péclet number as the spatial deviation of the velocity field is zero. In contrast, in case of viscous pipe flow the dispersive effect of the diffusive transport is combined to that of the deviation of the velocity with respect to the mean flow velocity. The latter case is known as Taylor dispersion.[62]

As a descriptor for the hydrodynamic dispersion we have to use one that evaluates the velocity field. The hydraulic tortuosity τ_h was used to describe the anisotropy of porous structures correlating it with e.g. the permeability tensor.[49–53] We have computed the hydraulic tortuosity according to the following equation.[63,64]

$$\tau_{h_x} = \frac{\langle \sqrt{u_x^2 + u_y^2 + u_z^2} \, \rangle}{\langle |u_x| \rangle} \tag{3.17}$$

In order to solve the closure problems for b^* and b, we extended the FEM-based FEniCS solver.[57,58] Thus, after computing the velocity and velocity deviation fields (u_j and $\tilde{u}_j$), the results are given as input to the b^*-solver.

---

[62] R. ARIS. *P. Roy. Soc. A. Math. Phy. A*, **235**: 67–77, 1956.
[63] A. KOPONEN et al. *Phys. Rev. E*, **54**: 406–410, 1996.
[64] ARTUR DUDA et al. *Phys. Rev. E*, **84**: 036319, 2011.

Dispersion via Brownian dynamics

We define the equation of motion of a tracer with position x_i and velocity v_i, which moves in the fluid phase through the porous network. This is given by the Langevin equation

$$m\frac{\partial v_i}{\partial t} = \sqrt{2\gamma_s\, k_\mathrm{B}T}W_i(t) - \gamma_s\,(v_i - u_i) - \frac{\partial U}{\partial x_i}\,, \quad i = 1,2,3, \tag{3.18}$$

where m is the mass of the tracer, γ_s is the drag coefficient, and $U(x_i)$ the particle interaction potential whose negative gradient $-\partial U/\partial x_i$ represents the force induced by the potential. T and k_B stand for the temperature and Boltzmann constant, respectively.

The first term on the right side of the equation represents the thermal-driving force whose stochastic behavior is modeled by Gaussian noise $W_i(t)$, a normally distributed random number with zero mean $\mu = 0$ and variance $\sigma^2 = 1$.[24,25] The thermal force accounts for the effect of the solvent on the tracer.

The second term on the right represents the drag force, which is proportional to the relative velocity of the particle with respect to the bulk flow $(v_i - u_i)$.

Here, inertial effects can be neglected since the time scale considered spans from the inertial ballistic regime all the way to the diffusive regime.[23,65] This is supported by the fact that the average motion of a Brownian particle over time and the average over the particle ensemble are analogous according to the ergodic hypothesis,[66,67] because all effective quantities computed are an average over the total number of tracers. Furthermore, no interaction potential U is considered since we want to model transport of passive scalars as in the case of the volume-averaged convection-diffusion equation discussed in the previous section. Applying these simplifications and the term $v_i = \frac{dx_i}{dt}$ the equation of motion can be rewritten to

$$0 = \sqrt{2\gamma_s\, k_\mathrm{B}T}W_i(t) - \gamma_s\left(\frac{dx_i}{dt} - u_i\right)\,, \tag{3.19}$$

with initial conditions as follows

$$x_i = X_{0,i}\,, \ \text{ when } \ t = 0\,, \tag{3.20}$$

$$v_i = V_{0,i}\,, \ \text{ when } \ t = 0\,, \tag{3.21}$$

---

[24] H G SCHUSTER & WOLFAM JUST. *Deterministic Chaos.* Wiley, 1994.

[25] GIORGIO VOLPE & GIOVANNI VOLPE. *Am. J. Phys.*, **81**: 224–230, 2013.

[23] HECTOR RUSINQUE et al. *J. Aerosol Sci.*, **129**: 28–39, 2018.

[65] XIN BIAN et al. *Soft Matter*, **12**: 6331–6346, 2016.

[66] L. BOLTZMANN. *Vorlesungen über Gastheorie (translated into English as "Lectures on Gas Theory".)* Vorlesungen über Gastheorie J. A. Barth, 1898.

[67] W. M. DEEN. *AIChE Journal*, **33**: 1409–1425, 1987.

where $X_{0,i}$ and $V_{0,i}$ are vectors containing the initial positions and velocities, respectively. Note that in Brownian dynamics (BD) the temperature can be controlled as with a thermostat, thus approximating the canonical ensemble. The above initial-value problem was numerically integrated by applying the leapfrog method[68] using an in-house C++ code parallelized with MPI and OpenMP. The velocity field of the bulk flow u_i was taken from the solution of the LBM.

By tracking the position of the particles with the Lagrangian method, one can compute the mean square displacement $\langle \Delta x_{ij}^2(t) \rangle$ of the particle ensemble

$$\langle \Delta x_{ij}^2(t) \rangle = \frac{1}{N} \sum_{n=1}^{N} (x_i^n(t) - \langle x_i(t) \rangle)(x_j^n(t) - \langle x_j(t) \rangle) , \qquad (3.22)$$

where $\langle ... \rangle$ indicates averaging over the tracer ensemble and N is the number of tracer particles. From its time derivative, the elements of the dispersion tensor D_{ij} can be calculated[69]

$$D_{ij} = \frac{1}{2} \frac{d}{dt} \langle \Delta x_{ij}^2(t) \rangle . \qquad (3.23)$$

Notice that the off-diagonal elements of the dispersion tensor (D_{ij} for $i \neq j$) vanish when the axial and radial axes of the diffusion ellipsoid coincide with the frame of reference of the diagonal terms of the tensor.[70] In the present work this is approximately the case, since the axial axis of the diffusion ellipsoid is predetermined by the selected main direction of the bulk flow.

In this study, only the transport of passive scalar tracers is considered. Deviations from scalar transport can be observed, e.g. when the pore size comes too close to the tracer particle size,[22,67,71] or the tracer shape diverges strongly from a sphere, as well as when pairwise interactions between the diffusing particles are strong and cannot be neglected.[72–74]

3.5 Results and discussion

3.5.1 Mass transport in homogeneous porous media: Comparison of the MVA and BD approaches

The flow through an arrangement of in-line cylinders is considered (see Fig. 3.1). The porosity was varied by increasing the cylinder diameter.

---

[68] GUIHUA ZHANG & TAMAR SCHLICK. *Mol. Phys.*, **84**: 1077–1098, 1995.

[69] N. HOZE & D. HOLCMAN. *bioRxiv*, 227090, 2017.

[70] D.K. JONES. *Diffusion MRI.* Oxford University Press, 2010.

[71] PANADDA DECHADILOK & WILLIAM M. DEEN. *Ind. Eng. Chem. Res.*, **45**: 6953–6959, 2006.

[72] ROBERT EVANS et al. *Anal. Chem.*, **90**: 3987–3994, 2018.

[73] JIE XIAO & XIAO DONG CHEN. *AIChE Journal*, **60**: 2416–2427, 2014.

[74] PETR DVOŘÁK et al. *Mol. Phys.*, **8976**: , 2018.

As required by the definition of the closure variables b and b^* in the MVA, the system consists of a representative periodic unit cell of the homogeneous porous medium considered. The relative values of the radial and axial dispersion coefficients with respect to the free (unbounded) diffusion coefficient (D_{xx}/D_∞ and D_{yy}/D_∞, respectively) were determined with increasing Péclet number (ratio of convection to diffusion).

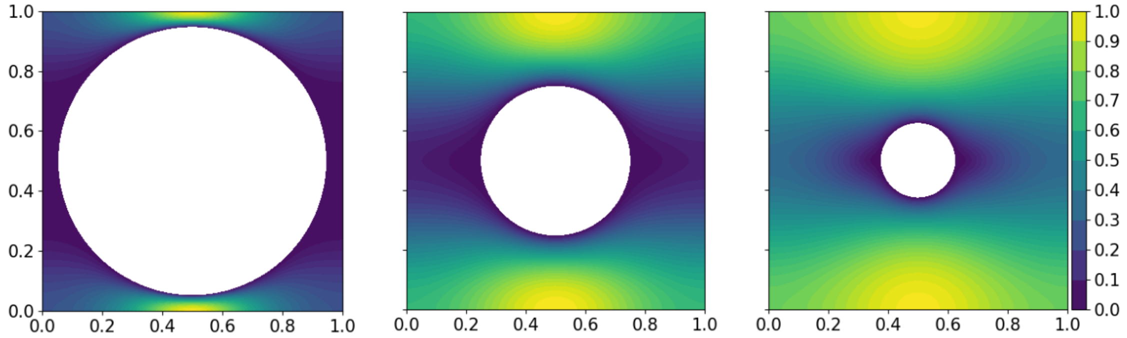

(a) $\varepsilon = 0.37$ **(b)** $\varepsilon = 0.80$ **(c)** $\varepsilon = 0.95$

Figure 3.1: Periodic unit cell of the in-line cylinder arrangements with a graphic representation of the velocity field for three porosity values. The distance in the x and y axes, and velocities were normalized by the maximal magnitude of the distance and velocity field, respectively, and are hence dimensionless. ε stands for the porosity of the cells

Dispersion regimes

Low Péclet numbers $\mathrm{Pe} < 1$ (i.e., low bulk-flow velocities) this dispersion regime is controlled by diffusion, as convection is weak here. Thus, in this range, the value of the dispersion coefficients is determined solely by the geometry of the porous structure, making the diffusive tortuosity the descriptor par excellence for this region. In fact, the relative dispersion coefficients, D_{xx}/D_∞ and D_{yy}/D_∞, converge to the reciprocal value of the diffusive tortuosity (τ_{xx}^{-1} and τ_{yy}^{-1}) as the Péclet number (Pe) goes to zero. This can be clearly seen in Figure 3.3 in comparison to the values of the diffusive tortuosity shown in Table 3.1. The diagonal components of the tensor of diffusive tortuosity τ_{ii} assume the same value since the porous medium is isotropic, i.e., $\tau_{xx} = \tau_{yy}$.

The diffusive tortuosity is related to the degree of diffusive paths obstructed by obstacles (the solid boundaries of the pores). For this reason, its reciprocal value is also known in literature as obstruction factor. In general, the diffusive tortuosity has a hindering effect on dispersion, i.e., the higher the tortuosity the lower the value of the dispersion coefficient in this diffusive regime (see Eqn. 3.13).

High Péclet numbers $\mathrm{Pe} > 1$ (i.e., high bulk-flow velocities) Here the axial dispersion is dominated by the spatial deviations of the velocity field. Two main dispersion phenomena can be distinguished that are caused by these spatial deviations. The first is due to velocity gradients between the different stream paths along the porous medium (e.g. trans-column, trans-channel, inter-channel, and Taylor dispersion[62]). The second effect is induced by the splitting of the flow paths and is known as mechanical dispersion. These phenomena have an enhancing effect on the dispersion coefficients.

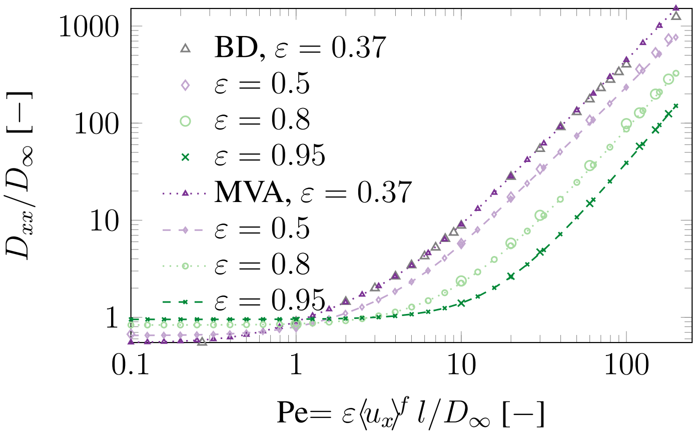

Figure 3.2: Axial dispersion coefficients as a function of the Péclet number in the in-line cylinder arrangements considered.

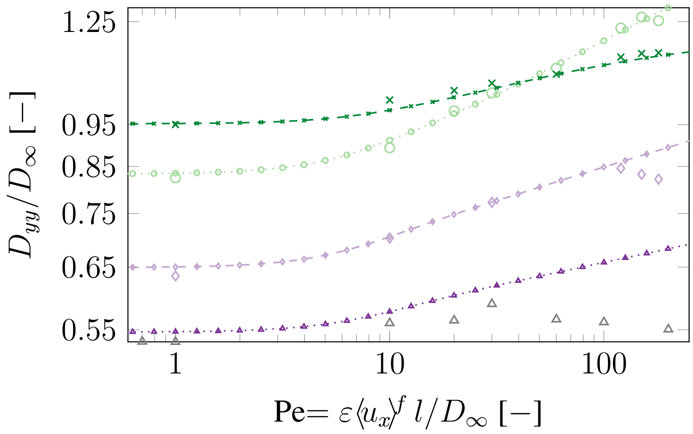

Figure 3.3: Radial dispersion coefficients as a function of the Péclet number in the in-line cylinder arrangements considered (see legend in Figure 3.2).

Since the velocity field is the determining parameter in this hydrodynamic regime, we will try to establish a connection between the dispersion coefficient and the hydraulic tortuosity in the next section.

Diffusive vs. hydraulic tortuosity

The diffusive and hydraulic tortuosity values are shown in Table 3.1. It is observed that an increase in porosity leads to a higher diffusive tortuosity, which inversely correlates with the dispersion coefficient in the diffusive regime $(\mathrm{Pe} < 1)$ as explained above. Regarding the hydrodynamic regime, at $\mathrm{Pe} > 1$, an increase of the hydraulic tortuosity is likewise observed as the porosity increases. Here, the axial dispersion coefficient increases with increasing hydraulic tortuosity and increasing porosity. This correlation is so strong that the order of the axial dispersion coefficients by porosity reverses at about $\mathrm{Pe} = 1$. However, the sensitivity of the hydraulic tortuosity is very small as can be seen from the fact that the hydraulic tortuosity decreases only slightly by the increase of porosity.

The radial dispersion coefficient shows a more complex behavior, as the radial velocities of the bulk flow are significantly lower than the axial velocities. Consequently, at high Péclet numbers both the spatial deviation of the velocity as well as the diffusion determine the dispersive transport.

Table 3.1: Selected descriptors of the porous structure of the in-line cylinders. The diffusive tortuosity values presented were computed with the MVA approach.

$\varepsilon\,[-]$	$\tau_{xx}^{-1}\,[-]$	$\tau_{xx}\,[-]$	$\tau_{h_x}[-]$
0.37	0.545	1.83	1.0196
0.50	0.649	1.54	1.0192
0.80	0.833	1.20	1.0189
0.95	0.952	1.05	1.0143

MVA vs. BD

As shown in Fig. 3.2 and 3.3, the results delivered by both methods are in good agreement with each other. Only in the case of the radial dispersion at $\varepsilon = 0.37$ (see Fig. 3.3) a slight discrepancy was observed. This might be explained by the fact that the geometry used in the BD approach shows a higher diffusive tortuosity of 1.88 (as can bee seen in Fig. 3.2 as the Pe number approaches zero), as opposed to the tortuosity value of 1.54 obtained in the MVA approach. Another explanation may be the slight differences in the geometry of the system due to the different discretization methods used/related in/to each approach.

Both approaches are able to deal with homogeneous porous media. In terms of computational performance MVA is significantly faster, since only one set of differential equations is solved for each calculation of the dispersion coefficient at a given Péclet number. Just as expected from a deterministic differential equation, MVA always delivers the same numerical results which are subject to classical numerical errors, e.g. involving the number of nodes of the mesh. In contrast, when using BD we have to solve the equation of motion for each particle of the ensemble considered in the calculations. We compute the trajectories of 10^6 tracers so that the fluctuations in the solution do not alter the first three significant digits of the dispersion coefficient and diffusive tortuosity values. Furthermore, the BD approach can handle mass transport in heterogeneous porous media, since no representative periodic unit cell is needed. This method is ideal for small systems where boundary effects cannot be neglected. In addition, when the BD method is used in combination with the LBM, we get a mesh-free simulation approach, which can be of great advantage for complex geometries.

3.5.2 Mass transport in heterogeneous porous media: Confinement effects

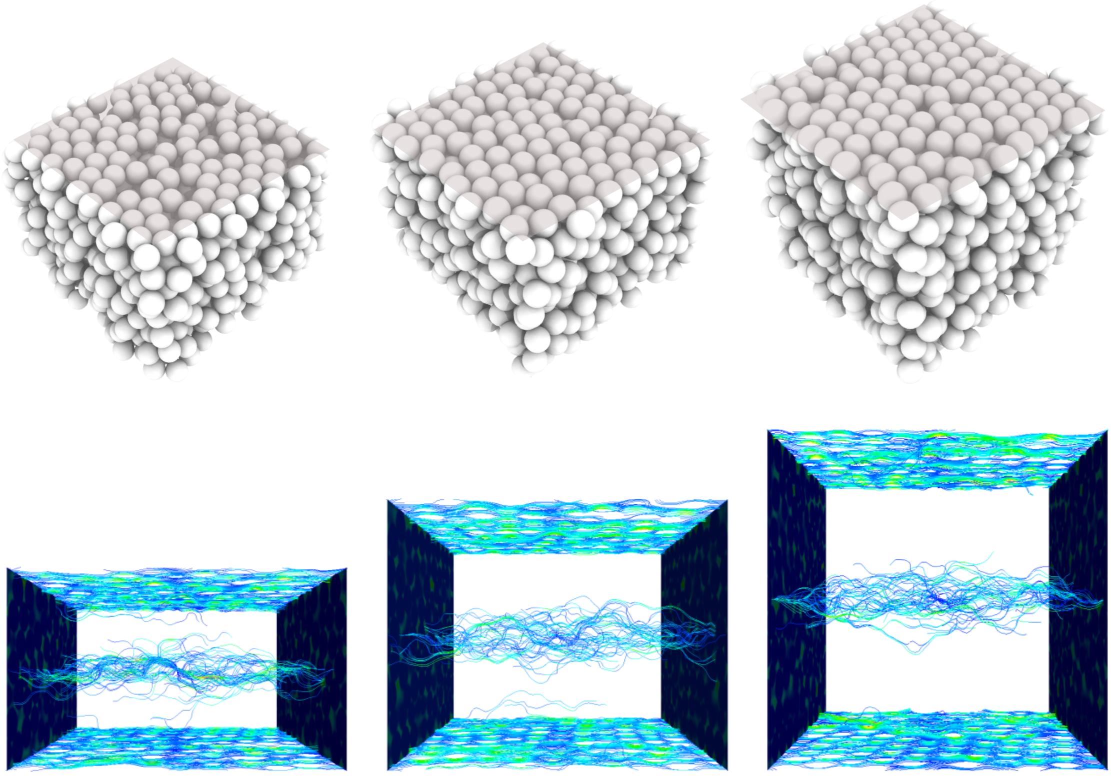

(a) $H/d = 6$ (b) $H/d = 8$ (c) $H/d = 10$

Figure 3.4: At the top the sphere packings of finite H/d-ratios are shown. Below, characteristic pathlines close to the wall $(z \approx 0)$ and in the middle of the packing $(z = H/2)$ are plotted for each packing, respectively.

This section outlines the dispersion in heterogeneous porous structures consisting of confined random sphere packings. Confinement effects on mass transport are particularly important in column chromatography and can be split into two effects. The first one is directly related to the highly ordered structure present in the immediate vicinity of the wall, as opposed to the highly disordered configuration present in the bulk of the packing, known as random close packing (RCP).[75] This effect alters the tortuosity of the pathlines affecting the mechanical dispersion. The second wall effect emerges from the steep velocity gradient induced by the presence of the wall, which in turn has an enhancing effect on the hydrodynamic dispersion. This contribution to dispersion is also known as trans-column dispersion in literature.[76]

---

[75] R. Andrew Shalliker et al. *J. Chromatogr. A*, **888**: 1–12, 2000.

The investigated packings were generated numerically with different ratios of packing height to sphere diameter H/d (see Fig. 3.4, which takes part of the images published in the Master thesis by Rusinque [77]). The dispersion coefficients at different Péclet numbers were computed using the BD approach. The packings were generated using the open-source software RCP provided by Desmond et al.[78] In contrast to the previous case, here the effective porosities were set approximately constant at 0.375 ± 0.005. Each diameter was spatially resolved with 35 lattice cells. The results of the dispersion coefficients are shown in Fig. 3.5 and 3.6.

Confinement effect

The confinement effect on the arrangement of the spheres can be seen in Fig. 3.4. Here, as mentioned above, the walls constrain the spheres to a highly ordered arrangement. The influence of the walls on the structure of the medium is in the range of 4 to 5 sphere diameters.[79] Outside this region, the characteristic structural disorder of a RCP configuration prevails. This effect can be seen in the porosity profile along the axis perpendicular to the walls (here referred to as the z-axis) of the generated packings: the porosity profiles are supported by the projections of the sphere centers right below each profile in Fig. 3.8.

---

[76] Stefan Bruns et al. *J. Chromatogr. A*, **1318**: 189–197, 2013.

[77] Hector Rusinque et al. *Skalenauflösende Berechnung der Diffusion und hydrodynamischen Dispersion in inhomogenen porösen Medien.* Technische Universität Clausthal, 2016.

[78] Kenneth W. Desmond & Eric R. Weeks. *Phys. Rev. E*, **80**: 051305, 2009.

[79] Robert S. Maier et al. *Phys. Fluids*, **15**: 3795–3815, 2003.

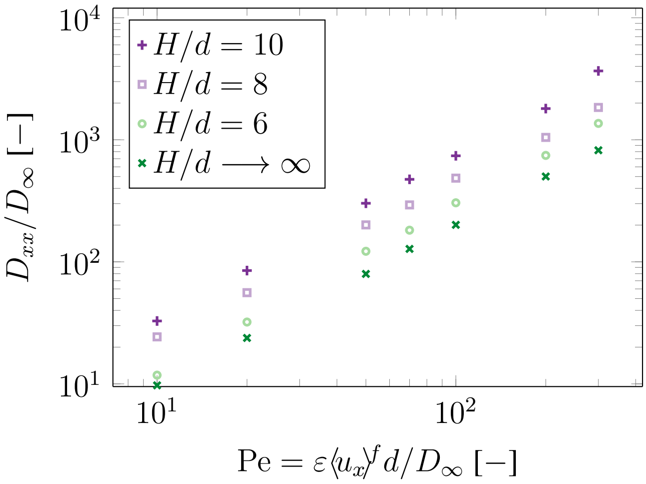

Figure 3.5: Axial dispersion coefficients as a function of the Péclet number in the sphere packings considered.

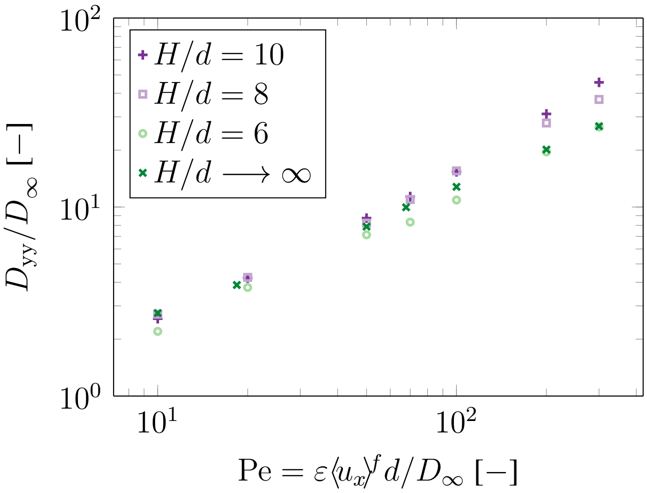

Figure 3.6: Radial dispersion coefficients as a function of the Péclet number in the sphere packings considered.

The narrowest packing examined in this study has a height of 6 sphere diameters which is why the entire packing is characterized by an ordered structure. The case of an unconfined sphere packing, i.e. $H/d \longrightarrow \infty$, is modeled by introducing periodic boundary conditions. The porosity profile of the narrowest packing shows pronounced fluctuations that are regularly spaced along its entire extent in the z-axis (see Fig. 3.8a), whereas the porosity fluctuations of the periodic packing are smaller and homogeneously distributed, see Fig. 3.8d.

To illustrate how the difference in structural disorder between these two extreme cases affects the convective motion of the tracers, we plotted pathlines near the wall at $z \approx 0$

and those in the middle of the packing at $z = H/2$ (see Fig. 3.4 and 3.7). The pathlines of the periodic packing ($H/d \longrightarrow \infty$) were also graphically depicted in Fig. 3.7e.

The packings with H/d ratios of 8 and 10 have different volume proportions of ordered and disordered pore regions. The presence of two pore regions with different structures in the same packing leads to the development of two significantly different flow conditions in each region, which results in strongly heterogeneous velocity profiles; heterogeneous not only in terms of magnitude but in the tortuosity of the stream paths along the pore network. This in turn leads to a strong dispersion of the diffusing tracers, i.e., to large dispersion coefficients. Both, the infinitely extended packing and the narrowest packing have mainly only one characteristic pore region, i.e., a lesser degree of heterogeneity, which explains their lower dispersion coefficients (see Fig. 3.5 and 3.6). Similar results were obtained in the experimental work of Bruns et al., 2013, for column chromatography with varying ratio of the column diameter to the mean particle diameter.[76]

Diffusive vs. hydraulic tortuosity

Regarding the selected descriptors, the diffusive tortuosity remains approximately constant around 1.4 for all the packings considered, see Table 3.2. This is a direct consequence of the fact that the effective porosity was set as constant. These results show the strong correlation of the diffusive tortuosity with the effective porosity of the sphere packings.

Table 3.2: Selected descriptors of the porous structure of the sphere packings. The tortuosity values have a standard deviation of 0.03.

$H/d\ [-]$	$\tau_{xx}^{-1}\ [-]$	$\tau_{xx}\ [-]$	$\tau_{h_x} [-]$
6	0.694	1.44	1.2328
8	0.694	1.44	1.2455
10	0.694	1.44	1.2486
∞	0.685	1.46	1.2723

In contrast, the hydraulic tortuosity increases slightly with increasing packing height. However, as the descriptors are average (effective) values, neither of them is suitable to capture the contribution of the heterogeneity in the structure to the dispersive mass transport. As opposed to the homogeneous case, where the hydraulic tortuosity directly correlates with the dispersion coefficient, here an indirect correlation between these two parameters is observed, meaning that the porous structure with the largest value of hydraulic tortuosity showed the smallest dispersion coefficient, namely the unconfined sphere packing with $H/d \longrightarrow \infty$.

From the results it can be deduced that in cases where heterogeneity is strongly pronounced in the structure of a porous medium, effective descriptors are not well suited to describe the dispersive mass transport in the medium. Instead, a spatial distribution or a probability distribution of the local hydraulic tortuosity could be used, whose standard deviation captures the degree of heterogeneity of a porous medium. A spatial distribution can be achieved by applying Eq. 3.17 to each plane along a selected axis, from which a tortuosity profile could be represented (analogous to the porosity profiles in Fig. 3.8). A probability distribution could be attained by calculating the tortuosity and occurrence of individual pathlines. These pathlines can be obtained e.g. using a particle tracking method.

According to the results, the degree of heterogeneity of a porous medium governs dispersion against the (effective) diffusive and hydraulic tortuosity in confined sphere packings at high Péclet numbers.

In a qualitative analysis, we can take the values of the narrowest confined packing $H/d = 6$ and the unconfined packing $H/d \longrightarrow \infty$ as characteristic tortuosity values of the wall and bulk regions of a packing, respectively. Here, the wall region is to be understood as the region where the ordered configuration induced by the wall is present, whereas the bulk region is the region in which the RCP configuration is found. So we can express the hydraulic tortuosity of the larger confined packings as the volume-weighted average of the characteristic tortuosity values. In this way, the degree of heterogeneity is related to the volume fractions of each characteristic region, where a volume fraction of one or zero indicates a homogeneous medium.

3.6 Conclusions

With the presented approaches we were able to determine and discuss the transport properties of the homogeneous and heterogeneous porous media considered. In the structured geometry of the homogeneous case, a clear correlation of the dispersive transport properties of the media with their tortuosity and effective porosity values can be seen, as opposed to the heterogeneous case, where there is no direct correlation between the considered parameters. The reason is attributed to the fact that the used descriptors are effective values not capable of capturing the dispersive effect induced by the degree of heterogeneity in the microscopic porous structure. Instead of effective parameters, the use of a local hydraulic tortuosity is proposed, the implementation of which will be left to future work.

In addition, the MVA and BD approaches were compared in the section of homogeneous porous media. Here, the method of volume average outperformed Brownian dynamics in terms of both precision and computational performance.

Acknowledgment: The authors appreciate the support for this project by the North-German Supercomputing Alliance (HLRN) as well as by the Lower Saxony Ministry of Science and Culture within the PhD program "Self-organizing multifunctional structures for adaptive high performance light-weight constructions". The framework of this coordinated program is the "Campus for Functional Materials and Functional Structures", an institution of the Clausthal University of Technology (TUC) in collaboration with the DLR, German Aerospace Center, in Braunschweig, the BAM, Federal Institute for Material Testing, in Berlin, and the Technical University of Braunschweig (TU BS).

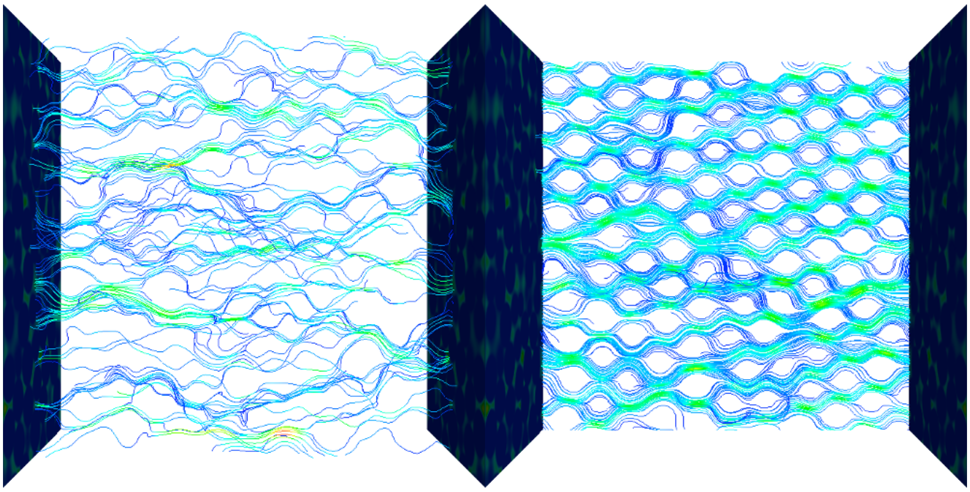

(a) $z = H/2$, xy top view (b) $z \approx 0$, top view

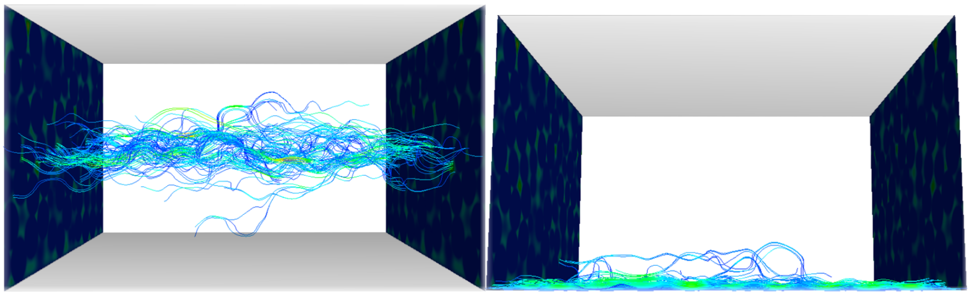

(c) $z = H/2$, front view (d) $z \approx 0$, front view

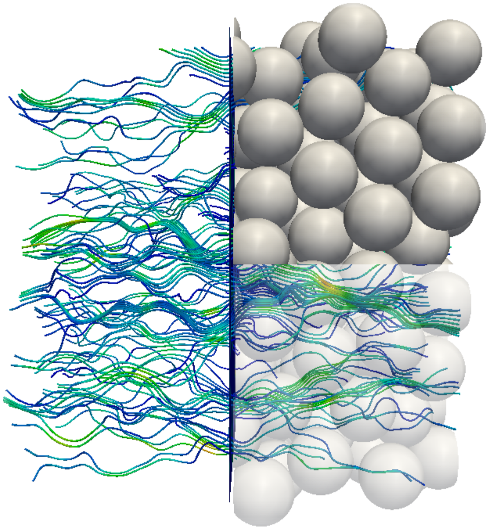

(e) $H/d \longrightarrow \infty$

Figure 3.7: (a)–(d) show selected views of the pathlines in the sphere packing with $H/d = 6$: close to the wall at $z \approx 0$ in (b) and (d), and in the middle of the packing at $z = H/2$ in (a) and (c). Additionally in (e), a portion of the periodic sphere packing and its related pathlines are presented.

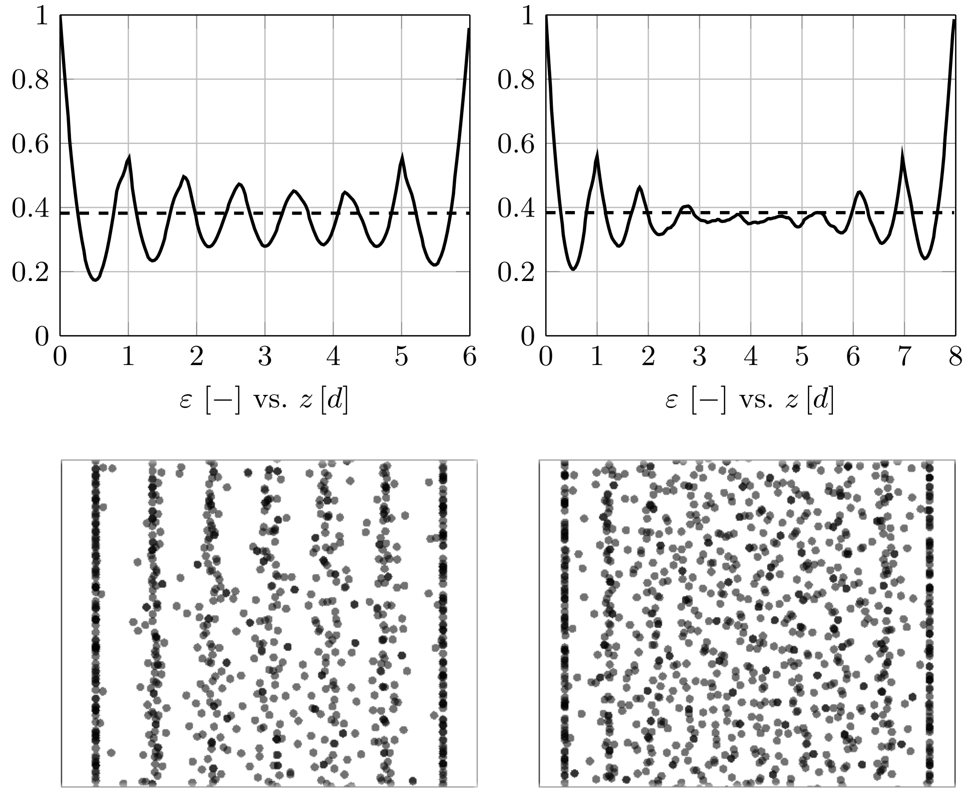

(a) $H/d = 6$ (b) $H/d = 8$

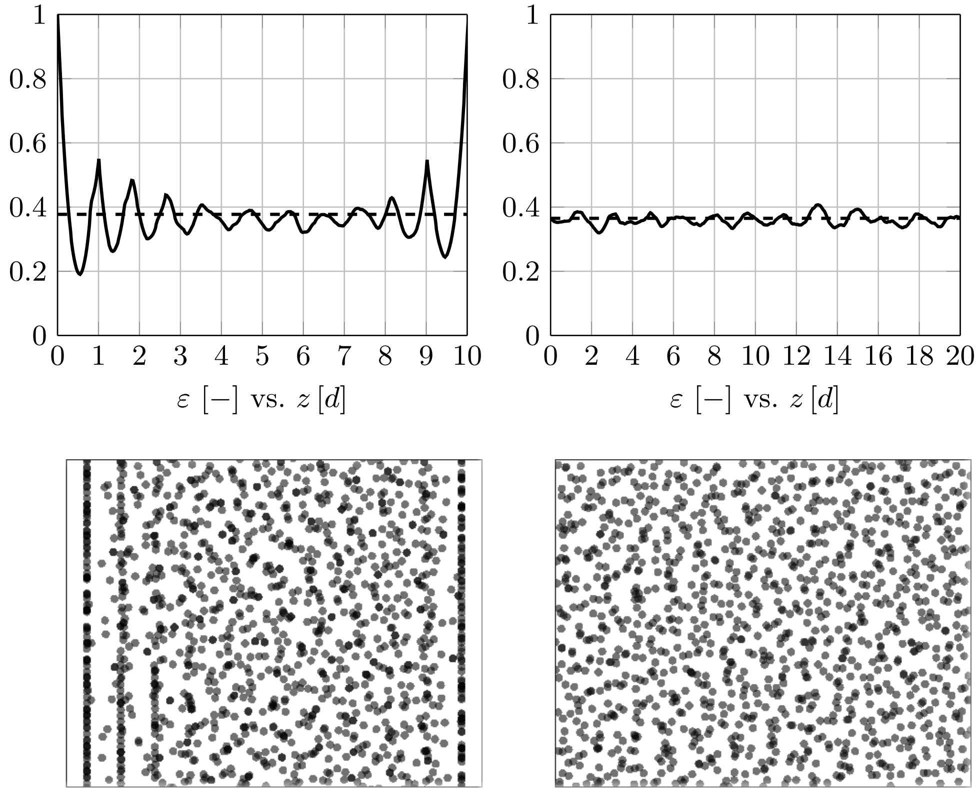

(c) $H/d = 10$ (d) $H/d \longrightarrow \infty$

Figure 3.8: Porosity profiles along the z-axis and projections of the sphere centers on a plane perpendicular to the walls, also along the z-axis from left to right.

4 Hindering effect of pore size on mass transport in porous media

This chapter was published in the form of a full paper in the scientific journal of Microporous and Mesoporous Materials

Hector Rusinque and Gunther Brenner (2019).
Mass transport in porous media at the micro- and nanoscale: A novel method to model hindered diffus
DOI: 10.1016/J.MICROMESO.2019.01.037 .

4.1 Zusammenfassung

Im vorliegenden Kapitel wird eine Methode zur Beschreibung des Massentransports in porösen Medien vorgestellt. Ingenieurwissenschaftliche Ansätze zur Beschreibung des Massentransports basieren auf MittelwertgröSSen wie dem effektiven Diffusionskoeffizienten.[80] Dieser unterscheidet sich vom (Bulk-)Diffusionskoeffizienten, da er externe Faktoren berücksichtigt, welche die Bewegung der diffundierenden Moleküle beeinflussen, z. B. die sterische Hinderung, die Tortuosität und die durch Konvektion bedingte Dispersionsverstärkung.

Der hier vorgestellte Ansatz basiert auf einer porenskaligen Simulation der Transportprozesse, die im Hohlraum eines nanoporösen Materials ablaufen. Dies erfordert eine räumliche Auflösung auf der Nanoskala, wo herkömmliche kontinuumsmechanische CFD-Modelle versagen können.Stattdessen wird die Lattice-Boltzmann-Methode (LBM) verwendet, um Mikro- und Nanoströme zu berechnen.[29,56] LBM ist ein partikelbasierter probabilistischer Ansatz, der eine diskretisierte Form der Boltzmann-Gleichung löst, d. h. eine Transportgleichung für seine primär zu untersuchende Variable: die Ein-Partikel-Wahrscheinlichkeitsverteilungsfunktion (PPDF, vom englischen "one-particle probability distribution function"). Nach Integration der Transportgleichung über den Phasenraum wird ein Kollektiv von wechselwirkenden Teilchen rekonstruiert. Dessen zentraler Term ist der Kollisionsterm, der die vom Modell angewandten Wechselwirkungsregeln vorgibt, z. B. nur binäre Kollisionen und die Annahme von molekularem Chaos (siehe Kapitel 4.1). In einem nachfolgenden Simulationsschritt wird das aus dem LBM-Solver gewonnene Geschwindigkeitsfeld (die ortabhängigen Geschwindigkeiten des Lösemittels) als Eingabe für die Bewegungsgleichung der gelösten Moleküle verwendet. In früheren Studien wurden ähnliche Methoden zur Berechnung des Obstruktionsfaktors[81] und der effektiven Diffusivität in porösen Medien[46–48] verwendet, wobei die gelösten Moleküle auf punktweise skalare Tracer reduziert werden. In diesen Methoden wird die Wechselwirkung zwischen den diffundierenden Partikeln und der Porenwand durch spiegelnde oder diffuse Reflexion des Tracers an der Porenwand erfasst. Im Gegensatz dazu wird hier nicht nur die Reflexion an der Wand, sondern auch die hinderliche Wirkung des durch die nahe gelegenen Wandatome induzierten Kraftfeldes auf die Diffusivität der gelösten Moleküle berücksichtigt. Dies wird durch ein neuartiges Wandhinderungsmodell auf Basis des Lennard-Jones-Potentials für den Fall von van-der-Waals-Wechselwirkungen zwischen gelösten Molekülen und Wandatomen modelliert, bei denen keine physikalische Adsorption an den Porenwänden stattfindet. AnschlieSSend wird die Validierung des Modells mit Hilfe von experimentellen und numerischen Daten aus der Literatur erfolgreich durchgeführt.

---

[80] Alexander Bufe et al. *Chem. Ing. Tech.*, **89**: 1385–1390, 2017.
[29] D. Arumuga Perumal & Anoop K. Dass. *Alex. Eng. J.*, **54**: 955 –971, 2015.
[56] Xiaowen Shan. *IMA J. Appl. Math.*, **76**: 650–660, 2011.

Darüber hinaus wird eine Anpassungsfunktion vorgestellt, die zur Abschätzung des Diffusionshinderungsfaktors einer komplexen Geometrie verwendet werden kann, wenn die PorengröSSenverteilung des porösen Netzwerks bekannt ist. SchlieSSlich wird ein Multiskalenansatz vorgestellt und mit einem Anwendungsbeispiel illustriert, wobei die Hindernisfaktoren der Mikro- und Nanoskala in den Simulationen des Stofftransports auf der gröSSeren Skala verwendet werden.

4.2 Abstract

Mass transport in liquid-filled pores at the micro- and nanoscale can play an important role in applications such as membrane separations, chromatography, and catalytic processes. In this work, we use Brownian dynamics in order to describe the motion of spherical solute molecules at a pore-scale. The method can be used to calculate effective parameters intrinsically related to the porous medium such as the effective diffusivity and the hindrance factor for diffusion. The latter is calculated using a novel probabilistic model derived in the present study, which uses the Lennard-Jones potential to reproduce the hindering effect of the interaction between solute molecules and the wall atoms on the diffusivity. In addition, we introduce a fitting function that can be used to estimate the diffusive hindrance factor of a complex geometry when the pore size distribution of the porous network is known. Finally, a multiscale approach is presented and illustrated with

---

[81] Siarhei Khirevich et al. *J. Chromatogr. A*, **1218**: 6489–6497, 2011.
[46] Tobias Heidig et al. *Chem. Ing. Tech.*, **86**: 554–560, 2014.
[47] Siarhei Khirevich et al. *J. Chromatogr. A*, **1217**: 4713–4722, 2010.
[48] Harun Koku et al. *J. Chromatogr. A*, **1237**: 55–63, 2012.

an application example, whereby the hindrance factors of the micro- and nanoscale are used in the simulations of the mass transport at the larger scale.

4.3 Introduction

In this study, a method for the quantification of mass transport in porous media is presented. Engineering approaches to describe mass transport are based on average quantities such as the effective diffusivity.[80] This differs from the (bulk) diffusion coefficient, as it captures external factors influencing the motion of the diffusing molecules, e.g. the steric hindrance, the tortuosity and dispersion enhancement due to convection.

The present approach is based on a pore-scale simulation of the transport processes occurring within the void space of a nanoporous material. This requires a spatial resolution at the nanoscale, where conventional continuum mechanics models can fail. Instead, the Lattice Boltzmann Method (LBM) is used to compute micro- and nanoflows.[29,56] In a subsequent simulation step, the velocity field obtained from the LBM solver is given as input to the equation of motion of the particles (the solute molecules).

In previous studies, similar methods were used to calculate the obstruction factor[81] and the effective diffusivity in porous media ,[46–48] whereby the solute molecules are reduced to pointwise scalar tracers. In these methods, the interaction between the diffusing particles and the pore wall is captured by specular or diffuse reflection of the tracer from the pore wall. In contrast, we consider not only the reflection on the wall but also the hindering effect of the force field induced by the nearby wall atoms on the diffusivity of the solute molecules. This is simulated by means of a novel wall hindrance model based on the Lennard-Jones potential.

The diffusivity of a species is related to its molecule size via the Stokes-Einstein equation $D_\infty = k_B T/\gamma_s$. There are several correction factors found in the literature regarding aspects such as the shape of the solute molecule, degrees of freedom, binding interactions with the solvent itself, and the effect of the solute concentration, among others.[72–74] In this study, only the deviation from unbounded diffusion D_∞ due to the influence of the wall atoms is considered. This influence also accounts for the steric effects that a soft spherical molecule experiences when passing through a narrow pore. The hindrance to diffusion due to particle-wall interactions has been studied mainly for well-defined pore

---

[72] Robert Evans et al. *Anal. Chem.*, **90**: 3987–3994, 2018.

[73] Jie Xiao & Xiao Dong Chen. *AIChE Journal*, **60**: 2416–2427, 2014.

[74] Petr Dvořák et al. *Mol. Phys.*, **8976**: , 2018.

geometries,[71,82–84] as well as for intricate pore networks such as those found in the void space of packed beds[85] or biological tissues.[86] While normally, the hindrance factor for diffusion is given as a function of the reduced molecule diameter $2r_m/x$ (the ratio of the molecule diameter $2r_m$ to the pore size x), in this work we introduce an additional parameter, namely the average bond length among the atoms of the solid phase $\overline{L}_{ww}$ which affects the strength of the particle-wall interactions (see Figure 4.1).

The presented method will be derived and verified by means of experimental data from literature. Based on this, mass transport within straight cylindrical pores and packed beds with different pore scales is considered and effective parameters for the description of this transport phenomenon are discussed.

4.4 Modeling and Numerical Approach

4.4.1 Equation of Motion of a Particle Ensemble: Mass Transport in Pores

There are models that can be used to simulate the mass transport of pointwise passive scalars in complex geometries, such as the Convection-Diffusion equation[87] and the Random Walk Particle Tracking Method.[47] However, the behavior of passive scalars can deviate strongly from that of solute molecules. Our objective here is to derive an equation of motion that can reproduce the steric effects and hindrance to diffusion that an ensemble of solute molecules experiences in bounded spaces.

A system is considered, which consists of three molecular entities, namely spherical solute molecules and wall atoms, as well as solvent molecules. The wall atoms constitute a porous medium whose pores are filled with a liquid consisting of the mixture of solute and solvent molecules. The motion of the solute molecules is induced by their interactions with the other molecular entities and with each other. Here, we assume that the mean strength of the interactions occurring in the solution is the same between all the molecules of the mixture, resulting in the long-range solute-solute interactions approximately canceling each other out (concept of an ideal solution). Furthermore, it is assumed that the solvent molecules are significantly smaller than the solute molecules, so that the the interactions between a solute molecule and the solvent can be modeled according to the fluctuation-dissipation theorem that quantifies the relation between the fluctuations in

---

[71] PANADDA DECHADILOK & WILLIAM M. DEEN. *Ind. Eng. Chem. Res.*, **45**: 6953–6959, 2006.

[82] ROBERT E BECK & JEROME S SCHULTZ. *Biochim. Biophys. Acta*, **255**: 273–3, 1972.

[83] EUGENE M RENKIN. *J. Gen. Physiol.*, **38**: 225–243, 1954.

[84] M. P. BOHRER et al. *Hindered Diffusion of Dextran and Ficoll in Microporous Membranes*. **volume** 17 1984. 1170–1173

[85] CHARLES N. SATTERFIELD et al. *AIChE Journal*, **19**: 628–635, 1973.

[86] JADER ALEAN et al. *J. Food Eng.*, **233**: 28–39, 2018.

[87] C.E. BAUKAL et al. *Computational Fluid Dynamics in Industrial Combustion*. Industrial Combustion Taylor & Francis, 2000.

a system at thermal equilibrium and its response to applied perturbations. When a solute molecule moves through the solvent, it experiences drag, dissipating kinetic energy. The solvent molecules respond to this perturbation by turning the dissipated energy into thermal motion (the corresponding fluctuation). This phenomenon can be used to describe diffusion as given by the Einstein relation (the ratio of the thermal driving force to its counteracting force, the drag)[13]

$$D = \frac{k_B T}{\gamma}. \tag{4.1}$$

The force induced by thermal motion on the particle can be interpreted as a body force equals to the negative gradient of the chemical potential, $-\frac{\partial \mu}{\partial x_i} \approx -\frac{\partial}{\partial x_i}(k_B T \ln C)$,[13] where C stands for the particle concentration. Further, the drag force is proportional to the relative velocity of the solute molecule with respect to the bulk flow velocity with a proportionality factor γ, the drag coefficient. For the special case of an unbounded solution, this coefficient can be modeled by the Stoke's law $\gamma_s = 6\pi\eta r_s$, where η stands for the viscosity of the unbounded solvent and r_s for the hydrodynamic radius of a solute molecule.

With the assumption of an isothermal fluid and considering a particle ensemble consisting of N solute molecules in an unbounded fluid, this yields for the k-th particle

$$m\frac{\partial v_i}{\partial t} = -k_{\mathrm{B}} T \frac{\partial \ln C}{\partial x_i} - \gamma_s \left(v_i - U_i\right), \tag{4.2}$$

where U_i stands for the bulk flow velocity.

After considering the solute-solute and solute-solvent interactions, the only interaction left affecting the motion of a given solute molecule is the interaction with the wall atoms of the porous medium. Here, we assume van der Waals interactions, which can be approximated using the negative gradient of the Lennard-Jones potential φ_w [88]

$$\varphi_w(r_w) = 4\epsilon_{sw}\left[\left(\frac{\sigma_{sw}}{r_w}\right)^{12} - \left(\frac{\sigma_{sw}}{r_w}\right)^{6}\right], \tag{4.3}$$

where r is the distance between two interacting particles, ϵ is the depth of the potential well (usually referred to as 'dispersion energy'), and σ is the distance at which the particle-particle potential energy φ is zero (often referred to as 'size of the particle'). Let us now take a look at how the introduction of the wall field affects the other interactions. The presence of the wall potential changes the chemical environment of the solvent and solute molecular entities. This change has an effect on the chemical potential gradient as well as on the drag exerted by the solvent, both in the radial direction (perpendicular to the wall). Consequently, γ_s must be replaced by a general location-dependent γ. For a finite number of solute-wall interactions (M_k), this leads to the following equation

---

[13] A. EINSTEIN. *Ann. d. Phys.*, **322**: 549–560, 1905.

[88] J. E. JONES. *P. Roy. Soc. A. Math. Phy. A*, **106**: 463–477, 1924.

$$m\frac{\partial v_i}{\partial t} = -k_{\mathrm{B}}T\frac{\partial \ln C}{\partial x_i} - \gamma\,(v_i - U_i) - \sum_{j=1}^{M_k}\frac{\partial \varphi_w(r_w^j)}{\partial x_i}. \tag{4.4}$$

Now, let us define a local diffusion coefficient $D_{\mathrm{local}}(r_w)$ dependent on the distance to the wall r_w, as follows

$$D_{\mathrm{local}}(r_w) = \kappa_d(r_w)D_\infty = \frac{k_BT}{\gamma(r_w)}, \tag{4.5}$$

where $\gamma(r_w)$ consists of the wall potential-independent drag γ_s and a wall potential-dependent term $\kappa_d(r_w)$,

$$\gamma(r_w) = \gamma_s/\kappa_d(r_w). \tag{4.6}$$

In the following, we will call the wall potential-dependent term κ_d, the local correction factor for diffusion. From Eq. 4.6, Equation 4.4 can be rearranged to

$$m\frac{\partial v_i}{\partial t} = -k_{\mathrm{B}}T\frac{\partial \ln C}{\partial x_i} - \gamma_s/\kappa_d\,(v_i - U_i) - \sum_{j=1}^{M_k}\frac{\partial \varphi_w(r_w^j)}{\partial x_i}, \tag{4.7}$$

In the present method it is assumed that the solute moelcules do not generate microflows due to their interactions with the solvent. This can be taken into account by introducing a further correction factor to the drift term (affecting the bulk flow velocity U_i). This factor is called the lag coefficient κ_c and is assumed to be dependent only on the hydrodynamic radius r_s and the wall-distance r_w (wall potential-dependent).[67,71] κ_c is defined as the ratio of the perturbed flow velocity to the unperturbed flow velocity evaluated at the particle center. From Eq. 4.1 and adding the drift correction κ_c, Equation 4.7 rearranges to

$$\frac{m\kappa_dD_\infty}{k_BT}\frac{\partial v_i}{\partial t} = -\kappa_d\frac{D_\infty}{C}\frac{\partial C}{\partial x_i} - v_i + \kappa_cU_i - \frac{\kappa_dD_\infty}{k_BT}\sum_{j=1}^{M_k}\frac{\partial \varphi_w(r_w^j)}{\partial x_i}. \tag{4.8}$$

We now group the individual wall potentials into an integral wall potential $\mathit{\Phi}_w$ affecting the k-th particle as follows

$$\mathit{\Phi}_w = \sum_{j=1}^{M_k}\varphi_w(r_w^j). \tag{4.9}$$

Averaging Procedure By averaging over the particle ensemble, it yields

---

[67] W. M. Deen. *AIChE Journal*, **33**: 1409–1425, 1987.

$$\frac{mD_\infty}{k_B T}\langle\kappa_d\frac{\partial v_i}{\partial t}\rangle = -\frac{D_\infty}{\langle C\rangle}\langle\kappa_d\frac{\partial C}{\partial x_i}\rangle - \langle v_i\rangle + \langle\kappa_c U_i\rangle - \frac{D_\infty}{k_B T}\langle\kappa_d\frac{\partial \Phi_w}{\partial x_i}\rangle. \tag{4.10}$$

An instantaneous quantity of a given molecule (e.g. its velocity) can be averaged over a particle ensemble at a given instant, or equivalently, over a long time observing the same particle.[66,67] Building on this, we can consider an averaging of instantaneous quantities, ψ and ξ, whereby these are decomposed into time-averaged and fluctuating components (a concept first introduced by Reynolds, 1985[89] in the continuum mechanics).

$$\psi(t,x_i) = \langle\psi\rangle + \psi', \tag{4.11}$$

$$\langle\xi(t,x_i)\psi(t,x_i)\rangle = \langle\xi\rangle\langle\psi\rangle + \langle\xi'\psi'\rangle. \tag{4.12}$$

As the location and chemical nature of the wall atoms do not change in time, the force fields induced by their potentials are time-independent, meaning that the fluctuation components of κ_d and κ_c fall to zero. Taking into account these considerations, with average hindrance factors $K_d = \langle\kappa_d\rangle$ and $K_c = \langle\kappa_c\rangle$, Equation 4.10 can be written as

$$\frac{K_d D_\infty m}{k_B T}\frac{\partial\langle v_i\rangle}{\partial t} = -K_d\frac{D_\infty}{\langle C\rangle}\frac{\partial\langle C\rangle}{\partial x_i} - \langle v_i\rangle + K_c\langle U_i\rangle + \langle\Delta e\rangle, \tag{4.13}$$

with average correction term

$$\langle\Delta e\rangle = -\frac{K_d D_\infty}{k_B T}\frac{\partial\langle\Phi_w\rangle}{\partial x_i}. \tag{4.14}$$

We introduce this correction term as an error source of the method, since in the simulations we are not directly computing the wall-solute interactions. Instead, their enhancing effect on the drag coefficient (i.e. their hindering effect on the diffusivity) is modeled using a probabilistic approach, which is presented in Section 4.4.1. There, we will focus on deriving a function for the diffusive hindrance factor K_d.

It is worth noting that the correction term $\langle\Delta e\rangle$ is proportional to the sum of all vectors of the force field induced by the wall potential $\langle\Phi_w\rangle$, implying that for symmetric systems this term falls to zero under the assumption of an isotropic solid phase. This is the case, for example, when diffusion takes place within a cylindrical pore or around a spherical obstacle. Furthermore, it should be noticed that by omitting the direct computation of the wall potential, the information about the distribution of the solute particles with respect to the wall is now average.

---

[66] L. BOLTZMANN. *Vorlesungen über Gastheorie (translated into English as "Lectures on Gas Theory".)* Vorlesungen über Gastheorie J. A. Barth, 1898.

[89] O. REYNOLDS. *Phil. Trans. A Math. Phys. Eng. Sci.*, **186**: 123–164, 1895.

Stochastic Equation of Motion: Brownian Dynamics

This section briefly explains how the deterministic equation of motion derived above is transformed into a stochastic approach as shown by Langevin, 1908.[90]

When a particle ensemble subject to Brownian motion spreads within an unbounded medium, there is no preferred direction for the random movements of the particles (isotropic motion). Consequently, the particles will end up homogeneously distributed over the space after a certain period of time, compensating for all concentration gradients initially present. The macroscopic manifestation of this microscopic phenomenon can be used to reproduce diffusion.[90] Diffusive mass transport was modeled in the previous section using the negative gradient of the chemical potential. In the following, we will replace this deterministic term with a stochastic one $\sqrt{2\kappa_d D_\infty}\, W_i(t)$ containing Gaussian white noise $W_i(t)$. The integral of white noise is used to describe Brownian motion. Numerically, this is realized by generating a normally distributed random number for each Cartesian coordinate with zero mean $\mu = 0$ and variance $s^2 = 1$.[24,25] Thus, from Eq. 4.8, it follows

$$\frac{m\kappa_d D_\infty}{k_B T}\frac{\partial v_i}{\partial t} = \sqrt{2\kappa_d D_\infty}\, W_i(t) - v_i + \kappa_c U_i - \frac{\kappa_d D_\infty}{k_B T}\sum_{j=1}^{M_k}\frac{\partial \varphi_w(r_w^j)}{\partial x_i}. \tag{4.15}$$

Effective Mass Transport of a Particle Ensemble As the force field induced by the wall is not directly solved, the local gradients of concentration and the local values of the drag coefficient in the radial direction of a pore are spatially not resolved. Therefore, only the average forms of κ_d and κ_c, the diffusive and convective hindrance factors K_d and K_c, respectively, are physically meaningful for the equation of motion describing the effective mass transport of a particle ensemble trough a porous medium. Furthermore, inertial effects are neglected assuming that the average behavior of a solute molecule over time and the average over the particle ensemble are equivalent, in accordance with the ergodic hypothesis.[66,67] This inertia-free behavior can also be explained by the time scales considered, which are assumed to be longer than the characteristic relaxation time of a Brownian particle.[23,65] Thus, from Eq. 4.15, the following simplified equation of motion for the k-th diffusing particle is obtained

$$0 = \sqrt{2K_d D_\infty}\, W_i(t) - v_i + K_c U_i. \tag{4.16}$$

---

[90] DON S. LEMONS & ANTHONY GYTHIEL. *Am. J. Phys.*, **65**: 1079–1081, 1997.

[24] H G SCHUSTER & WOLFAM JUST. *Deterministic Chaos*. Wiley, 1994.

[25] GIORGIO VOLPE & GIOVANNI VOLPE. *Am. J. Phys.*, **81**: 224–230, 2013.

[23] HECTOR RUSINQUE et al. *J. Aerosol Sci.*, **129**: 28–39, 2018.

[65] XIN BIAN et al. *Soft Matter*, **12**: 6331–6346, 2016.

This Lagrangian approach allows us, for example, to obtain the effective diffusivity of the medium by computing the mean square displacement $\langle \Delta x_i^2(t) \rangle$ of the particle ensemble and its time derivative

$$\langle \Delta x_i^2(t) \rangle = \frac{1}{N} \sum_{i=1}^{N} (x_i(t) - \langle x_i(t) \rangle)^2, \tag{4.17}$$

$$D_{\text{eff},i} = \frac{1}{2} \frac{d}{dt} \langle \Delta x_i^2(t) \rangle. \tag{4.18}$$

Wall Hindrance Model: A Probabilistic Approach

When modeling mass transport in a porous medium without spatially resolving the pores, the solid fraction $(1 - \varepsilon)$ can be thought of as a hindrance (the probability that diffusion does not occur), while the void fraction ε is the probability of diffusion taking place and can be introduced as a correction factor.[80] Another example is the obstruction factor K_τ, or its reciprocal, the tortuosity. Here, the sum of the obstruction factor, considered as probability, with its complementary probability $(1 - K_\tau)$ corresponds to all possible roads or paths that a random walker can take to travel from point A to point B in free space. By placing obstacles between the two points, a fraction of these paths is blocked. Consequently, diffusion cannot take place along these paths. The obstruction factor K_τ indicates the fraction of free paths left. Thus, diffusion will only take place when at a given location the events of finding void space ε and a free path K_τ occur simultaneously. In other words, the probability of diffusion taking place is given by the product of the probabilities ε and K_τ, so that the total correction factor to diffusion is equal to $K_{\text{total}} = \varepsilon K_\tau$,[80] if no further hindrance to diffusion is to be considered.

In general, a given hindrance to diffusion $P_{A,1}$ and its associated correction factor $P_{A,2}$ can be viewed as complementary probabilities or events, so that $P_{A,1} + P_{A,2} = 1$. If a further hindrance to diffusion $P_{B,1}$ occurs simultaneously to $P_{A,1}$, the probability of diffusion taking place is given by the product of the probabilities $(1 - P_{A,1})(1 - P_{B,1})$. Building on this consideration, the fundamental idea behind the wall hindrance model is that there may be a hindrance probability to diffusion f_j induced by a wall atom (j) at a location x_i (location-dependent), so that its complementary probability, the correction factor, is equal to

$$\kappa_j = 1 - f_j. \tag{4.19}$$

Furthermore, the probability of diffusion taking place at the same location x_i when being hindered by the wall atoms A, B and C, simultaneously, is equal to the product of the probabilities given by

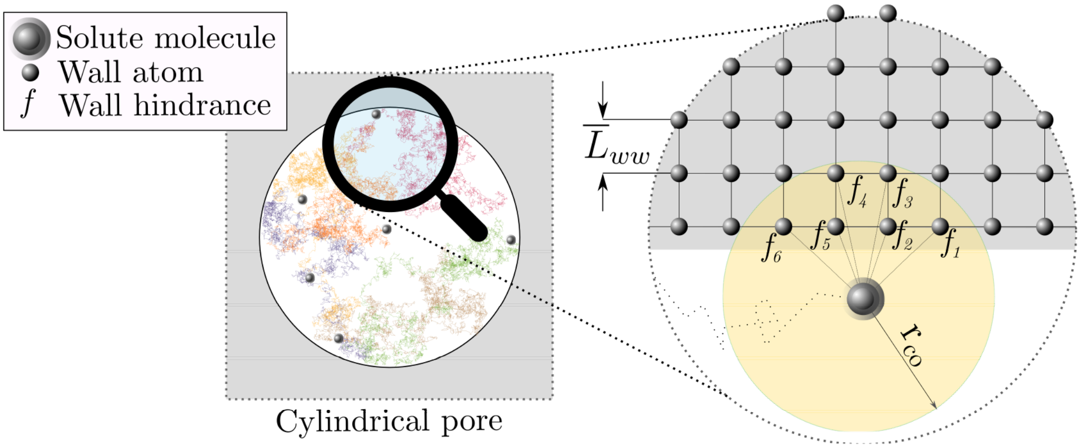

Figure 4.1: Discretization of the pore walls at the atomic level to calculate the interactions between wall atoms and solute molecules, where r_{co} is the cutoff radius above which the interactions are neglected and $\overline{L}_{ww}$ represents the average bond length between a pair of wall atoms. The chaotic lines within the cylindrical pore represent computed trajectories (random walks) of selected particles.

$$\kappa_d = (1 - f_A)(1 - f_B)(1 - f_C). \tag{4.20}$$

This results in the following equation for the diffusive hindrance factor of the particle ensemble

$$K_d = \frac{1}{N}\sum_{k=1}^{N}\kappa_d^k = \frac{1}{N}\sum_{k=1}^{N}\prod_{j=1}^{M_k}(1 - f_j^k) = \frac{1}{N}\sum_{k=1}^{N}\prod_{j=1}^{M_k}\kappa_j^k. \tag{4.21}$$

Numerically, this means that the random walkers have to gather all the information about their surroundings (all the f_j - see Figure 4.1), in order to compute the integral hindrance factor for diffusion, before they can move.

Now, we want to find a function for the hindrance probability $f_j(x_i)$. Let us assume that $f_j(x_i)$ at a given location x_i correlates directly with the magnitude of the force induced by the j-th wall atom at the same location, $\|F_j(x_i)\|$. It is further assumed that the wall atoms are significantly smaller than the solute molecules, so that the radius of the solute molecules r_m coincides with the collision diameter σ_{sw}, (i.e. $\sigma_{sw} \approx \sigma_{ss}/2$). This means that the force $\|F_j(x_i)\|$ is actually the reaction to the force exerted by the solute molecule on the wall atom, explained by Newton's third law of motion. Further, we add the constraint that the maximal value that $f_j(x_i)$ can take is one $f_j(x_i) \leq 1$ given by the axiom of the probability space. We could also add the constraint of the probability $f_j(x_i)$ being always equal or bigger than zero given by the same axiom. However, this is a fact, that has been questioned by different authors such as Paul Dirac, 1942[91] and Burgin, 2009.[92] A function that satisfies these requirements may be the normalization of the force acting on the solute molecule as follows

$$f(x_i) = \frac{\|F_j(x_i)\|}{\max\{\|F_j(x_i)\|\}} \quad \text{for} \quad r_w(x_i) \geq 2^{(1/6)}\sigma_{sw}. \tag{4.22}$$

Where $2^{(1/6)}\sigma_{sw}$ is the distance at which the Lennard-Jones potential shows its minimum (i.e. where the force becomes zero). Beneath this value the repulsion force increases dramatically, as the collision between the particles is imminent. Here, the collision is modeled by implementing a bounce-back boundary condition (BC), in this case, diffuse reflection of the incoming particles from the pore wall.

$$f(x_i) = 0; \text{ BC: Diffuse reflextion for } r_w(x_i) < 2^{(1/6)}\sigma_{sw}. \tag{4.23}$$

As already mentioned, under the assumption of van der Waals interactions between wall atoms and solute molecules, the force $F(r_w(x_i))$ can be modeled using the Lennard-Jones potential (Eq. 4.3), with wall distance

$$r_w(x_i) = \|x_i - x_{w,i}\| = \sqrt{(x_1 - x_{w,1})^2 + (x_2 - x_{w,2})^2 + (x_3 - x_{w,3})^2},$$

where $x_{w,i}$ is the location of a given wall atom (a *constant*). So, $\varphi_w(r_w)$ is derived

$$F_i(r_w) = -\frac{\partial \varphi_w(r_w)}{\partial x_i} = 4\epsilon_{sw}\left(12\,\frac{{\sigma_{sw}}^{12}}{{r_w}^{13}} - 6\,\frac{{\sigma_{sw}}^{6}}{{r_w}^{7}}\right) e_i. \tag{4.24}$$

The hindrance probability, a dimensionless normalized force f is obtained by dividing the force by its maximum as plotted in Figure 4.2

$$f(r_w) = \frac{2\left(\frac{\sigma_{sw}}{r_w}\right)^{13} - \left(\frac{\sigma_{sw}}{r_w}\right)^{7}}{2\left(\frac{7}{26}\right)^{13/6} - \left(\frac{7}{26}\right)^{7/6}} \quad \text{for} \quad r_w(x_i) \geq 2^{(1/6)}\sigma_{sw}. \tag{4.25}$$

---

[91] P. A. M. Dirac. *P. Roy. Soc. A. Math. Phy. A*, **180**: 1–40, 1942.

[92] Mark Burgin. *Extended probabilities: mathematical foundations.* arXiv, 2009.

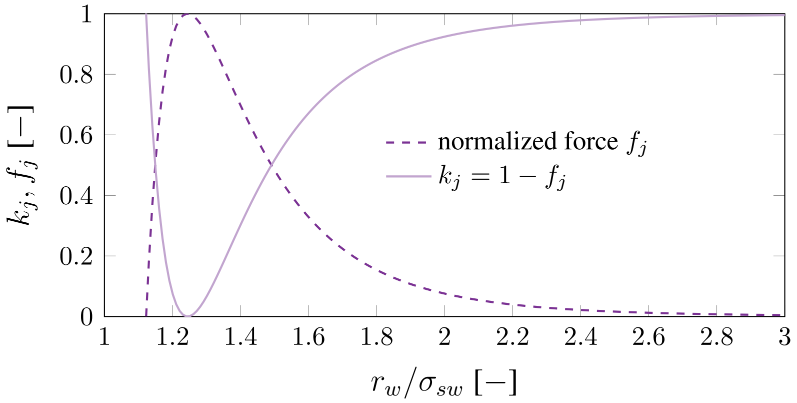

Figure 4.2: Local hindrance probability f_j and its complementary probability k_j as a function of the dimensionless distance between diffusing particle and wall atom.

Validation To validate the wall hindrance model a set of simulations was carried out considering the motion of a particle ensemble $N = 10^6$ in straight cylindrical pores, for different pore and molecule sizes, $7 \leq x/\overline{L}_{ww} \leq 403$ and $1.5 \leq \sigma_{sw}/\overline{L}_{ww} \leq 6$, respectively (see definition of $\overline{L}_{ww}$ in Fig. 4.1) as well as correction factor for convection equals one, $K_c = 1$. Notice, as already mentioned, that due to the inherent symmetry of the system (the cylindrical pores), the correction term $\langle \Delta e \rangle$ (see Eq. 4.14) drops to zero. As can be seen in Figure 4.3, the validation results show good agreement with the experimental data from the literature.

In order to solve the function for K_d derived above, the equation of motion (Eq. 4.16) is numerically integrated by applying the leapfrog method .[68]

The leapfrog integration is a second-order method. Though, it requires the same number of function evaluations per step as the first order Euler scheme. Furthermore, the leapfrog method is more stable for oscillatory motion in contrast to Euler integration[68].

In molecular dynamics, the Lennard-Jones potential is usually truncated at cutoff radii r_{co} between $[2.2 - 3]\sigma_{sw}$, mostly at $r_{co} = 2.5\sigma_{sw}$.[93–96] Here a cutoff radius of $r_{co} = 3\sigma_{sw}$ was used for the simulations. The effect of using a shorter cutoff radius was examined. As shown by the simulation results plotted in Fig. 4.4b, truncating the Lennard-Jones potential at a too short cutoff radius can have significant effects on the results obtained.

---

[68] Guihua Zhang & Tamar Schlick. *Mol. Phys.*, **84**: 1077–1098, 1995.
[93] Ethan A. Mastny et al. *J. Chem. Phys.*, **127**: 094106, 2007.
[94] Stefan Becker et al. *Langmuir*, **30**: 13606–13614, 2014.
[95] Michaela Heier et al. *Mol. Phys.*, **116**: 2083–2094, 2018.
[96] Jadran Vrabec et al. *Mol. Phys.*, **104**: 1509–1527, 2006.

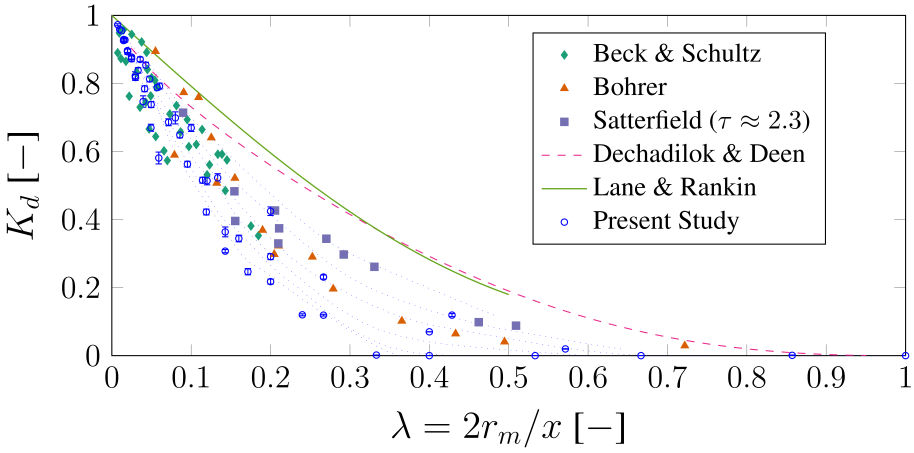

Figure 4.3: Diffusive hindrance factor K_d in straight cylindrical pores versus the reduced molecular diameter λ. The molecular diameter $2r_m$is given by $2r_m = 2\sigma_{sw}$.

The error bars in Figures 4.3 and 4.4 arise from the stochastic nature of the diffusion modeling and represent the standard deviation of various simulation runs (at least 3 runs for each point with 10^6 tracer molecules). Due to the short-range interactions, our simulation results as well as the experimental results from literature are more scattered than the numerical results for hard spheres from other authors. The dotted lines represent each molecule size σ_{sw} considered, whereby, due to their weaker and shorter interactions, the smallest molecules exhibit the weakest hindrance to diffusion and are therefore closest to the curves for hard spheres given by the equations of Dechadilok & Deen and Lane & Rankin.

K_d Approximation from the PSD for a Complex Geometry

A complex porous structure can be thought of as a network of cylindrical pores, if the shape of the individual pores is approximately cylindrical.[97,98] Let the pore size distribution (referred to the pore volume) of such a porous configuration be $q_3(x)$ with units $[\mathrm{m}^3/\mathrm{m}^4]$, fulfilling

$$\int_{x_{min}}^{x_{max}} q_3(x)dx = 1. \tag{4.26}$$

For this case, we can estimate the diffusive hindrance factor of the porous structure as the sum of the hindrances caused by each cylinder forming the network of pores, when the average bond length between wall atoms $\overline{L}_{ww}$ and the molecule radius r_m are known

$$K_\mathrm{d} = \int_{x_{min}}^{x_{max}} K_{d,\mathrm{cyl}}(x) q_3(x)dx, \tag{4.27}$$

---

[97] A.B. Abell et al. *J. Colloid Interf. Sci.*, **211**: 39–44, 1999.
[98] W. C. Conner et al. *Langmuir*, **2**: 151–154, 1986.

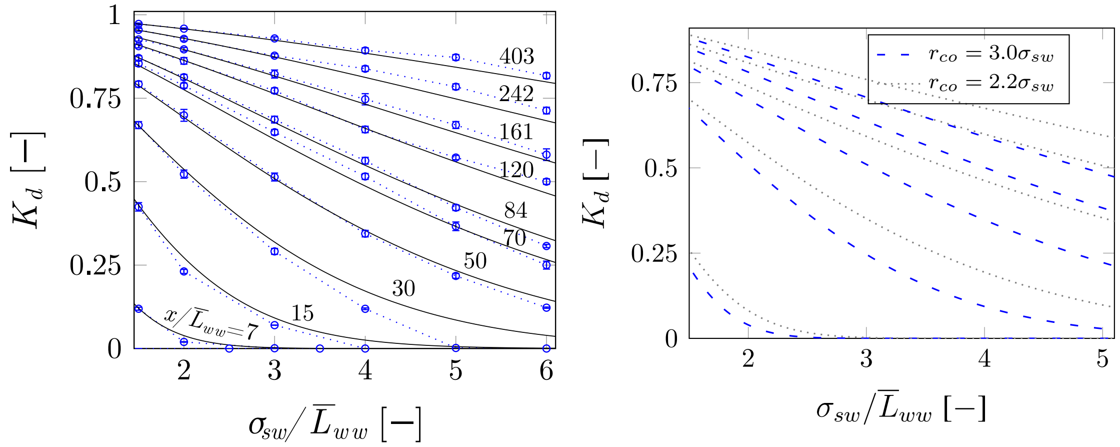

(a) K_d for cylindrical pores

(b) Effect of the cutoff radius

Figure 4.4: a) Diffusive hindrance factor $K_{d,\text{cyl}}$ as a function of the ratios of the distance σ_{sw} and the pore size x to the mean bond length $\overline{L}_{ww}$, in straight cylindrical pores (circles) with curves fitting the results (solid lines). b) $K_{d,\text{cyl}}$ for cutoff radii $r_{co}/\sigma_{sw} = 2.2$ and $r_{co}/\sigma_{sw} = 3.0$.

with the diffusive hindrance factor $K_{d,\text{cyl}}$ for straight cylindrical pores.

A function fitting the results obtained for the straight cylindrical pores is presented

$$K_{d,\text{cyl}} = \exp\left\{\frac{-(\sigma_{sw}/\overline{L}_{ww})^{3/2}}{0.162351(x/\overline{L}_{ww}) - 0.266835}\right\} \tag{4.28}$$

with

$$0 \leq K_{d,\text{cyl}} \leq 1,$$

derived within the following intervals of σ_{sw} and $\overline{L}_{ww}$

$$7 \leq x/\overline{L}_{ww} \leq 403,$$

$$1.5 \leq \sigma_{sw}/\overline{L}_{ww} \leq 6.$$

In order to evaluate the performance of the fitting function (Eq. 4.28) within the range considered, Figure 4.4a is presented, where good concordance between fitting curves and simulation results can be seen.

The pore size distribution of a porous material $q_3(x)$ can be experimentally obtained, e.g. via mercury or nitrogen porosimetry, using a model for cylindrical pores,[97,98] so that the hindrance to diffusion of a given molecule diffusing within a real porous medium can be estimated from experimental data. For these purpose, the molecular radius r_m and the average bond length of the solid phase $\overline{L}_{ww}$ must be known as well as the pore size distribution, which has to be properly normalized in order to fulfill Eq. 4.26.

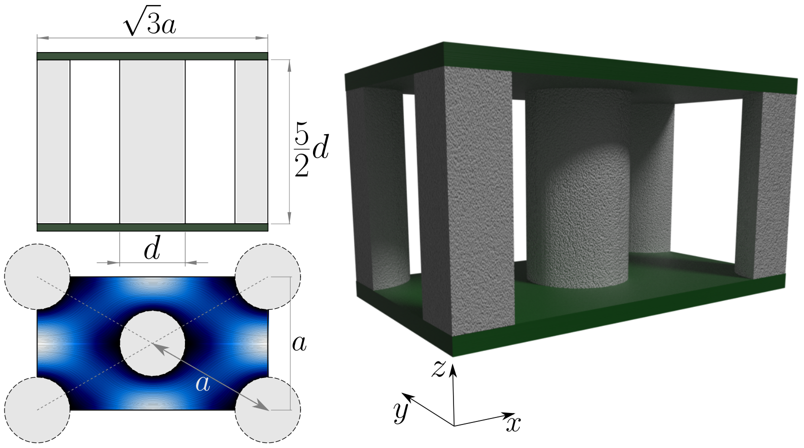

Figure 4.5: Staggered cylinder arrangement confined in a narrow slit. The bulk flow occurs as a consequence of a force or pressure gradient acting in the positive x-axis direction. The velocity field is graphically represented in the lower left corner.

Passive Scalar Case: Random Walk Particle Tracking

If we consider passive scalars with negligible inertial effects and radii zero, which results in negligible wall potential, the diffusive and convective hindrance factors K_d and K_c, respectively, take the value 1. This leads to the equation of motion used in the Random Walk Particle Tracking method (RWPT).[99] From Equation 4.16, it follows

$$v_i = \sqrt{2D_\infty}\, W_i(t) + U_i. \tag{4.29}$$

This model can be used to indirectly solve the Convection-Diffusion equation or to compute the diffusivity needed in this Eulerian continuum approach.[80]

In order to verify the implementation of the RWPT method, the dispersion of a particle ensemble $N = 10^6$ within a staggered cylinder arrangement confined in a narrow slit is simulated (see Fig. 4.5). The obtained results plotted in Fig. 4.6a are compared with the numerical results of Khirevich[100] and the experimental data from Eghbali et al.[101] These show a good agreement with the results of Khirevich, as expected since the RWPT method was also applied in his simulations. The longitudinal diffusivity for the case of Taylor dispersion is also simulated and the results are compared with the analytical solution for the Taylor-Aris dispersion, which can be derived from the Convection-Diffusion equation.[62] for the case of shear flow in an open channel or in a pipe (see Fig. 4.6b).

The discrepancy with the experimental values of Eghbali et al. may be explained by the shape of the solute molecule studied, namely Coumarin 480 ($C_{16}H_{17}NO_2$). This molecule

---

[99] Siarhei Khirevich et al. *Commun. Comput. Phys.*, **13**: 801–822, 2013.

[100] Siarhei Khirevich. *PhD Thesis*, 159, 2011.

[101] Hamed Eghbali et al. *Anal. Chem.*, **81**: 705–715, 2009.

[62] R. Aris. *P. Roy. Soc. A. Math. Phy. A*, **235**: 67–77, 1956.

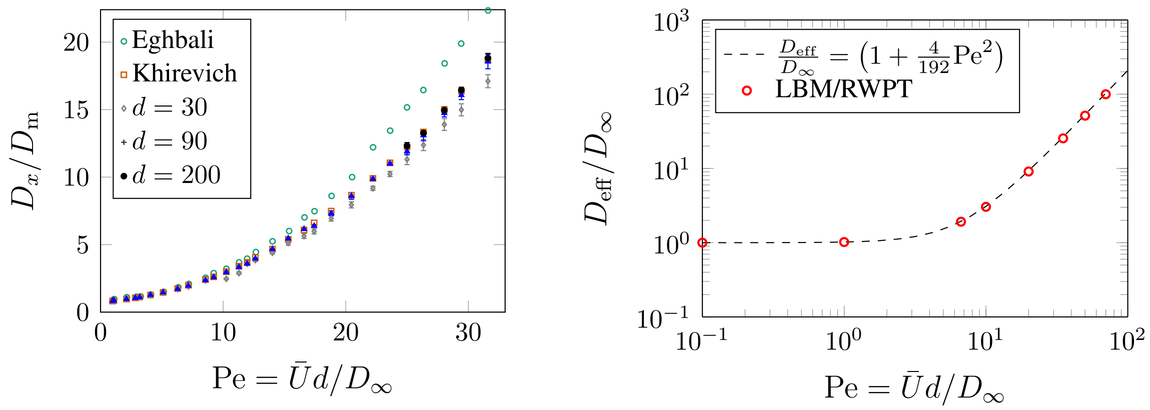

(a) Dispersion in arrays

(b) Taylor dispersion

Figure 4.6: a) Longitudinal diffusivity in a staggered cylinder arrangement as a function of the Péclet number. The effect of the resolution of the lattice used for the discretization of the geometry is also graphically represented. The resolution used in the simulations of Khirevich was 200 grid nodes per cylinder diameter, $d = 200$. b) Taylor dispersion as a function of the Péclet number compared with its analytical solution.

contains four interconnected rings making its structure very flat and rigid, which differs strongly from the assumption of a pointwise passive molecule. Here, the necessity of a correction factor for convection $K_c > 1$ [71] regarding the shape of the molecule becomes evident, since the discrepancy increases with the Péclet number (the ratio of convection to diffusion $\mathrm{Pe} = \bar{U}d/D_\infty$).

4.4.2 Multiscale Numerical Approach

In this section, mass transport in packed beds is considered. These are arranged in a hierarchical pore system consisting of three pore-scales with diameters around $x \approx 100\,\mu\mathrm{m}$ for the largest scale, $x \approx 300\,\mathrm{nm}$ for the medium scale and $x \approx 10\,\mathrm{nm}$ for the smallest scale, as shown in Figure 4.7. Hierarchical pore structures can be used in catalytic applications, where mass transport controls the macrokinetics of the heterogeneous catalytic process, in order to enhance mass transport.[9–11]

Macroscopic Approach

Under the continuum assumption, the transport in the microstructure of the porous medium can be calculated, using a numerical method able to spatially resolve the geometric structure of the medium. Due to the different length scales, this is de facto not possible, which is why a modeling of the mass transport at the macroscopic level has to be carried out on

---

[9] Robert Güttel & Thomas Turek. *Energy Technol.*, **4**: 44–54, 2016.
[10] Li Chen et al. *Chem. Eng. J.*, **349**: 428–437, 2018.
[11] Jian Yin et al. *J. Mater. Chem. A*, **6**: 8441–8448, 2018.

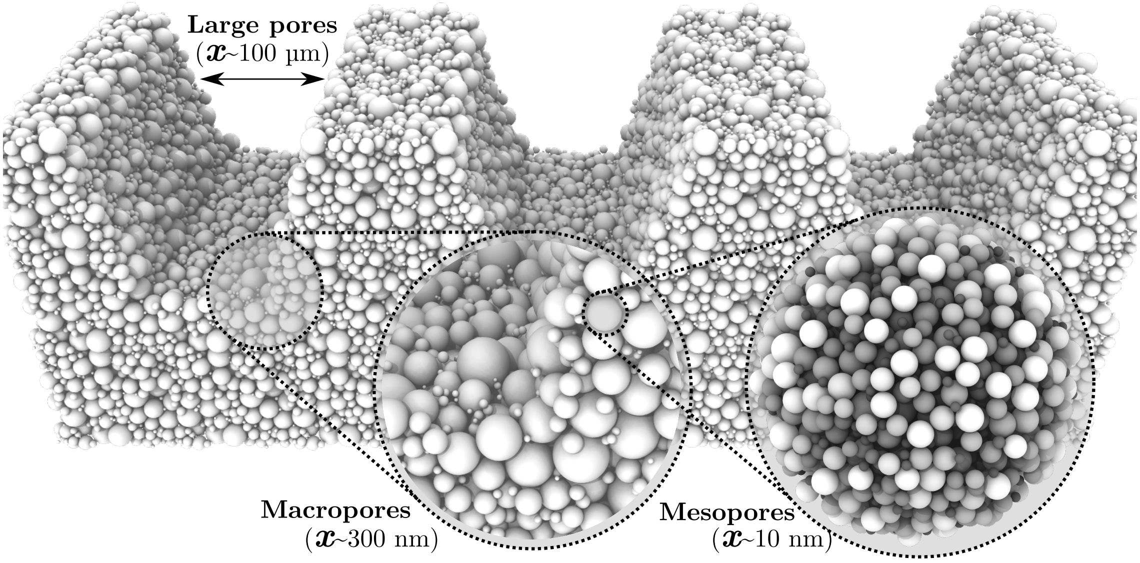

Figure 4.7: Hierarchic-nanoporous structure used as a medium in the application example. Porescales according to the IUPAC definition for nanoporous materials.

the basis of average quantities and effective transport coefficients. Thus, only the large pores are spatially resolved in such simulation step. Using local volume averaging, the convection-diffusion equation is obtained[102,103]

$$\frac{\partial \bar{C}}{\partial t} + \bar{U}_i \frac{\partial \bar{C}}{\partial x_i} = D_{\text{eff,MP}} \frac{\partial^2 \bar{C}}{\partial x_i^2} + \bar{R}, \tag{4.30}$$

where $\bar{C}$ is the average particle concentration, $D_{\text{eff,MP}}$ the effective diffusivity of the macroporous and mesoporous structure, which can assume the general form of a second-order tensor for anisotropic pore structures, $\bar{U}_i$ the average velocity field, which describes convection, and $\bar{R}$ a source term modeling e.g. chemical reactions.

In this paper, the focus is on the modeling of micro- and nanoscales (the microscopic approach). Within the scope of the research project to which this study is related, the modeling of the macroscale has already been pursued by Bufe et al.[80]

Microscopic Approach

Nanoscale Simulation Step The calculation of the diffusivity of the mesoporous structure $D_{\text{eff},m\text{P}}$ is the first simulation step. This effective diffusivity is given by the following expression

$$D_{\text{eff},m\text{P}} = K_d K_\tau D_\infty, \tag{4.31}$$

and is required as input for the next simulation step at the microscale.
Here, the nanoscale is directly simulated using the wall hindrance model presented in Sec-

---

[102] M. Sahimi. *Flow and Transport in Porous Media and Fractured Rock: From Classical Methods to Modern Approaches*. Wiley, 2011.

[103] Donald L. Koch & John F. Brady. *J. Fluid Mech.*, **154**: 399–427, 1985.

tion 4.4.1. The equation of motion Eq. 4.16 with the equation for the diffusive hindrance factor (Eq. 4.21) have to be solved. Furthermore, the effective diffusivity of the mesoporous structure is computed with the time derivative of the mean square displacement, Eq. 4.17 and 4.18.

Microscale Simulation Step The (nano-scaled) mesopores are not spatially resolved in the microscale modelling. Instead, the porous structures at the nanoscale are treated as an effective medium (see Figure 4.8).

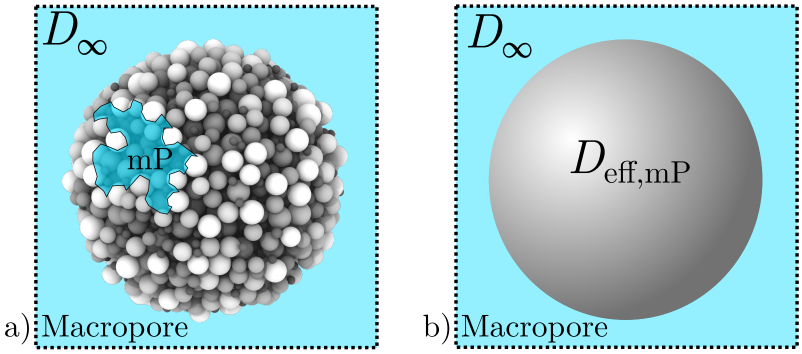

Figure 4.8: a) Macropores (MP) and mesopores (mP) of the microscale. b) Effective representation of the mesoporous medium.

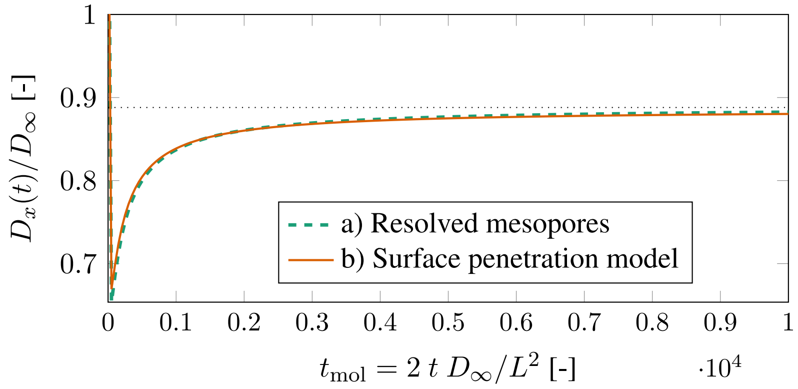

Figure 4.9: Time evolution of the diffusivity of a simple cubic arrangement of spheres for the cases of spatially resolved and non-resolved mesopores (see Fig. 8). The parameters considered are $K_d = 1$, $K_\tau = D_{\text{eff,mP}}/D_\infty = 0.729$, $\varepsilon_{m\text{P}} = 0.454$, and $\varepsilon_{\text{MP}} = 1$.

The RWPT method presented in Section 4.4.1 is used to describe the mass transport at the microscale. The bridge between the macro- and mesoporous media is established by a probabilistic penetration model. Here, the probability of a scalar tracer entering the mesopores from the outer void space P_{in} and the probability of a tracer leaving the mesopores P_{out} can be obtained using the following relations under the assumption of an isotropic mesoporous medium[104,105]

$$P_{\text{in}} = \frac{\varepsilon_{m\text{P}}}{\varepsilon_{\text{MP}}}\sqrt{\frac{D_{m\text{P}}}{D_{\text{MP}}}} = \sqrt{K_d}\frac{\varepsilon_{m\text{P}}}{\varepsilon_{\text{MP}}} \quad \text{and} \quad P_{\text{out}} = 1. \tag{4.32}$$

Where $D_{m\text{P}} = K_d D_\infty$ and $D_{\text{MP}} = D_\infty$ are the integral diffusion coefficients within a representative meso- and macropore, respectively.

Once a tracer particle enters the mesopores, it changes its diffusive motion according to the effective diffusivity of the mesoporous structure $D_{\text{eff},m\text{P}}$ given by Eq. 4.31. The effective diffusivity of the combined system of macro- and mesopores $D_{\text{eff,MP}}$ is computed from the time derivative of the mean square displacement (see Eq. 4.17 and 4.18).

In order to verify the implementation of the probabilistic penetration model, the diffusivity of a simple cubic arrangement of spheres for the cases of spatially resolved and non-resolved mesopores is numerically simulated (see Figure 4.8) as a function of a dimensionless time t_{mol} until the asymptotic behavior is reached. As can be seen from the results, shown in Figure 4.9, the implementation was successfully verified.

Application Example

In this section, the mass transport of a particle ensemble $N = 10^6$ in a hierarchical pore system like the one shown in Figure 4.7 using the microscopic approach proposed above.

Nanoscale Simulation Step At the nanoscale, two polydisperse nanosphere packings were computer generated using the software tool provided by Baranau and Tallarek (2014).[36] In practice, the spheres of the packings are nanoparticles, which stick to each other due to attractive interactions and friction to form a mesoporous structure.[106] Two sphere packings are generated from two particle collectives showing the same size distribution. These structures are called Building-Blocks and are represented graphically in Figure 4.8a. The particle size distribution follows a normal distribution, $x_p = \mathcal{N}(\bar{x}_p, s^2)$ with $\bar{x}_p = 23.82\,\text{nm}$ and $s = 4.275\,\text{nm}$. Due to the random initial positions of the spheres in the generation algorithm, and the random (normal-distributed) particle sizes, the generated packings slightly differ in their resulting void fractions and obstruction factors with $\varepsilon_{\text{BB1}} = 0.45$, $\varepsilon_{\text{BB2}} = 0.47$ and $K_{\tau,\text{BB1}} = 0.735$, $K_{\tau,\text{BB2}} = 0.749$. Via a sphere insertion method (i.e. the void space of the generated sphere packing is randomly filled with spheres in order to characterize the void space itself), a pore size distribution (PSD) for

---

[104] Anton Daneyko et al. *J. Chromatogr. A*, **1407**: 139–156, 2015.

[105] Jorge M. Ramirez et al. *Water Resour. Res.*, **44**: , 2008.

[36] Vasili Baranau & Ulrich Tallarek. *Soft Matter*, **10**: 3826–3841, 2014.

[106] Aurina Martínez Arias & Alfred P. Weber. *J. Aerosol Sci.*, **131**: 1–12, 2019.

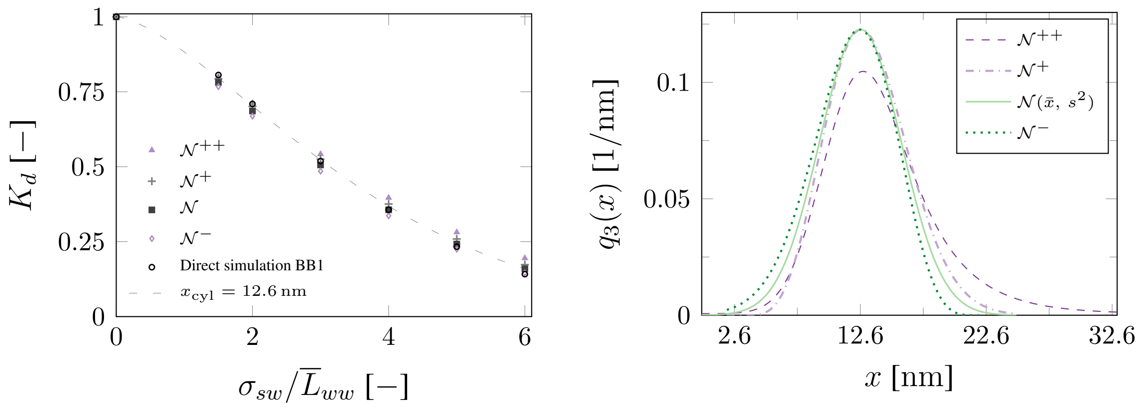

Figure 4.10: On the left, diffusive hindrance factor K_d in a computer-generated Building-Block BB1. Direct simulation and PSD approximations of K_d based on normal distributions $\mathcal{N}$ centered at $\bar{x} = x_{cyl}$ with different standard deviations. On the right, PSDs $q_3(x)$ considered. The distributions are slightly skewed to the left $\mathcal{N}^-$ and to the right $\mathcal{N}^+$, to a greater extent for $\mathcal{N}^{++}$, without changing $\bar{x}$.

the generated Building-Blocks (BB1 and BB2) can be estimated from the particle size of the filling spheres. The software provided by Baranau et al.[107] could also be used to this purpose.

Note, that the resulting pore size distributions are shape-dependent, meaning that they depend, for example, on the shape of the filling material or on the pore shape assumed by the evaluation model. Several evaluation models can be found in literature that are able to determine the PSD from an adsorption isotherm (experimentally obtained) for slits as well as for cylindrical and spherical pores.[108,109]

In this study, we are rather interested in estimating the pore size distribution of BB1 and BB2 for the case of cylindrical pores. The aim of the latter is to apply the K_d approximation from the PSD $q_3(x)$, as suggested in Section 4.4.1; since the pore size distribution of the generated Building-Blocks cannot be calculated using, for example, an isotherm as mentioned above, we will make some assumptions and evaluate their hypothetical outcome based on how well this matches the calculated diffusive hindrances. We assume that the pore size distribution is also normal-distributed, $q_3(x) \approx \mathcal{N}(\bar{x},\, s^2)$ centered at the cylindrical pore size x_{cyl} to which the results of the direct simulation fit best, $\bar{x} = x_{cyl}$. Further, we consider the impact of the standard deviation and of certain level of skewness in the normal distribution. Here we consider two cases for the variation of the standard deviation (s_1 and s_2), and three cases for the variation of the skewness of the distribution: the first with a distribution slightly skewed to the left, further noted as $\mathcal{N}^-$, and a second

---

[107] VASILI BARANAU et al. *Soft Matter*, **9**: 3361, 2013.
[108] LINDA S. CHENG & YANG RALPH T. *Chem. Eng. Sci.*, **49**: 2599–2609, 1994.
[109] SALIL U. REGE & RALPH T. YANG. *AIChE Journal*, **46**: 734–750, 2000.

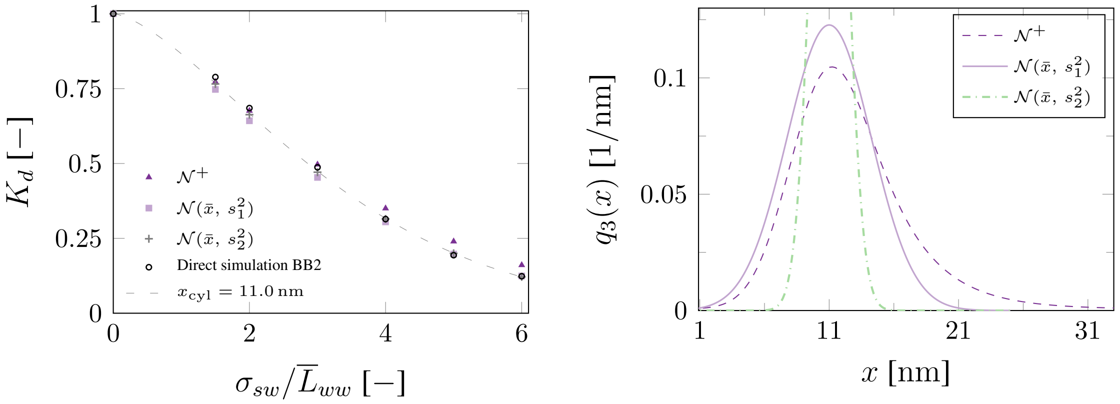

Figure 4.11: On the left, diffusive hindrance factor K_d in a computer-generated Building-Block BB2. Direct simulation and PSD approximations of K_d based on normal distributions $\mathcal{N}$ centered at $\bar{x} = x_{cyl}$ with different standard deviations. On the right, PSDs $q_3(x)$ considered. The distribution $\mathcal{N}^+$ is slightly skewed to the right without changing $\bar{x}$.

distribution slightly skewed to the right, $\mathcal{N}^+$, as well as a third one also skewed to the right but in a larger extent, $\mathcal{N}^{++}$. The average pore size $\bar{x}$ is kept constant in all the cases considered.

Bulk flow (convection) is not considered in this example. The results for the nanoscale simulation step are shown in Figures 4.10 and 4.11.

Microscale Simulation Step A computer generated, hierarchical-porous structure containing micro- and mesopores (a structure made of Building-Blocks) is considered, as shown in Figure 4.7. It is assumed that the macropores contribute 53 % and the mesopores 47 % to the total void space of this structure. From these values of the void space fractions a total porosity of 64 % can be determined for the generated layer of Building-Blocks.
As already mentioned, in the microscale simulation step only the contours or outer surfaces of the Building-Blocks and not their mesopores are spatially resolved. From the values of the effective diffusivity obtained in the previous simulation step, the simulations for the microscale are carried out and their results are shown in Figure 4.12.

Discussion With regard to the results obtained for the Building-Blocks BB1 and BB2 (Figures 4.10 and 4.11, respectively), it was found that the diffusive hindrance factor of BB1 comes closest to the calculated hindrance for a straight cylindrical pore of $12.6\,\mathrm{nm}$ diameter, whereas in the case of BB2 the nearest hindrance corresponds to that shown by a cylindrical pore size of $11.0\,\mathrm{nm}$. The assumed pore size distributions $\mathcal{N}(\bar{x},\, s^2)$ centered at these pore sizes show excellent agreement with the results of the direct simulations.

As far as the simulations of mass transport within the layers (made of Building-Blocks

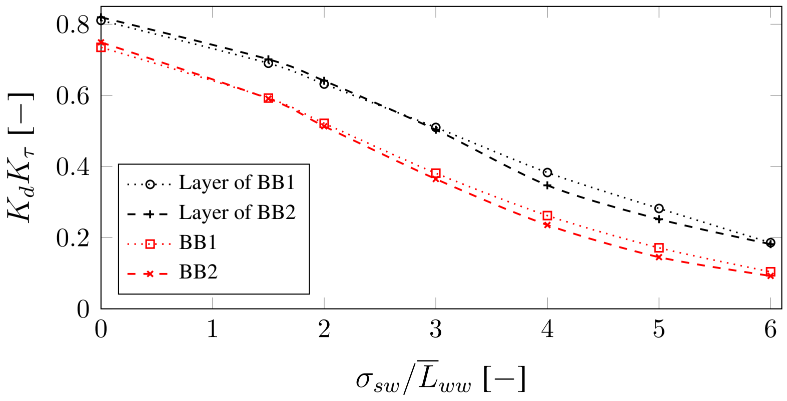

Figure 4.12: Total hindrance to diffusion, i.e. the obstrucion factor K_τ and diffusive hindrance factor K_d related to the layers made of the Building-Blocks BB1 and BB2.

BB1 and BB2) are concerned, it was found that there is a molecule size above which the hindrance for the layer consisting of BB2 is stronger, since the K_d curves intersect at some point between $2 < \sigma_{sw}/\overline{L}_{ww} < 3$ (see black curves in Figure 4.12). This can be explained by the fact that the dominant pore size of the Building-Blocks BB2 ($\bar{x} = 11.0\text{nm}$) is smaller than that of the BB1 ($\bar{x} = 12.6\text{nm}$) (the smaller the pore size, the stronger the hindrance), while the smaller obstruction factor of the layer made of BB1 constitutes a stronger hindrance to diffusion. This means, that for small molecule sizes the smaller obstruction factor of the BB1 layer controls the total hindrance to diffusion, while at large molecule sizes the stronger hindrance factor for diffusion of the BB2 layer controls it.

4.5 Conclusions

The hindrances to diffusion that an ensemble of solute molecules (spherical, large and "soft") experiences when passing through a narrow pore were modeled using an equation of motion from Brownian dynamics. The fundamental term of this equation is a local correction factor for diffusion, which accounts for the effect of the solute-wall interactions on the drag and diffusion coefficients. Here a mathematical model for the local correction factor is proposed using a probabilistic approach based on the Lennard-Jones potential for the case of van der Waals interactions between solute molecules and wall atoms where no physical adsorption takes place on the pore walls. Subsequently, the validation of the model is successfully carried out by means of experimental and numerical data from the literature. In addition, an approximation of the diffusive hindrance factor for complex geometries out of their pore size distribution is suggested. For that purpose, a function fitting the simulation results for the hindrance factor for diffusion in straight cylindrical pores is presented.

Finally, a multiscale approach using the models described above is proposed and illustrated with the help of an application example. For this matter, a hierarchic-nanoporous system is considered containing micro- and mesopores. Future work will focus on the introduction of additional interactions, e.g. associated to thermally activated processes such as chemical reactions or adsorption, and on further hindrances to diffusion.

Acknowledgment: The authors appreciate the support for this project by the North-German Supercomputing Alliance (HLRN) as well as by the Lower Saxony Ministry of Science and Culture within the PhD program "Self-organizing multifunctional structures for adaptive high performance light-weight constructions". The framework of this coordinated program is the "Campus for Functional Materials and Functional Structures" (https://www. campus-fws.de/de/) which is an institution of the Clausthal University of Technology (TUC) in collaboration with the Deutsches Zentrum für Luft- und Raumfahrt (DLR, German Aerospace Center) in Braunschweig and the Bundesanstalt für Materialforschung und -prüfung (BAM, Federal Institute for Material Testing) in Berlin, completed by the Technical University of Braunschweig (TU BS).

4.6 Notation

C	$1/\mathrm{m}^3$	particle concentration
D_∞	m^2/s	diffusivity in dilute bulk solution
$D_{\mathrm{eff,MP}}$	m^2/s	effective diffusivity in the macro- & mesoporous structure
$D_{\mathrm{eff,mP}}$	m^2/s	effective diffusivity in the mesoporous structure
D_{local}	m^2/s	local diffusivity in a mesopore
f, f_j	–	probability of diffusion being hindered when influenced by the j-th wall atom
i		vectorial index: $\varPsi_i = \{\varPsi_1, \varPsi_2, \varPsi_3\} = \{\varPsi_x, \varPsi_y, \varPsi_z\}$
j	–	j-th wall atom acting on the k-th diffusing particle
k	–	k-th diffusing particle of the ensemble
k_B	$\mathrm{J\,K}^{-1}$	Boltzmann constant
K_d	–	integral hindrance (correction) factor for diffusion
K_c	–	integral convective factor for convection
$\overline{L}_{ww}$	m	average bond length between a pair of wall atoms
M_k	–	number of wall atoms acting on the k-th diffusing particle
N	–	number of diffusing particles
$\mathcal{N}(\bar{x}, s^2)$		normal distribution centered in $\bar{x}$ with variance s^2
$q_3(x)$	$\mathrm{m}^3/\mathrm{m}^4$	pore size distribution (PSD)
r_{co}	m	cutoff radius
r_m	m	molecular radius
r_s	m	hydrodynamic Stokes' radius
s^2, s		variance & standard deviation, respectively
U_i	$\mathrm{m\,s}^{-1}$	flow velocity at the particle center
v_i	$\mathrm{m\,s}^{-1}$	particle velocity
$W_i(t)$	–	Gaussian white noise with $s^2 = 1$
x, x_p	m	pore size & particle size, respectively
ε	–	porosity (void space)
κ_d	–	local hindrance (correction) factor for diffusion
κ_c	–	lag coefficient
κ, κ_j	–	probability of diffusion taking place when influenced by the j-th wall atom
φ_w	J	potential of a wall atom
$\varPhi_w$	J	integral wall potential
γ	$\mathrm{kg\,s}^{-1}$	drag coefficient
γ_s	$\mathrm{kg\,s}^{-1}$	Stokes' drag coefficient
η	$\mathrm{kg\,m}^{-1}\,\mathrm{s}^{-1}$	viscosity
σ_{ss}	m	Lennard-Jones' collision diameter between solute and solute molecules
σ_{sw}	m	Lennard-Jones' collision diameter between solute and wall molecular entities

5 Effect of electric forces on the formation of nanoparticulate clusters

This chapter was built with the structure of a full paper to be submitted to a scientific journal

---

Hector Rusinque, Aurina Martinez-Arias, Juliana Rivas-Botero
Alfred Weber, Gunther Brenner (2019).
Formation of nanoparticulate spray-dried clusters: A numerical and experimental study.

5.1 Zussamenfassung

Die Verwendung von kolloidalen Siliziumdioxid-Nanopartikeln (NPs) ist vielfältig, z. B. in der Katalyse, Pharmazie und in Beschichtungen. Aufgrund der Neigung von Kolloiden zur Selbstassemblierung werden kolloidale Dispersionen normalerweise gegen Aggregation stabilisiert. Wenn der Selbstorganisationsprozess jedoch auf kontrollierte Weise durchgeführt werden kann, lässt sich die Aggregation ausnutzen, um nanopartikuläre Cluster mit einstellbaren Eigenschaften zu erhalten. Die katalytischen, optischen und elektronischen Eigenschaften eines Nanomaterials können durch seine GröSSe, Form und Struktur in einem MaSSe beeinflusst werden, das nicht leicht vorhersagbar ist. Die Bewältigung dieser Herausforderungen wird durch Strategien zur Synthese von mesoporösen Aggregaten mit einstellbarer PorengröSSe ermöglicht.[110]

Im vorliegenden Kapitel wird eine Sprühtrocknungstechnik verwendet, um mesoporöse nanopartikuläre Cluster zu synthetisieren.[106] Dies ist eine gut etablierte Synthesestrategie, bei der eine kolloidale Dispersion von Siliziumdioxid-NPs in Tröpfchen von wenigen Mikrometern zerstäubt wird, die anschlieSSend einen Trocknungsprozess durchlaufen. Während das Tröpfchen schrumpft, lagern sich die NPs zu einem kugelförmigen Cluster mit mesoporöser Struktur zusammen, der auch als Building Block (BB) bezeichnet wird. Durch Zugabe eines Metalls zur Dispersion, z. B. in Form eines Metallnitrats, können Silica-Cluster synthetisiert werden, die metallische NPs tragen. In einem anschlieSSenden Schritt können die hergestellten BBs aufgesprüht und verdichtet werden, um eine hierarchische poröse Schicht zu erhalten, die als Katalysator, z. B. im Fischer-Tropsch-Prozess, eingesetzt werden kann.

---

[110] POUL L HANSEN et al. *Science*, **295**: 2053–2055, 2002.
[106] AURINA MARTÍNEZ ARIAS & ALFRED P. WEBER. *J. Aerosol Sci.*, **131**: 1–12, 2019.

Der Bildungsmechanismus von durch Sprühtrocknung hergestellten nanopartikulären Clustern, werden sowohl für den Fall von hartkugelartigen als auch von elektrisch geladenen NPs diskutiert. Grundlage für die Diskussion sind experimentell und numerisch ermittelte Feststoffvolumenanteile und PorengröSSenverteilungen aus realen (im Labor hergestellten) bzw. computergenerierten BBs. Für den Fall von Clustern aus geladenen NPs wird ein Bildungsmechanismus vorgeschlagen, bei dem der kolloidalen Silica-Dispersion ein hydratisiertes Metallsalz und HCl zugesetzt wird. Die Menge des zugegebenen hydratisierten Salzes erwies sich einerseits als von entscheidender Bedeutung, da bei Temperaturen oberhalb $100\,^{\circ}\mathrm{C}$ der Dehydrierungsprozess der Salze ein zweites und hochreines Wasserreservoir bereitstellt, das eine zweite Verdampfungsstufe im Trocknungsprozess hervorruft. Andererseits fängt das hinzugefügte Metallsalz das während der ersten Trocknungsstufe verdampfende HCl auf, bevor es aus der Siliziumdioxidstruktur entweicht, was sich negativ auf die elektrostatischen Wechselwirkungen zwischen den NPs durch nachfolgende Absenkung des pH-Wertes auswirkt. Es wird gezeigt, dass die PorengröSSe und der Feststoffvolumenanteil der Cluster durch die Einstellung der HCl-Retention in der Siliziumdioxid-Struktur kontrolliert werden können, was wiederum auf eine Modifikation der elektrischen Kräfte zurückzuführen ist. Letzteres kann nämlich ausgenutzt werden, um die PorengröSSe durch die abstoSSende Wirkung der elektrischen Kräfte zu erweitern.

5.2 Abstract

A strategy to control the pore size of mesoporous nanoparticulate clusters produced by spray-drying is presented. Further, we propose a mechanism of formation induced by the electrostatic interactions between the colloidal nanoparticles. Experimental results showing the effect of these interactions on the solid volume fraction and pore size of the clusters are provided and supported with our simulation results. Due to the complexity of the system and limited computational resources, simulations usually consider a limited number of particles focusing on the phenomena occurring at the interface of the evaporating droplet. As surface-induced effects propagate into the assembly ony within a few particle shells, the bulk structure of large clusters remains unresolved by these particle-based approaches. Here, we use an alternative approach to reproduce the bulk structure of large clusters, for which the contribution of surface-induced effects can be neglected.

5.3 Introduction

Colloidal silica nanoparticles (NPs) are used in many applications such as catalysis, pharmaceuticals and coatings. Due to the tendency of colloids to self-assemble, colloidal dispersions are usually stabilized against aggregation. However, if the self-assembly process is carried out in a controlled way, aggregation can be exploited to obtain nanoparticulate clusters with tunable properties. The catalytic, optical, and electronic properties of a nanomaterial can be affected by its size, shape and structure to a degree that is not easily predictable.[110,111] Strategies for the synthesis of mesoporous aggregates with adjustable pore size offer possibilities to meet these challenges.[110] In the present study, we use a spray-drying technique to synthesize mesoporous nanoparticulate clusters.[106] This is a well-established synthesis strategy where a colloidal dispersion of silica NPs is atomized into droplets of a few microns, that subsequently undergo a drying process. As the droplet shrinks, NPs assemble to form a spherical cluster with mesoporous structure, also known as building block (BB).[106] By adding a metal to the dispersion, e.g. in the form of a metal nitrate, silica clusters supporting metallic NPs can be synthesized. In a subsequent step, the produced BBs can be sprayed and compacted to obtain a hierarchical porous layer which is suitable to be used as catalyst, e.g. in the Fischer-Tropsch process.

Geometric confinement of colloidal NPs induced by evaporation of aerosols [14–20] or emulsions,[111,112] has been studied by several authors. However, the interactions considered in the numerical models in this work differ in that, for instance, long-range interactions such as electrostatic forces and hydrodynamic interactions (HIs), i.e., forces resulting from momentum transport between NPs through the solvent, are often not considered in numerical models since they imply a dramatic increase in computational complexity. Nevertheless, it is worth noting that HIs should not be neglected if the kinetics play an important role in the formation of the cluster structure, as in the case of surface-induced crystallization.[15] In contrast, when the equilibrium structures are preponderant, it has been found that HIs do not affect the resulting structures.[33,111,113]

Electrostatic interactions depend on many physical parameters such as temperature, electric permittivity of the solvent, pH value and ion concentration. These parameters vary

---

[111] Junwei Wang et al. *Nat. Comm.*, **9**: , 2018.
[14] M. Mezhericher et al. *Chem. Eng. Sci.*, **66**: 884–896, 2011.
[15] Michael P. Howard et al. *J. Chem. Phys.*, **149**: 094901, 2018.
[16] Katarzyna Jabłczyńska et al. *Adv. Powder Technol.*, **29**: 3542–3551, 2018.
[17] Sabrina Zellmer et al. *ACS Nano*, **9**: 10749–10757, 2015.
[18] Thomas Breinlinger et al. *J. Am. Ceram. Soc.*, **98**: 1778–1786, 2015.
[19] Thomas Breinlinger et al. *Powder Technol.*, **283**: 1–8, 2015.
[20] Wendong Liu et al. *ACS Nano*, **13**: 4972–4979, 2019.
[112] Bart De Nijs et al. *Nat. Mater.*, **14**: 56–60, 2015.
[33] John F. Brady. *J. Fluid Mech.*, **272**: 109–133, 1994.
[113] Adolfo J. Banchio et al. *J. Chem. Phys.*, **148**: 134902, 2018.

during the drying process, making a direct quantitative comparison between simulations and experiments difficult. This might be the reason why there is a lack of research on charge-stabilized colloidal dispersions,[31,113–116] while colloidal suspensions of hard spheres have been investigated by several researchers.[15,30,32–34,117–122] In this work, we consider both the effect of long-range electrostatic interactions and the hydrodynamic interactions between the NPs. Clusters containing a large number of NPs are studied. The NPs in turn have a high diffusivity due to their size, which is relatively small, i.e. in the order of a few nanometers, compared to the NPs usually used in other studies,[16,17,111,123] in the order of hundreds of nanometers. The clusters were produced by spray-drying, which implies relatively short evaporation times. As a result of the above conditions, we obtain clusters whose structure shows mainly a bulk-like configuration. The latter has been documented in the relationship between the viscosity and self-diffusivity of colloidal dispersions with its volume fraction.[33–35,124,125] We exploit the fact that the physics underlying the bulk structure formation of clusters resemble the mechanics behind the bulk structure of colloidal suspensions and model their inner configuration based on the self-diffusivity of the NPs in bulk suspension.

We discuss an experimental procedure to synthesize catalytic active clusters with controlled pore size (catalytic metal oxides supported on amorphous mesoporous silica) and propose a mechanism of formation. This strategy can be used to optimize the balance between the surface area available to reaction and the limiting mass transport within the narrow pores of reactants and products involved in catalytic processes such as the Fischer-Tropsch synthesis. Here, as the pore size of the clusters reaches the order of magnitude of the diffusing molecules, mass transport suffers a dramatic decrease.

---

[31] P. R. Schunk et al. *J. Rheol.*, **56**: 353–384, 2012.
[114] Brian Giera et al. *Langmuir*, **33**: 652–661, 2016.
[115] A. Imhof et al. *J. Chem. Phys.*, **100**: 2170–2181, 1994.
[116] Amit Kumar & Jonathan J.L. Higdon. *Phys. Rev. E*, **82**: 051401, 2010.
[30] Pieter J. In't Veld et al. *Phys. Rev. E*, **79**: 10–13, 2009.
[32] Dan S Bolintineanu et al. *Comput. Part. Mech.*, **1**: 321–356, 2014.
[34] Clara Weis et al. *Sci. Rep.*, **6**: 1–15, 2016.
[117] Jeffrey F. Morris & John F. Brady. *J. Fluid Mech.*, **312**: 223–252, 1996.
[118] Thanh N. Phung et al. *J. Fluid Mech.*, **313**: 181–207, 1996.
[119] David R. Foss & John F. Brady. *J. Fluid Mech.*, **401**: 243–274, 1999.
[120] N Koumakis et al. *Phys. Rev. Lett.*, **108**: , 2012.
[121] Shengfeng Cheng & Gary S Grest. *J. Chem. Phys.*, **138**: 64701, 2013.
[122] N. Koumakis et al. *J. Rheol.*, **60**: 603–623, 2016.
[123] Carsten Schilde & Arno Kwade. , **27**: 672–684, 2012.
[35] Heather M. Shewan & Jason R. Stokes. *J Non-Newton Fluid*, **222**: 72–81, 2014.
[124] J. Brady & Goerges. Bossis. *Annu. Rev. Fluid Mech.*, **20**: 111–157, 1988.
[125] Morton M. Denn et al. *Soft Matter*, **14**: 170–184, 2018.

Table 5.1: Type of cluster configurations and range of their solid volume fractions obtained in this work and by other authors. All the clusters were produced by drying of droplets dispersed as aerosols or emulsions using approximately monodisperse NPs. The prevalent cluster structures are random close packing (rcp), polycrystalline (PC), and monocrystalline (MC) configurations, which appear as fcc or icosahedral (ico) arrangements.

Reference	**Dispersion/NPs**	Φ / –	Structures
This work	Aerosol/SiO_2	0.578 to 0.723	rcp, PC
This work	Aerosol/SiO_2 + Co_3O_4	0.458 to 0.559	rcp, PC
Schilde et al. [123]	Aerosol/SiO_2	0.604 to 0.758	rcp, PC
Wang et al. [111]	Emulsion/PS	0.689 to 0.740	MC: ico
De Nijs et al. [112]	Emulsion/Co-Fe oxide	0.688 to 0.689	MC: ico, fcc

5.4 Results and Discussion

We use the solid volume fraction and pore size of the produced clusters as descriptors of their mesoporous structure. Depending on the magnitude of the volume fraction, the dominant arrangement of the NPs can be identified. For instance, crystalline structures usually show compacter arrangements with a higher solid volume fraction than that of disordered arrangements. Based on this, we could determine that the clusters produced in this work show a predominant disordered structure. Such a structure is known as random close packing (rcp) and is related with solid volume fractions of around 0.63 in contrast to the fraction of a face-centered cubic structure (fcc) of 0.74. We compare our results with solid volume fractions obtained in other works in Table 5.1.

The principal factors determining the final structure of a cluster are the evaporation time and the time scale of diffusion, as well as the number of NPs per cluster and their polydispersity. The ratio of both time scales (i.e. evaporation time to self-diffusivity time scale) will ultimately determine the influence of the evaporation kinetics on the structure. In general, three characteristic structures can be formed depending on this ratio, also known as the Péclet number: A polycristalline structure in the outer shells, a disordered (rcp) structure, and monocrystalline configuration in the inner layers of the cluster. Surface-induced nucleation/crystallization are kinetic effects, which induce the predominant polycrystalline structure present in the shells near to the droplet interface. In contrast, disordered or monocrystalline bulk structures are thermodynamically induced[33] and begin to dominate the structure a few layers from the outer cluster shell.[15,21,76,79] Hence, the

---

[21] HECTOR RUSINQUE et al. *Comm. Compu. Inf. Sci.*, **1199**: 104–121, 2020.

[76] STEFAN BRUNS et al. *J. Chromatogr. A*, **1318**: 189–197, 2013.

[79] ROBERT S. MAIER et al. *Phys. Fluids*, **15**: 3795–3815, 2003.

number of NPs per cluster affects the final structure, since more NPs result in more inner layers and thus more bulk structure, unaffected by kinetic effects. Further, if the evaporation process occurs slowly enough, i.e. in a time scale significantly larger than that of diffusion, thermodynamically favored bulk crystallization will prevail over disordered rcp structures and surface-induced crystallization due to the flexible droplet interface that allows the rearrangement and healing of defects.[111,112]

In the following, we present the experimental results for the first and second system shown in Table 5.1, as well as the model used to reproduce the solid volume fraction of the clusters. Although in both cases the colloidal NPs are stabilized by electrostatic forces, we explain in the next section why the NPs by the end of the evaporation process behave effectively as hard spheres.

5.4.1 Clusters of hard-sphere-like silica NPs

Amorphous silica NPs form stable colloidal dispersions. Preferential dissolution of surface species confers silica particles their characteristic surface charge. These charged sites consist of deprotonated silanols and are a function of the pH value and the ionic strength of the solution.[126] Hence, a dispersion of silica NPs is charged-stabilized, usually at basic pH values beyond the isoelectric point, i.e. pH > 2. However, even when approaching this point of zero charge, silica NPs can still show a high stability due to their weak attractive interactions. The latter has been related to their inherent surface roughness or "hairiness".[127,128] In order to enhance the stability of the dispersion, a basic pH is set e.g. by adding sodium or ammonium cations as counterions of the anionic silica NPs. However, this also increases the ionic strength of the solution, which will increase further with the evaporation of the solvent. Consequently, the screening effect on the electrostatic forces intensifies, up to a point where they effectively disappear and thus the colloidal NPs behave as hard spheres, i.e. short-range forces dominate the interactions between the NPs.

---

[126] H.E. Bergna & W.O. Roberts. *Colloidal Silica: Fundamentals and Applications*. Surfactant Science CRC Press, 2005.

[127] S Jenkins et al. *J. Chem. Phys.*, **224711**: 174704, 2007.

[128] Valentina Valmacco et al. *Nanoscale Horiz.*, **1**: 325–330, 2016.

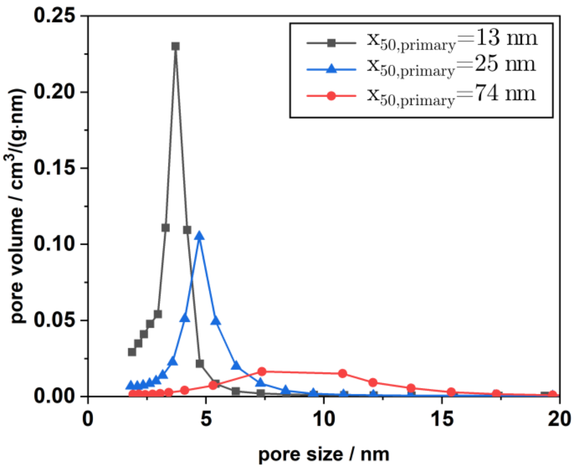

Figure 5.1: Pore size distribution of the produced clusters with different nanoparticle sizes.

Experimental part: Hard-sphere-like NPs

In order to assess the influence of the particle size and number of particles on the cluster structures, a series of experiments was conducted, where clusters were produced by spray-drying of silica suspensions with the same initial solid volume fraction of the suspension and different NP sizes. Notice that the number of NPs indirectly increases with decreasing particle size, since two crucial variables are kept constant, namely the initial volume fraction and the average droplet size in the atomization process. The experimental results are shown in Fig. 5.1, at which we can observe that the pore size increases with increasing particle size. Likewise, an increase in solid volume fraction with increasing particle size was observed with $\Phi = 0.578, 0.655$ and 0.699 for $x_{50,\text{primary}} = 13, 25$ and $64\,\mathrm{nm}$, respectively. Although it might seem counter-intuitive, the solid volume fraction (or its counter-part: the void fraction, also known as porosity) and the pore size do not directly correlate for the case of hard spheres. The solid volume fraction is primarily a function of the kind of configuration (e.g. fcc or rcp) and in a lesser degree of the NPs polydispersity as well as of the nature of the process (e.g. a mechanical or a thermal process).[36] The pore size depends strongly on the particle size, and only couples weakly with the solid volume fraction as it also depends on the polydispersity. Based on the values of the solid volume fraction obtained, the produced aggregates comprising larger and fewer NPs showed a structure dominated by surface-induced polycrystalline configurations, while the structure of clusters consisting of smaller and more NPs exhibited a larger and more porous bulk fraction. The latter is characterized by a disordered (rcp) arrangement and arises from the high diffusivity of NPs, whose strong thermal fluctuations, i.e. Brownian motion, distort the ordered equilibrium configuration so that the NPs get stuck in a jammed rcp arrangement before reaching the jammed fcc structure.[33] This predominant bulk structure is the focus of our numerical work, which consists in a particle-based model based on Newtonian dynamics. Here, the equation of motion of each particle in the ensemble is solved to obtain their trajectories, from which the mean square displacements of the particle ensemble can be calculated. The latter are needed to determine the self-diffusivity of the colloidal NPs in suspension. The description of the numerical model can be found in the Method section later in this paper.

---

[36] VASILI BARANAU & ULRICH TALLAREK. *Soft Matter*, **10**: 3826–3841, 2014.

Numerical part: Hard-sphere-like NPs

By computing the long-time self-diffusivity in colloidal dispersions at different concentrations, we are able to estimate the final solid volume fraction (i.e. the complementary value of the porosity), at which all the NPs lose their liquid-like mobility and form a jammed solid-like structure. This approach does not take into account the effect of the confining walls (i.e. the confining water/air interface) and consequently, the surface-induced polycrystalline region is neglected. The numerical results for the case of hard spheres are shown in Fig. 5.2, where the ratio of the self-diffusivity of infinitely dilute colloidal dispersions D_0 to the long-time self-diffusivity in concentrated colloidal suspensions D_L is plotted over the solid volume fraction Φ.

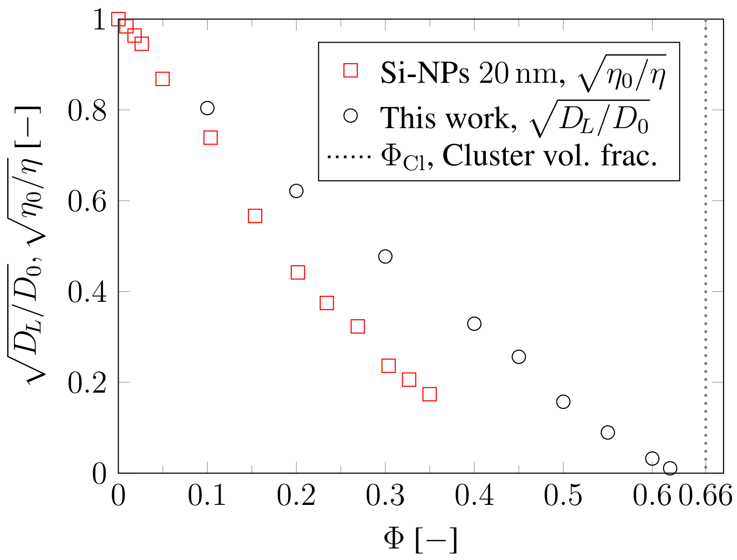

Figure 5.2: Relative diffusivity vs. solid volume fraction for a colloidal dispersion of hard-sphere-like particles.

According to earlier studies,[34,115] the steady-shear viscosity and long-time self-diffusivity of dispersions of hard spherical particles are still well coupled by the Stokes-Einstein relation. Based on this, we compared our numerical results for hard-sphere-like particles with the viscosity of the colloidal dispersion. Here, we vary the solid volume fraction of the suspensions and measured their viscosity. In Fig. 5.2, the final solid volume fraction, Φ_{Cl}, of the clusters produced with silica $25\,\mathrm{nm}$ NPs is represented with the dotted vertical line. The results show how the behavior of the colloidal silica NPs (red squares) deviates from the hard-sphere behavior (black circles). At low solid volume fractions this deviation is small, since the average distance between the NPs is larger than the range of the electrostatic interactions. As the solid volume fraction increases both curves separates. From about $\Phi = 0.1$ to $\Phi = 0.2$ the deviation increases sharply, signaling the interval in which the electrostatic interaction has the greatest influence on viscosity. After this, the increase in deviation gradually stops, which is an indication of the electrostatic forces being screened by the more concentrated amount of ions dissolved in the water (i.e. in the dispersion medium). Although we could not measure viscosity values for solid volume fractions larger than $\Phi = 0.35$, we *did* measure the solid volume fraction of the produced clusters via porosimetry and found that the value of the solid fraction coincides with the solid fraction reached in random closed packings (of hard spheres). This indicates that the deviation between the curves in Figure 5.2 must eventually decrease until both curves converge, which is explained by the stronger screening effect that ends up fully suppressing the electrostatic forces. In the numerical part of the following section, we consider the case, where electrostatic forces are kept constant with increasing solid volume fraction and show how the deviation between the hard-sphere case and the charged particles evolves.

5.4.2 Clusters produced in two evaporation stages: Effect of the electric forces

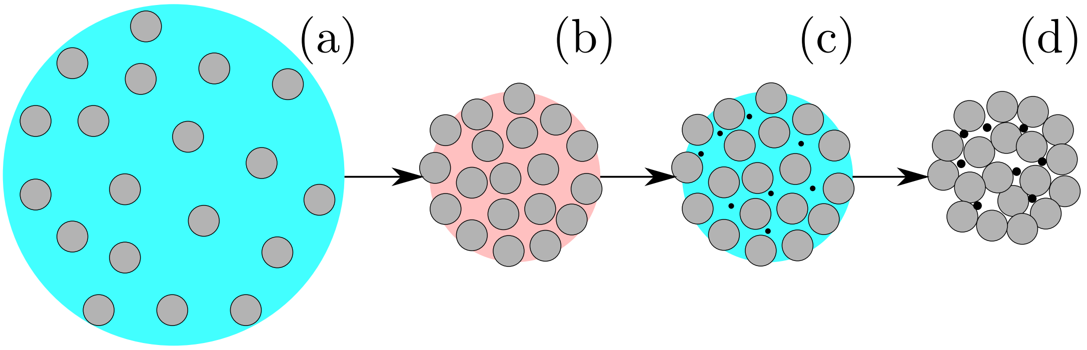

Figure 5.3: (a) Initial state of a droplet of the atomized dispersion prior to the first evaporation stage. The larger (blue) circle represents a droplet and the inner (gray) circles represent the dispersed nanoparticles. (b) Final state of the first stage and initial state of the second evaporation stage. The change in color of the dispersion medium indicates the transformation from water (in blue) to crystals of hydrated metallic salts (in red). (c) Secondary water reservoir as ultra-pure dispersion medium. The increase in temperature leads to the dehydration of the metallic salts and consequently to the second evaporation stage, where the metallic components agglomerate to form metallic NPs (black circles). (d) Dried nanoparticulate cluster.

In this section, we consider the effect of the electrostatic interactions on the structure of the nanoparticulate clusters produced. By adding a hydrated metal salt (cobalt nitrate hexahydrate) to the suspension, a second evaporation stage beyond $100\,°\mathrm{C}$ is promoted during the drying process, where ultrapure water is released from the crystallized hexahydrates (see Fig. 5.3).[129] In this ion-free background, repulsive electrostatic forces dominate over both attractive forces, the capillarity and dispersion forces, resulting in expansion/dilation of the narrow pores. Already at a nitrate loading of $3.8\,\%$ an increment of the pore size can be observed for the clusters comprising silica NPs with a mean particle size of $13\,\mathrm{nm}$. The range or width of the pore size distribution does not change with the amount of cobalt nitrate added, i.e. with the amount of water of the secondary evaporation stage. However, the number of pores is affected by this amount of cobalt nitrate, as cobalt NPs are formed during the drying process, occupying the pores of the silica structure and eventually clogging them.

In order to vary the strength of the "reactivated" electrostatic forces during the second evaporation stage, the ion concentration and the pH value of the suspension were modified by adding hydrogen chloride (HCl) in a step prior to the spray drying process. However, the added HCl partially evaporates together with the water during the first evaporation stage, whereby a fraction of the added amount leaves the forming cluster structure.

---

[129] Fiona A Wigzell & S. David Jackson. *Appl. Petrochem. Res.*, **7**: 9–21, 2017.

Therefore, only the HCl remaining in the porous structure can ultimately be absorbed by the secondary water reservoir. The amount of HCl retained within the forming cluster depends on both a steric and a chemical factor. The former concerns the size of the pores, which can be so narrow that they sterically hinder the escape of the hydrogen chloride molecules from the porous structure. The second factor mentioned is based on a chemical process in which the hydrogen chloride molecules are adsorbed within the cavities of the cluster. This adsorption process is enabled by the presence of the metal nitrate hydrates, which might react chemically with the HCl to form a salt, as suggested by Sharma et al., 2020.[12] Hence, the concentration of cobalt nitrate hexahydrate ($Co(NO_3)_2 \cdot 6\,H_2O$) has a direct impact on the retention of the HCl molecules, and consequently on the electrostatic forces. Dissolved HCl has a suppressing effect on both the range and magnitude of the electric forces: On the one hand, its ions reinforce the screening effect (i.e. they shorten the range of the electric force). On the other hand, its acidic nature lowers the pH, which reduces the surface charge of the silica NPs (i.e. it lowers the magnitude of the electric force). Thus, an increase in HCl retention leads to a reduction of the pore size and porosity due to the weaker electric (repulsive) forces. Building on this, there must be an initial concentration of HCl and hydrated $Co(NO_3)_2$ above which the quantity of adsorbed HCl will suffice to effectively deactivate the electrostatic interactions, resulting in clusters with similar porous structure to that of the clusters produced in only one evaporation stage.

Experimental part: Charged NPs

In the following, we asses the effect of the pore size on the retention of HCl by varying the primary particle size of the produced clusters. For this purpose, we used silica NPs with mean diameters of 13 and $25\,\mathrm{nm}$, whose related pore sizes can be seen in Fig. 5.1. Furthermore, two cobalt nitrate loadings were considered, $3.8\,\%$ and $20\,\%$ (loading understood as the percentage of mass of cobalt per mass of silica), in order to evaluate their impact on the retention of HCl. The addition of cobalt nitrate reduces the original pH of the suspension from above 9 to approx. 7. The subsequent addition of HCl lowers further the pH value. The results presented in Figures 5.4 and 5.5 include the original suspension without any addition of cobalt nitrate or HCl (i.e. pH above 9), the suspension with added cobalt nitrate and without HCl (pH around 7) as well as at least one suspension with the addition of both cobalt nitrate and HCl.

---

[12] Ravi Sharma et al. *Chem. Eng. J.*, **381**: 122512, 2020.

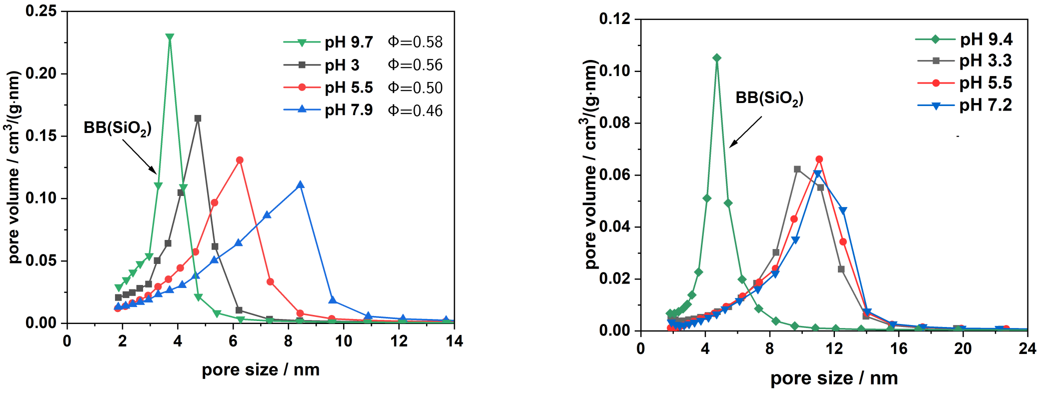

(a) Silica $13\,\mathrm{nm}$

(b) Silica $25\,\mathrm{nm}$

Figure 5.4: Effect of the pore size (or particle size) and cobalt nitrate concentration on the retention of HCl for a cobalt nitrate loading of $3.8\,\%$.

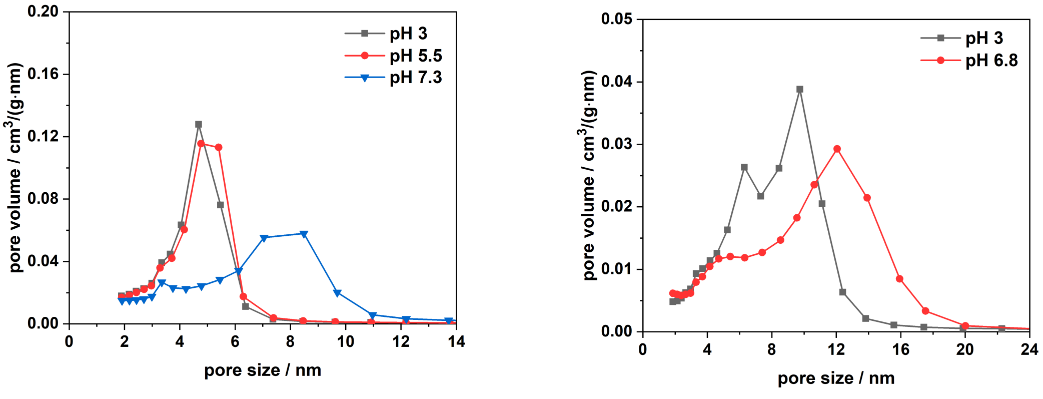

(a) Silica $13\,\mathrm{nm}$

(b) Silica $25\,\mathrm{nm}$

Figure 5.5: Effect of the pore size and cobalt nitrate concentration on the retention of HCl for a cobalt nitrate loading of $20.0\,\%$.

In general, the results show that the addition of cobalt nitrate (with or without HCl) increases the pore size of the clusters. This can be explained by the fact that cobalt NPs are formed during the drying process due to supersaturation of the evaporating water. These crystals accommodate within the cavities of the cluster, acting as a template (i.e. a steric obstacle impeding the interactions between the larger silica NPs). The results in Fig. 5.4a for silica $13\,\mathrm{nm}$ show a gradual decrease in pore size as the concentration of HCl increases, which in turn leads to weaker repulsive interactions between NPs. This indicates that within the narrow pore structure of the forming clusters, the concentration of added cobalt nitrate was sufficiently high to capture a sensible amount of HCl. In contrast, the same amount of cobalt nitrate for the case of silica $25\,\mathrm{nm}$, i.e. for larger pores, did not retain sufficient HCl to affect the electrostatic interactions, which can be seen in Fig. 5.4b, where the pore size remains unchanged with the increase in HCl concentration (i.e. the reduction of the pH value below 7). In Figures 5.4a and 5.5a for silica $13\,\mathrm{nm}$, an abrupt change in pore size can be seen after adding HCl (pH 5.5). Here, the pore narrows abruptly to the apparently minimal size reachable in the presence of the forming cobalt NPs. This can be explained by the larger amount of cobalt nitrate added, which leads to an enhanced retention of HCl, which suffices to effectively deactivate the electrostatic interactions between the silica NPs. A similar behavior was observed for silica $25\,\mathrm{nm}$ with a cobalt loading of $20\,\%$ (see Fig. 5.5b). A bimodality in the pore size distribution was also observed. This can be attributed to the selective formation of cobalt NPs in pores larger than $6\,\mathrm{nm}$, since these NPs reach sizes from $6\,\mathrm{nm}$ to $15\,\mathrm{nm}$. Thus, the smaller pores not only remain intact but also increase in number as the partially filled, larger pores become smaller.

In contrast to the hard-sphere case, the solid volume fraction strongly correlates with the pore size, as the void space between the NPs is being expanded by the action of the electrostatic interactions. Therefore, the solid volume fraction decreased with increasing HCl content, i.e. with the vanishing of the electrostatics interactions (see values in Fig. 5.4a). Note that the solid volume fraction of the clusters produced without any addition of nitrate or HCl $\Phi = 0.58$, is very similar to that of the clusters produced with the highest content of HCl, i.e. the lowest pH of 3, $\Phi = 0.56$. This supports the idea that the silica NPs conform the structural skeleton of the clusters, while the cobalt NPs formed during the drying process just fill the cavities of the silica structure without substantially changing it.

Numerical part: Charged NPs

In order to quantify the effect of the electrostatic interactions on the cluster porous structure, their magnitude was varied by means of numerical simulations. We used a particle-based mesoscopic model, which reproduces the behavior of a well-stabilized colloidal dispersion. The model uses an approximation of a repulsive hard-sphere potential plus a screened Coulomb potential, as the effective colloidal pair potential.[30–32,113] As already stated, we focus on the bulk structure, predominant in clusters produced with smaller NPs by spray-drying. For this purpose, we compute the self-diffusivity of the NPs moving in a bulk region, i.e. without the influence of the droplet-air interface (see Fig. 5.6), as the solid volume fraction, Φ, of the cluster increases (i.e. as the water content decreases).

By tracking the long-time self-diffusivity of the NPs, we are able to estimate the solid fraction at which the NPs configuration reaches a jammed state (i.e. the point during the drying process at which the particles completely lose their mobility and get stuck in a mechanically stable configuration).

As a measure of the magnitude of the electrostatic interactions, we used the electric surface potential. Its ordering effect on the cluster configuration can be seen qualitatively in Fig. 5.6, where for the same solid volume fraction, $\Phi = 0.45$, the electric surface potential was increased. Here, the crystallized fraction represented in green increases with the electric surface potential. These crystals were identified using the common neighbor analysis tool of the open-source software Ovito.[130] A diagonal cutting plane was introduced to show the inner part of packing computation domain, i.e. the cluster.

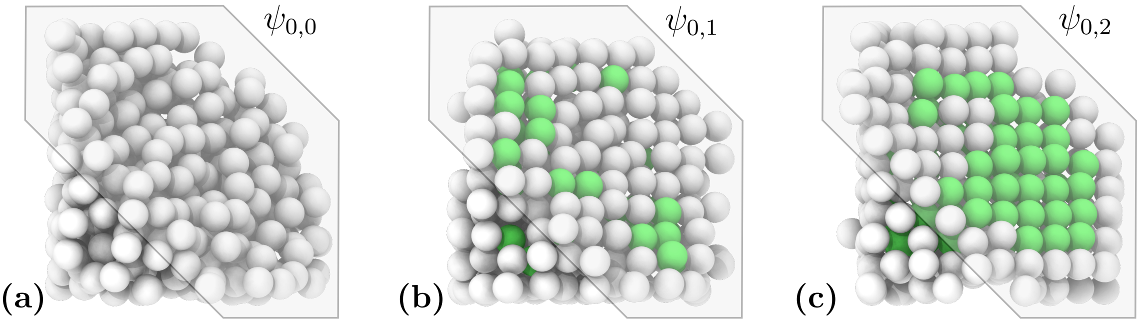

Figure 5.6: Structural order vs. surface potential with $\psi_{0,2} = 115\,\mathrm{mV}$, $\psi_{0,1} = 50\,\mathrm{mV}$, $\psi_{0,0} = 0\,\mathrm{mV}$ (i.e. hard spheres) and an ionic strength of $0.01\,\mathrm{mol\,L^{-1}}$.

The results for the self-diffusivity for three different electric surface potentials, $\psi_{0,a} = 10\,\mathrm{mV}$, $\psi_{0,b} = 48\,\mathrm{mV}$, $\psi_{0,c} = 72\,\mathrm{mV}$ and an ionic strength of $0.03\,\mathrm{mol\,L^{-1}}$, are shown in Fig. 5.7. We considered NPs with a diameter of $13\,\mathrm{nm}$ dispersed in a medium with a relative electric permittivity $\epsilon_r = 34$ at $200\,^{\circ}\mathrm{C}$.[131] These are similar conditions to those that can be expected during the final evaporation stage. However, the exact conditions of ionic strength and surface electric potential are not accessible by measurements.

As analytically deducted by Brady 1994,[33] for the case of hard spheres, the long-time self-diffusivity vanishes quadratically as it approaches the maximum solid volume fraction, $\Phi_m \approx 0.63$

$$D_L/D_0 \propto 1/1.26 \cdot \underbrace{0.85(1-\Phi/\Phi_m)}_{\text{Hydrodynamics}}\,\underbrace{1/1.2(1-\Phi/\Phi_m)}_{\text{Contact}} = 0.562(1-\Phi/\Phi_m)^2. \quad (5.1)$$

This deduction is in line with the viscosity model of Maron and Pierce,[132] which is commonly used to describe the relative viscosity of hard-sphere dispersions beyond the dilution regime.[35] As explained in the previous section, $\eta_0/\eta = D_L/D_0$ for hard spheres, via the Stokes-Einstein relation, so that the Maron and Pierce equation can be written as follows

---

[130] Alexander Stukowski. *Model. Simul. Mat. Sci. Eng.*, **20**: 045021, 2012.

[131] Siti Machmudah et al. *Hydrolysis of Biopolymers in Near-Critical and Subcritical Water*. Elsevier Inc., 2017. 69–107

[132] Samuel H. Maron & Percy E. Pierce. *J. Colloid Sci.*, **11**: 80–95, 1956.

$$D_L/D_0 = (1 - \Phi/\Phi_m)^2, \tag{5.2}$$

or reorganized into the following linear form

$$\sqrt{D_L/D_0} = 1 - \Phi/\Phi_m\,. \tag{5.3}$$

The first term in Eqn. 5.1 corresponds to the vanishing of the hydrodynamic interactions between particles as the mobility of the NPs drastically decreases, while the second term represents the particle-particle contact interactions.[33,35] Eqn. 5.3 explains the linear decrease of the square-root of the diffusivity ratio, $\sqrt{D_L/D_0}$, shown in Fig. 5.2. However, we did not observe the same behavior in the case of the charged particles. This can be explained by the fact, that electrostatic interactions exponentially grow with decreasing distance between the interacting particles, preventing them from touching each other. At short distance, the mobility of the NPs will be dramatically hindered by the long-range repulsive electric forces, so that solid-like structures begin to form, i.e. colloidal crystals, see green spheres in Fig. 5.6. Since direct contact between the particles is highly unlikely for the case of charged particles, the second term in Eqn. 5.1 can be neglected. Hence, we fitted the diffusivity values of the charged particles to the following linear equation

$$D_L/D_0 = K_{\mathrm{el}}(1 - \Phi/\Phi_m), \tag{5.4}$$

which is applied only for large values of the solid volume fraction. Here, K_{el} is a coefficient that depends on the electric surface potential. Further, Φ_m can be read from the intersection of the fitting function with the horizontal axis (see Fig. 5.7).

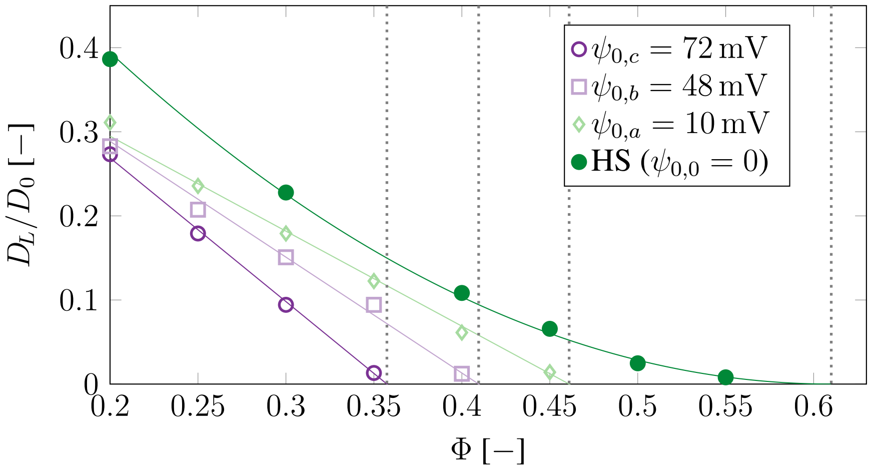

Figure 5.7: Relative diffusivity vs. solid volume fraction for different electric surface potentials with the same ionic strength.

Note that in Fig. 5.7, the diffusivity ratio (instead of its root-square) is plotted against the solid volume fraction. Therefore, the hard-sphere case (HS) shows a quadratic decay in accordance to the Maron-Pierce equation (Eqn. 5.2). For the case of charge-stabilized NPs, the suggested function, Eqn. 5.4, shows an excellent agreement with the numerical results for large values of solid volume fraction as it approaches the maximum solid fraction, Φ_m. We have successfully verified this behavior and the implementation of the numerical model with the experimental results of Holmqvist and Nägele [133].

We used Eqn. 5.4 to quantitatively estimate the maximum value reached by the solid fraction for each electric surface potential considered. These values are $\Phi_a = 0.461$, $\Phi_b = 0.410$, $\Phi_c = 0.357$. It is clear from the results that relatively small variations in electric surface potential can have a sensible impact on the final solid fraction of nanoparticulate clusters. Though the exact conditions of pH and ion concentration remain uncertain, we considered realistic surface potential values.[134] Note that the dielectric constant (also known as relative permittivity) of water is cut approx. in half at the evaluated temperature of $200\,°\mathrm{C}$ in comparison to its value at $25\,°\mathrm{C}$.[131] This should lead to proportionally higher electric surface potentials.[135] Building on this, the highest electric surface potential evaluated, $\psi_{0,c} = 72\,\mathrm{mV}$, should still be within a reasonable and realistic range for colloidal silica dispersions. The obtained values of solid volume fractions in the numerical calculations led to smaller values than those obtained in the experiments ranging from 0.46 to 0.58. This may indicate that the NPs rearrange themselves in a more compact configuration either towards the end of the secondary evaporation stage or afterwards in a dried state during the consolidation of the structure.

5.5 Conclusions

The formation mechanism of nanoparticulate clusters produced via spray-drying was discussed for both the case of hard-sphere-like and charged NPs. The base for the discussion were the solid volume fractions and pore size distributions obtained by experimental and numerical means. A formation mechanism for the case of clusters consisting of charged NPs was suggested, at which a hydrated metallic salt and HCl have to be added to the colloidal silica dispersion. The amount of added hydrated salt showed to be of vital importance, on the one hand, as it provides a second and highly pure water reservoir at temperatures over $100\,°\mathrm{C}$, inducing a second evaporation stage in the drying process. On the other hand, the added metallic salt captures the evaporating HCl before it escapes the silica structure, which negatively affects the electrostatic interactions between the NPs. It was shown that the pore size and solid volume fraction of the clusters can be controlled by adjusting the retention of HCl in the silica structure, which in turn adjusts the strength of the electric forces. The latter causes the electrical forces to proportionally dilate the pore size due to their repulsive character.

---

[133] PETER HOLMQVIST & GERHARD NÄGELE. *Phys. Rev. Lett.*, **104**: , 2010.
[134] CIGDEM O METIN et al. *J Nanopart Res*, **13**: 839–850, 2011.
[135] STACEY HARPER et al. *Environ. Sci. Nano*, **3**: 953–965, 2016.

5.6 Numerical and experimental methods

5.7 Methods

5.7.1 Materials

For the synthesis of the clusters, ammonium stabilised aqueous colloidal silica suspension with 3 different silica primary particle size were used as a support for the Co3O4 nanoparticles. The silica suspensions were obtained from CWK Chemiewerk Bad Köstritz GmbH. In this work 3 different silica sizes were investigated: 13 nm, (Köstrosol 0830AS, 30 wt %), 25 nm, (Köstrosol 2040AS, 40 wt %), and 64 nm, (Köstrosol 4550, 50 wt %). For the synthesis of cobalt oxide nanoparticles cobalt (II) nitrate hexahydrate, $Co(NO_3)_2 \cdot 6\,H_2O$, from Sigma-Aldrich was used as the precursor. Small amounts of hydrochloric acid (HCl) were used to decrease the pH value of the prepared suspensions before the spray drying process. Deionized water was used as a solvent in all the suspensions. All materials in this work were used as received without further treatment.

5.7.2 Characterization

The structure and morphology of the clusters were examined with Scanning Electron Microscopy (SEM). The analyses were carried out with a Zeiss DSM Gemini 982 operated at 5 kV. The zeta potential and electrophoretic mobility of the suspensions before spray drying were light scattering with a Zetasizer Nano ZS (Malvern Panalytical). The thermal decomposition of the cobalt nitrate to cobalt oxide was analysed with a Thermogravimetric analysis (TGA). The experiments were carried out in the temperature range of 20 to $1000\,^{\circ}\mathrm{C}$ under air conditions with a heating rate of 10 K/min using a NETZSCH TG 209 F1 thermogravimetric analyser. Nitrogen adsorption-desorption isotherms were recorded with an ASAP 2020 from Micromeritics GmbH. The pore size distributions and total pore volume of the BBs were calculated according to the Barrett-Joyner-Halenda (BJH) model. Generally, a sample mass between 100-150 mg was degassed for 2 h at a temperature of $250\,^{\circ}\mathrm{C}$ before analysis. During the measurements, several data points for adsorption and desorption isotherms were collected.

5.7.3 Particle simulation

To model the motion of the colloidal nanoparticles (NPs), we use Fast Lubrication dynamics (FLD),[116,136,137] which is an approximation to Stokesian dynamics (SD).[118,119,124] As in other methods based on N-body Newtonian dynamics such as the mentioned SD, as well as Langevin and Brownian dynamics, the external forces applied to the particles are divided into conservative forces $\mathbf{F}^{\mathrm{P}}$, and the interactions with the solvent. The latter are described by the fluctuation-dissipation theorem, namely the fluctuating Brownian force $\mathbf{F}^{\mathrm{B}}$ and its counterpart, the dissipative hydrodynamic force $\mathbf{F}^{\mathrm{H}}$. This results in the following equation of motion for the NPs

$$\mathbf{m}\frac{d\mathbf{U}}{dt} = \mathbf{F}^{\mathrm{H}} + \mathbf{F}^{\mathrm{B}} + \mathbf{F}^{\mathrm{P}}\,, \tag{5.5}$$

where $\mathbf{U}$ is the particle translational/rotational velocity vector of dimension $6N$. $\mathbf{F}^{\mathrm{P}}$ is a conservative force due to interparticle or external potentials.

When the particle Reynolds number is small, the hydrodynamic force exerted on the particles in a suspension in the absence of bulk shear flow is

$$\mathbf{F}^{\mathrm{H}} = -\mathbf{R}\mathbf{U}\,, \tag{5.6}$$

where the hydrodynamic interactions are directly proportional to the particle translational/rotational velocities $\mathbf{U}$. $\mathbf{R}$ stands for the hydrodynamic resistance tensor as the proportionality factor.

The stochastic Brownian force $\mathbf{F}^{\mathrm{B}}$ is the mesoscopic manifestation of the thermal motion of fluid particles and is given by

$$\left\langle \mathbf{F}^{\mathrm{B}} \right\rangle = 0\,, \tag{5.7}$$

$$\left\langle \mathbf{F}^{\mathrm{B}}(0)\mathbf{F}^{\mathrm{B}}(t) \right\rangle = 2k_{\mathrm{B}}T\mathbf{R}\delta(t)\,. \tag{5.8}$$

The angle brackets indicate an ensemble average, k_B and T are the Boltzmann constant and the absolute temperature, respectively, and $\delta(t)$ is the Dirac delta function.

In this work, as conservative forces we consider the DLVO (Derjaguin-Landau-Verwey-Overbeek) interactions, i.e. those forces that arise from the Van der Waals (VdW) and screened Coulomb pair potentials. The VdW forces in turn are composed of an attraction

---

[136] MICHAEL DEAN BYBEE. *Hydrodynamic Simulations of Colloidal Gels: Microstructure, Dynamics, and Rheology*. Ph.D. dissertation. University of Illinois at Urbana-Champaign, 2003.

[137] AMIT KUMAR. *Microscale dynamics in suspensions of non-spherical particles*. Ph.D. dissertation. University of Illinois at Urbana-Champaign, 2010.

and a repulsion part, and are proportional to the Hamaker constant A_c. Their mathematical expressions are well documented in [32, 138].

Computation of the electrostatic interactions

Charged colloidal systems can be described by means of the DLVO pair potential. The electrostatic part of the DLVO potential takes the form of a screened Coulomb pairwise interaction, which in the case of two spherical particles of radius a, each carrying an effective charge Q_{eff} in a fluid of dielectric constant ϵ_r with a concentration n of monovalent ions is given as a function of the center-to-center distance r by

$$U_{\text{el}}(r) = \frac{Q_{\text{eff}}^2}{4\pi\epsilon_0\epsilon_r}\frac{e^{-r/\lambda_D}}{r} \quad \text{with} \quad Q_{\text{eff}} = \frac{e^{a/\lambda_D}}{1+a/\lambda_D}Q\,, \tag{5.9}$$

where Q is the actual charge of the particles, ϵ_0 is the vacuum permittivity, and λ_D is the screening Debye length.

The electric DLVO pair potential U_{el} can be linked to the electrostatic potential φ. The latter is derived from the analytical solution of the linearized Poisson-Boltzmann (PB) equation, known as the Debye-Hückel potential[139]

$$U_{\text{el}}(r) = Q_{\text{eff}}\,\varphi(r) \quad \text{with} \quad \varphi(r) = \frac{Q_{\text{eff}}}{4\pi\epsilon_0\epsilon_r}\frac{e^{-r/\lambda_D}}{r}\,. \tag{5.10}$$

In general, the PB equation is used to model the electrical double layer surrounding a charged surface in an electrolytic solution for the case of low salt concentrations $\lessapprox 0.003\,\text{mol}\,\text{L}^{-1}$.[140] Strictly speaking, both the Debye-Hückel potential as well as the electric part of the DLVO pair potential hold only for low electric potentials (i.e. $e\,|\varphi| \ll k_B T$, or as established standard $\varphi \leq 25\,\text{mV}$). However, their use can be extended for a wider range of potentials, from $50 - 80\,\text{mV}$, as a good approximation.[141]

$$\epsilon_0\epsilon_r\nabla^2\varphi(r) = -\sum_{j=1}^{N} q_j n_j^0 \exp\left(-\frac{q_j\,\varphi(r)}{k_\text{B}T}\right) - \rho_\text{f}\,, \tag{5.11}$$

with boundary conditions

$$-\epsilon_0\epsilon_r\,\mathbf{n}\cdot\nabla\varphi = \sigma \quad \text{on} \quad r = a\,, \tag{5.12}$$

$$\varphi = 0 \quad \text{on} \quad r \longrightarrow \infty\,, \tag{5.13}$$

---

[139] K. Dill & S. Bromberg. *Molecular Driving Forces: Statistical Thermodynamics in Biology, Chemistry, Physics, and Nanoscience*. CRC Press, 2012.

[140] Jin Si Zhang et al. *Sci. Rep.*, **7**: , 2017.

[141] H.J. Butt et al. *Physics and Chemistry of Interfaces*. Physics textbook Wiley, 2003.

where the j-th species (e.g. dissolved ions) carries a charge q_j and has a concentration n_j^0. The surface charge density σ is imposed as a boundary condition on the particle surface.

In the determination of the screening length λ_D, there is no general consensus as to whether the counterions released by the colloidal particles contribute to their own screening or not .[142] The role of the volume fraction of the colloidal particles in the screening of the electric force is still under discussion.[113] We used the most established equation in literature and took into account the counterions of the deprotonated oxygen atoms, present in the hydroxyl groups of the silica surface, namely the following equation

$$\lambda_{\mathrm{D}} = \left(\frac{\sum_{j=1}^{N} n_j^0 \, q_j^2}{\epsilon_0 \epsilon_r \, k_{\mathrm{B}} T} \right)^{-1/2} . \tag{5.14}$$

5.8 Supporting information

5.8.1 Simulation details

In all calculations carried out, the colloidal particles are treated as finite-sized particles with translational as well as rotational degrees of freedom, LAMMPS atomic style "sphere". The parameters for the hard-sphere colloids are analogous to previous works [31, 32], where the particle radius is set to $a = 5\sigma$. Colloidal interactions are accounted for with the integrated Lennard-Jones potential, pair style "colloid" in LAMMPS, with a cut-off distance of $R_c = 2a + 30 - 1/6\sigma$ and a Hamaker constant of $A_{\mathrm{cc}} = 4\pi^2 \approxeq 39.478\varepsilon$. Notice that this interaction is not strictly hard, but is slightly softened to avoid particle overlap. The inner and outer cutoff distances for the FLD lubrication terms are set to $2.0002a$ and $3a$, respectively.

Verification: Charge-stabilized colloids

Here we present the verification of the model used in the simulation, for which the repulsive part of the DLVO potential has been implemented in LAMMPS, a widely-used open source software for molecular dynamics simulations.

A model system was considered equivalent to the silica system used in the numerical and experimental studies by Banchio et al. and Holmqvist et al., respectively.

---

[142] K S SCHMITZ et al. *J. Phys. Chem. B*, **107**: 10040–10047, 2003.

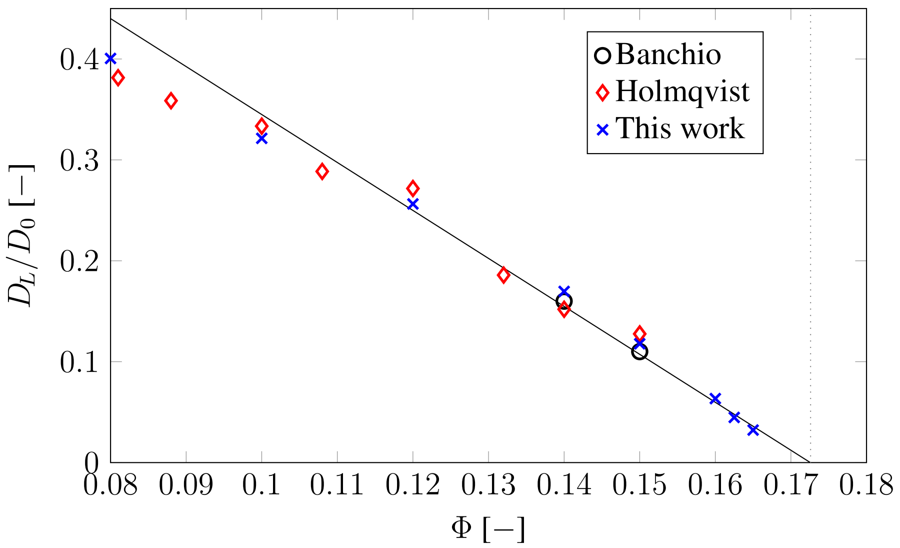

Figure 5.8: Relative diffusivity vs. volume fraction.

5.8.2 Materials characterization

The size of the primary nanoparticles used in the production of the clusters (Building blocks) were measured via dynamic light scattering (Zetasizer Nano ZS, Malvern) and their number-weighted particle size distributions are presented in Fig. 5.9

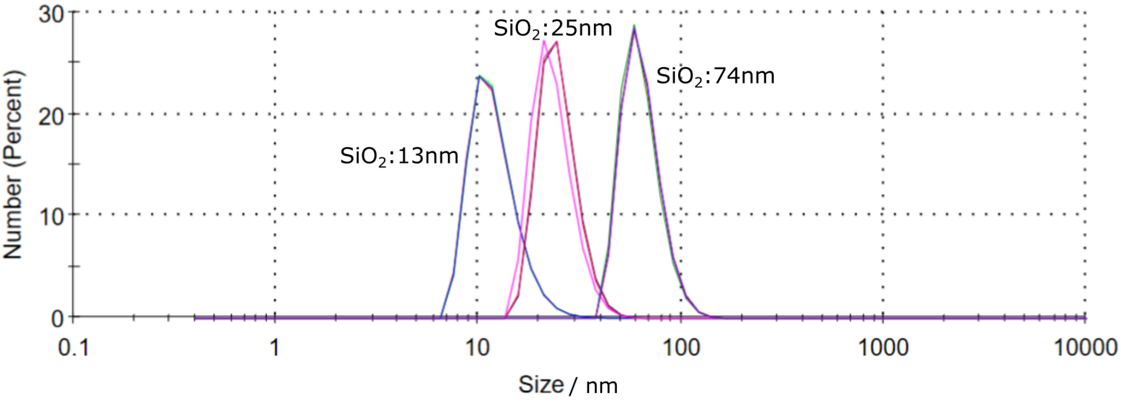

Figure 5.9: Number-weighted particle size distribution of the primary NPs used to produce the clusters.

5.8.3 Electric potential

Here, additional results are provided supporting the fact that the electrostatic potentials can be used for a wider range of potentials beyond the low region (i.e. $<25\,\mathrm{mV}$), by introducing the concept of effective number of charges, Z_{eff} ,[113] which takes values, in general, lower than the real number of charges, as shown in Fig. 5.10 and Fig. 5.11. Since we use relatively high electric potentials in our calculations, their accuracy is checked by comparing the numerical solution of the PB equation with the Debye-Hückel potential. The PB equation is solved in spherical coordinates (i.e. 1D) for each particle size, surface potential ($\varphi(a) = \psi_0$) and salt concentration considered. For this purpose, we used the open-source finite-element package FEniCS.[57,58]

The surface charge density imposed as boundary condition at the NP surface is calculated with [135]

$$\sigma = \epsilon_0 \epsilon_r \, \psi_0 \, (1 + a/\lambda)/a$$

.

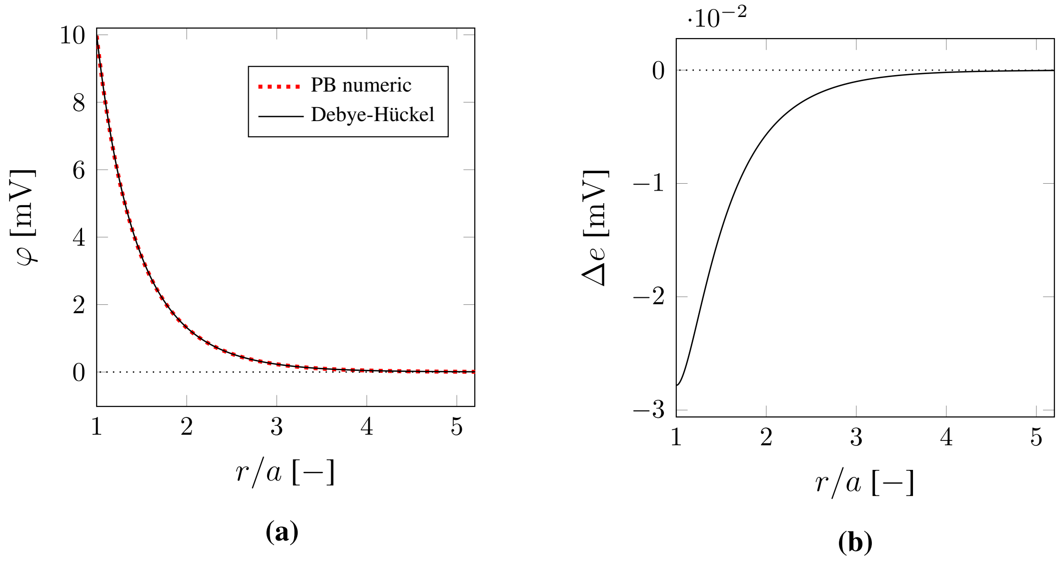

(a) **(b)**

Figure 5.10: Comparison of the numerical solution obtained from the PB solver with the Debye-Hückel potential of a NP of radius $a = 130.0\,\mathrm{nm}$, surface potential $\psi_0 = 15\,\mathrm{mV}$ in a solution $0.003\,\mathrm{mol\,L^{-1}}$ of a monovalent salt. The resulting screening Debye length for water at 20 °C is $\lambda_D = 173.1\,\mathrm{nm}$.

---

[57] MARTIN S. ALNÆS et al. *ACM T. Math. Software*, **40**: , 2014.

[58] MARTIN S. ALNÆS et al. *Arch. Num. Software*, **3**: , 2015.

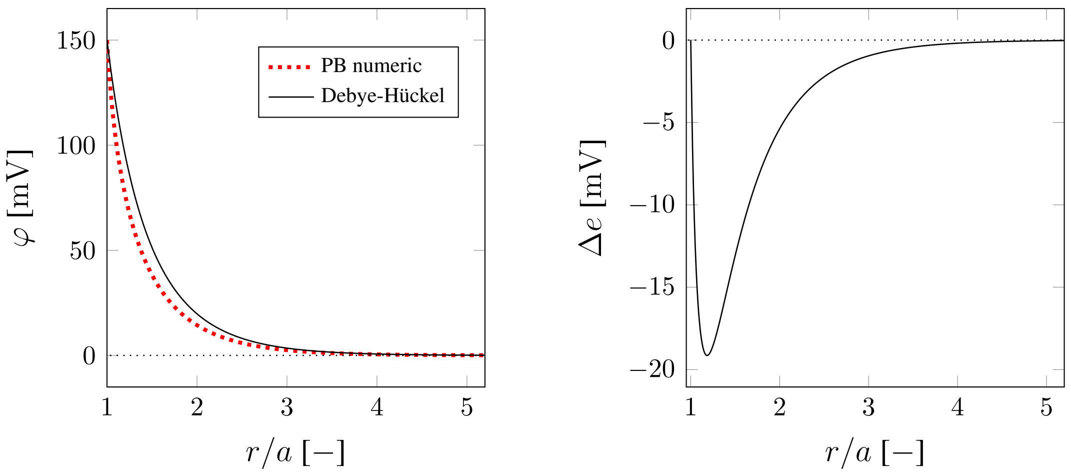

(a) **(b)**

Figure 5.11: Comparison of the numerical solution obtained from the PB solver with the Debye-Hückel potential of a NP of radius $a = 130.0\,\mathrm{nm}$, surface potential $\psi_0 = 150\,\mathrm{mV}$ in a solution $0.003\,\mathrm{mol\,L^{-1}}$ of a monovalent salt. The resulting screening Debye length for water at $20\,°\mathrm{C}$ is $\lambda_D = 173.1\,\mathrm{nm}$. The surface charge density imposed as boundary condition at the NP surface is calculated with $\sigma = \epsilon_0 \epsilon_r\, \psi_0\, (1 + a/\lambda)/a$ [135].

Acknowledgment: The authors appreciate the support for this project by the North-German Supercomputing Alliance (HLRN) as well as by the Lower Saxony Ministry of Science and Culture within the PhD program "Self-organizing multifunctional structures for adaptive high performance light-weight constructions". The framework of this coordinated program is the "Campus for Functional Materials and Functional Structures" (https://www. campus-fws.de/de/) which is an institution of the Clausthal University of Technology (TUC) in collaboration with the Deutsches Zentrum für Luft- und Raumfahrt (DLR, German Aerospace Center) in Braunschweig and the Bundesanstalt für Materialforschung und -prüfung (BAM, Federal Institute for Material Testing) in Berlin, completed by the Technical University of Braunschweig (TU BS).

6 Effect of an electric field on the formation of nanoparticulate clusters

This chapter was published in the form of a full paper in the Journal of Aerosol Science

Hector Rusinque, Elena Fedianina, Alfred P. Weber, & Gunther Brenner. (2018).
Numerical study of the controlled electrodeposition of charged nanoparticles
in an electric field
Journal of Aerosol Science, 129, 28-39.
DOI: 10.1016/J.JAEROSCI.2018.11.005 .

6.1 Zusammenfassung

Die Selbstassemblierung von Nanopartikeln zu gröSSeren Strukturen kann eine leistungsfähige Technik zur Einstellung der elektrischen und optischen Eigenschaften der erzeugten Strukturen sein, die verschiedene Anwendungen in Bereichen wie der Mikroelektronik findet. Diese spontane Organisation erfolgt durch direkte spezifische Wechselwirkungen, z. B. van der Waals-Kräfte, oder indirekt durch ein äuSSeres Feld. Die besonderen Eigenschaften der resultierenden Struktur lassen sich durch die Wechselwirkungen zwischen den selbstorganisierten Teilchen erklären, die durch ihre elektronischen, magnetischen und optischen Eigenschaften beeinflusst werden.[143,144] Diese intermolekularen Kräfte halten die Selbstassemblierung zu einer stabilen Struktur zusammen. Darüber hinaus können durch das Sintern der Partikel-Cluster neue Schichten von Nanopartikeln auf der gesinterten Struktur abgeschieden werden, um komplexe 3D-Strukturen wie bei der additiven Fertigung zu bilden.[145]

Im vorliegenden Kapitel werden die Bewegung und die Elektroabscheidung von Nanopartikeln unter dem Einfluss eines elektrischen Feldes numerisch untersucht. Nach der Injektion der Partikel in die Abscheidungskammer (ein Elektrodenaufbau) bewegen sich diese spontan von einem Bereich mit hohem elektrischem Potenzial, der von Brownscher (Zufalls-)Bewegung dominiert wird, in einen Bereich mit niedrigem Potenzial, in dem ihre Trajektorien durch die elektrische Kraft bestimmt/kontrolliert werden, bis sie sich auf

---

[143] Zhihong Nie et al. *Nat. Nanotechnol.*, **5**: 15–25, 2010.
[144] C. Stephenson & A. Hubler. *Sci. Rep.*, **5**: 15044, 2015.
[145] Kiwoong Lee et al. *Nanotechnology*, **28**: 475302, 2017.

der Oberfläche des Substrats (der Elektrode mit dem niedrigsten Potenzial) zusammensetzen. Die Simulationsergebnisse sind in guter Übereinstimmung mit den numerischen und experimentellen Messdaten von Choi et al. 2015.

Aus den erhaltenen Ergebnissen wurde festgestellt, dass die von den abgeschiedenen Nanopartikeln hinterlassene Musterbreite indirekt mit der elektrischen Kraft unter isothermen Bedingungen (konstante thermische Bewegung) korreliert. Eine Verringerung der Musterbreite wird daher hauptsächlich durch eine Erhöhung der GröSSe der elektrischen Kraft erreicht, was entweder durch eine Erhöhung der Anzahl der Ladungen pro einfallendem Partikel oder durch eine Erhöhung der Potenzialdifferenz oder schlieSSlich durch eine Verringerung des Elektrodenspalts erfolgen kann. Weitere Modifikationen an der Geometrie des Elektrodenaufbaus zeigen einen geringen Einfluss auf die Musterbreite, da diese nur die Form des elektrischen Feldes beeinflussen und nicht dessen Stärke, die direkt mit der GröSSe der elektrischen Kraft zusammenhängt. Hier wird eine Verringerung der Musterbreite beobachtet (d.h. eine Verstärkung des Fokussierungseffekts der Elektroabscheidung), wenn die Modifikationen der Geometrie zu einer engeren Konvergenz der Stromlinien des Feldes auf dem Substrat führten. Dies ist z. B. der Fall, wenn die Dicke der Maske erhöht oder der Abstand zwischen den Öffnungen der Maske verringert wird.

6.2 Abstract

A numerical investigation of the effect of sensitive parameters on the controlled electrodeposition of charged nanoparticles driven by an electric field is conducted. By applying a potential difference between an arrangement of electrodes, an electric field is generated, in which charged nanoparticles are transported through a mask and finally deposited on a substrate, a technique first described and applied by Choi et al. Using this technique, sharply delimited structures of deposited particles can be printed. A series of simulations are carried out taking into account the variation of different parameters such as the geometry of the electrode arrangement as well as the size and charge of the particles. The numerical results are verified with experimental and numerical data from Choi et al. It is determined how the considered parameters affect the deposition of the nanoparticles with respect to the sharpness of the obtained deposits. Here, the investigated spherical particles showed an inertia-free behavior within the considered diameters from 5 to $30\,\mathrm{nm}$. The correlation of the thermal fluctuations with the electric force is quantitatively analyzed, as well as its impact on the width of the pattern of deposited nanoparticles.

6.3 Introduction

The general driving force of isothermal-isobaric processes is the minimizing of Gibbs free energy.[146] Under these conditions of constant temperature and pressure, an ensemble of nanoparticles, seeking energy minima, organizes spontaneously into ordered, larger structures in a lower-energy, more stable state. As a consequence of being thermodynamically more stable, self-assembled structures can exhibit properties that differ from those shown by their individual components.

The self-assembling of nanoparticles to form larger structures can be a powerful technique for adjusting the electrical and optical characteristics of the produced structures, finding various applications in areas such as microelectronics.[147,148] This spontaneous organization occurs as a result of direct specific interactions, e.g. van der Waals forces, or indirectly through an external field. The particular properties of the resulting structure can be explained by the interactions between self-assembled particles affected by their electronic, magnetic and optical properties[143,144] These intermolecular forces hold the self-assembly into a stable structure together. Furthermore, by sintering the particle cluster, new layers of nanoparticles can be deposited on the sintered structure to form complex 3D structures as in additive manufacturing.[145]

Different self-assembly techniques have been developed based on the above-mentioned principles. For instance, using a self-assembly process driven by capillary interactions, 2D-arrays consisting of an orderly arrangement of monodisperse polymethylmethacrylate microspheres were formed.[149] In another study, nanoparticles gather spontaneously with the neighboring particles in a liquid medium by binding them using ligands attached to their surfaces.[150] Surface-grafted DNA molecules were used as ligands that drive the self-assembly process.[151]

The self-assembly process of a nanoparticle system can also be induced by directed self-assembly techniques (DSA). The most common directors are external fields such as electric and magnetic fields, whose effect on charged particles consists in driving their movement and aligning them by the induced interactions. However, this is only the case, if the external force is strong enough to overcome Brownian motion.[152] By applying a potential difference between two electrodes an electric field can be generated and used to precipitate charged nanoparticles on one of the electrodes, the substrate. The geometry of the second electrode can be adjusted to force the field lines to focus on a specific surface area of the substrate. This lens effect can be achieved by using a mask with micrometer scale opening sizes as an electrode, conferring on such a electrode setup the ability to print micropatterns of nanoparticles onto the substrate through controlled electrodeposition.[153,154] This technique, presented by Choi et al. 2015, enables the fabrication of hierarchical functional materials with complex structures opening up application opportunities in fields ranging from catalysis, optics, photonics, sensor technology and separation processes to electrochemical devices.[154–156] As an example, the controlled design of the pore structure of porous materials allows the optimization of diffusive transport through these media, enhancing catalytic and separation processes.[9–11,155]

---

[146] Marek Grzelczak et al. *ACS Nano*, **4**: 3591–3605, 2010.
[147] David Lyon & Alfred Hubler. *IEEE T. Dielect. El. In.*, **20**: 1467–1471, 2013.
[148] Alfred W. Hübler & Onyeama Osuagwu. *Complexity*, **15**: , 2010.
[149] N D Denkov et al. *Langmuir*, **8**: 3183–3190, 1992.
[150] Alexander Böker et al. *Soft Matter*, **3**: 1231, 2007.
[151] W. Benjamin Rogers et al. *Nat. Rev. Mater.*, **1**: 16008, 2016.
[152] Slavko Kralj & Darko Makovec. *ACS Nano*, **9**: 9700–9707, 2015.

In this paper, after verifying the implementation of the model with experimental and numerical data from Choi et al.[154], selected parameters affecting the controlled deposition of charged nanoparticles in an electric field are numerically studied, specifically by calculating the pattern width W_c. The parameters taken into account for the study are the electric field, which is changed in magnitude and shape by modifying the geometry of the electrode setup and the potential difference, as well as the size (5-30 nm) and charge of the metallic nanoparticles. Different metals are as well considered. However, the motion of the particles showed to be material-independent. Based on the simulation results, a dimensionless analysis is performed, in order to explain the inertia-free behavior shown by the particles. Finally, building on the gained understanding of the nanoparticle motion, a dimensionless number and a fitting function are proposed, which can be used to correlate the width of the printed pattern with the electric force applied.

6.4 Modeling and numerical approach

An electrode arrangement inducing a lens effect in the electric field lines is considered. Such a setup was first presented by Choi et al. in different previous studies.[154,157–159] A representative scheme of the electrode setup with given dimensions is shown in Figure 6.1. The motion of nanoparticles in an electric field can be described by the Langevin equation. This equation is derived from Newton's second law of motion, whereby a stochastic

---

[153] Hoseop Choi & Mansoo Choi. *US Patent*, US9321633B2, 2014.

[154] Hoseop Choi et al. *J. Aerosol Sci.*, **88**: 90–97, 2015.

[155] Cedric Boissiere et al. *J. Adv. Mater.*, **23**: 599–623, 2011.

[156] Nathan E Motl et al. *J. Mater. Chem. A*, **1**: 5193–5202, 2013.

[9] Robert Güttel & Thomas Turek. *Energy Technol.*, **4**: 44–54, 2016.

[10] Li Chen et al. *Chem. Eng. J.*, **349**: 428–437, 2018.

[11] Jian Yin et al. *J. Mater. Chem. A*, **6**: 8441–8448, 2018.

[157] Sukbeom You & Mansoo Choi. *J. Aerosol Sci.*, **38**: 1140–1149, 2007.

[158] Sukbeom You et al. *Small*, **6**: 2146–2152, 2010.

[159] Hyoungchul Kim et al. *Nat. Nanotechnol.*, **1**: 117–121, 2006.

term, known as white noise, models the Brownian motion of the nanoparticles after mathematical integration.

The interactions between the air molecules of the medium and the nanoparticles are represented in the equation by two terms describing thermal motion and drag. The balance between these two forces is known as the Einstein relation and is described by the fluctuation-dissipation theorem. Here, a particle moving through a medium experiences drag leading to dissipation of kinetic energy. The surrounding molecules respond to this perturbation by turning the dissipated energy into thermal motion (the corresponding fluctuation).

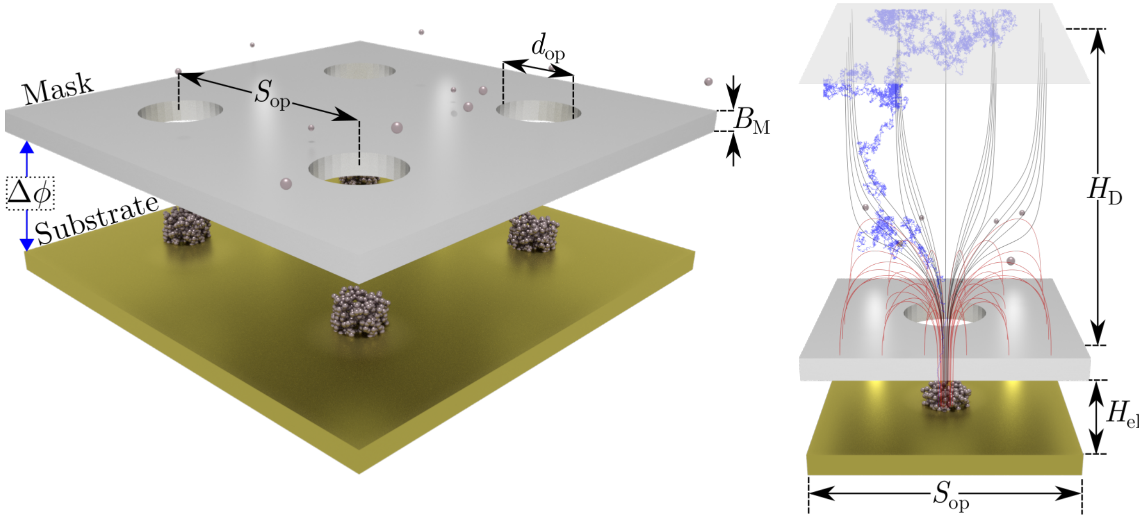

Figure 6.1: Electrode arrangement with potential difference and dimensions. Here, d_{op} stands for the opening diameter of the mask, S_{op} for the spacing between openings, B_{M} for the mask thickness, H_{D} for the distance between the upper electrode (the "ceiling") and the mask electrode in the middle, and H_{el} for the distance between the mask and substrate electrodes (in the following referred as electrode gap). The same potential difference between the mask and the substrate $(\Delta\phi)$ is applied between the ceiling and the substrate, so that there is no difference in potential between the ceiling and the mask.

The equation of motion with the considered forces is shown below

$$m\dot{\mathbf{v}} = \mathbf{F}_{\gamma} + \mathbf{F_{th}} + \mathbf{F}_{\text{el}} + \mathbf{F_{vdW}} \tag{6.1}$$

The following equations describe the forces acting on a particle

- Drag force $\mathbf{F}_{\gamma} = -\gamma_s \mathbf{v(t)}$,

  where γ_s is the Stokes drag coefficient given by $\gamma_s = 12\pi\,\eta\,d_p$. Here, d_p stands for the particle size, η for the dynamic viscosity, $-\mathbf{v(t)}$ for the flow velocity relative to the moving sphere assuming stationary air.

- Electric force $\mathbf{F}_{\text{el}} = q\mathbf{E(x)}$,

  where q is the charge of a nanoparticle and $\mathbf{E(x)}$ is the position-dependent electric field that can be described by $\mathbf{E}(\mathbf{x}) = -\nabla\phi(\mathbf{x})$.

- Van der Waals force

$$\mathbf{F_{vdW}} = \frac{A_{ps} d_p^3}{12\left(D_{ps} - d_p/2\right)^2 \left(D_{ps} + d_p/2\right)^2}\mathbf{n} + \frac{A_{pp} d_p^6}{6\left(D_{pp} - d_p\right)^2 D_{pp}^3 \left(D_{pp} + d_p\right)^2}\mathbf{r} \tag{6.2}$$

  where A is the Hamaker constant, D_{ps} is the distance between incoming particles and the substrate surface, D_{pp} is the distance between incoming particles and deposited particles, and $\mathbf{n}$ as well as $\mathbf{r}$ their respective normal vectors.

- Thermal driving force $\mathbf{F_{th}} = \sqrt{2\gamma_s\, k_\mathrm{B} T/C_c}\mathbf{W}(\mathbf{t})$.
  where k_B is the Boltzmann constant, T is the temperature and $\mathbf{W}(\mathbf{t})$ is Gaussian white noise $W_i(t)$. The integral of white noise describes Brownian motion (also known as Wiener process). Numerically, this is realized by generating a normally distributed random number for each coordinate with zero mean $\mu = 0$ and variance $\sigma^2 = 1$.[24,25]

The equation of motion is numerically integrated by the leapfrog method.[68] The leapfrog integration is a second-order method. Though, it requires the same number of function evaluations per step as the first order Euler scheme. The leapfrog method is more stable for oscillatory motion in contrast to Euler integration. As no motion occurs in the solid phase, nanoparticles are not allowed to cross solid boundaries. Therefore, a no-flux boundary condition is implemented for the solid elements of the system. A simple boundary condition such as diffusive reflection serves this purpose. In contrast to the diffusive boundary condition for the solid phase, at the lateral boundaries of the computational domain, periodic boundary conditions are used. It is assumed that the solid surface of the substrate is the only surface from which the particles are not reflected. Instead, they stick to the substrate surface on a given location that is stored as the final position of the particle. This stick condition implies the assumption that the momentum associated with all collisions between the incoming particles and the substrate surface is not high enough to lead to reflection of the particles from the surface. Out of the final positions of the centers of all deposited nanoparticles, the resulting spatial distribution on the substrate surface and its related width are computed. The computation of the electric field is based on the electrostatic Maxwell equations using the commercial software COMSOL Multiphysics. A file with the computed electric field over the discretized space is given as input to the Langevin solver, where the electric field can be evaluated in any point of the computational domain through multilinear interpolation. For instance, the electric field of

---

[24] H G SCHUSTER & WOLFAM JUST. *Deterministic Chaos*. Wiley, 1994.

[25] GIORGIO VOLPE & GIOVANNI VOLPE. *Am. J. Phys.*, **81**: 224–230, 2013.

[68] GUIHUA ZHANG & TAMAR SCHLICK. *Mol. Phys.*, **84**: 1077–1098, 1995.

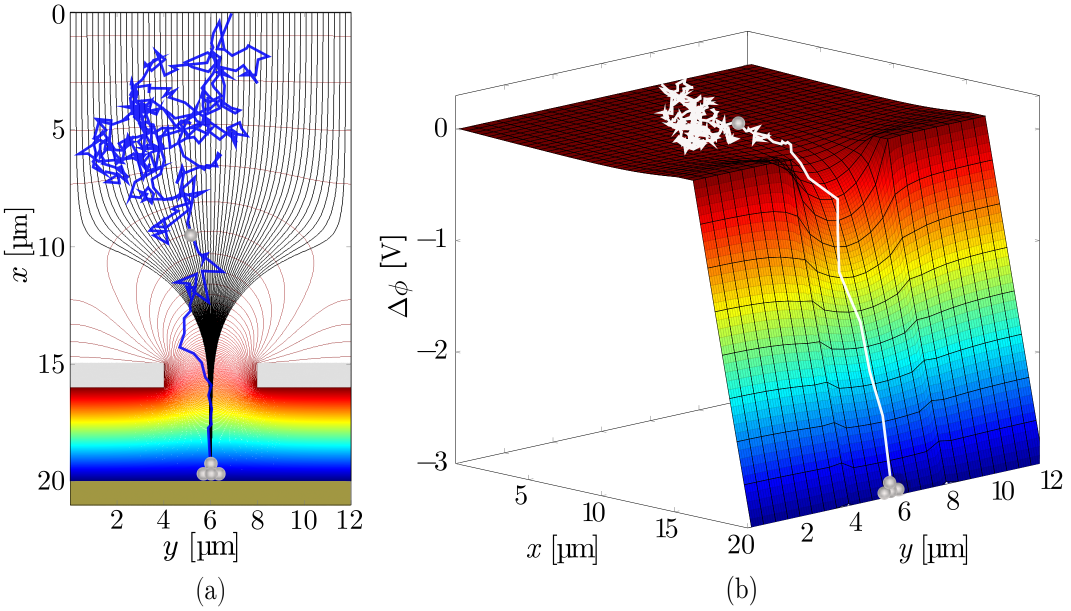

Figure 6.2: a) The electric field lines (in black) emerging from the ceiling of the deposition chamber run from high to low potential. The equipotential lines (perpendicular to the field lines) are red for high potential and turn yellow, green and blue as the potential goes down.
b) Alternatively, the equipotential lines can be seen as a potential surface on which the nanoparticles spontaneously move downhill transforming potential energy into kinetic energy. This example is taken from the results presented in the verification case using a slit-shaped mask opening (see Sec. 6.5.1).

the verification case presented in Section 6.5.1, and the electric potential levels of a given xy-plane are shown in Figure 6.2.

6.5 Results and discussion

In the following, computational results of the nanoparticle deposition driven by an electric field are presented. Sensitive parameters affecting the particle motion are varied to evaluate their effect on the electrodeposition regarding the pattern width. In the scope of this work, the deposit width W_c is given as a fraction of the mask opening size d_op. The length fraction obtained $W_\mathrm{c}/d_\mathrm{op}$ can be interpreted as a focusing strength associated with the lens effect of the electrode arrangement. The Full Width at Half Maximum (FWHM) of the fitted Gaussian distributions was chosen as a characteristic length to represent the pattern width (see Figure 6.3). All the length values related to the geometry of the deposition chamber are given in terms of opening diameters (d_op). The deposition occurs at a temperature of $298.15\,\mathrm{K}$.

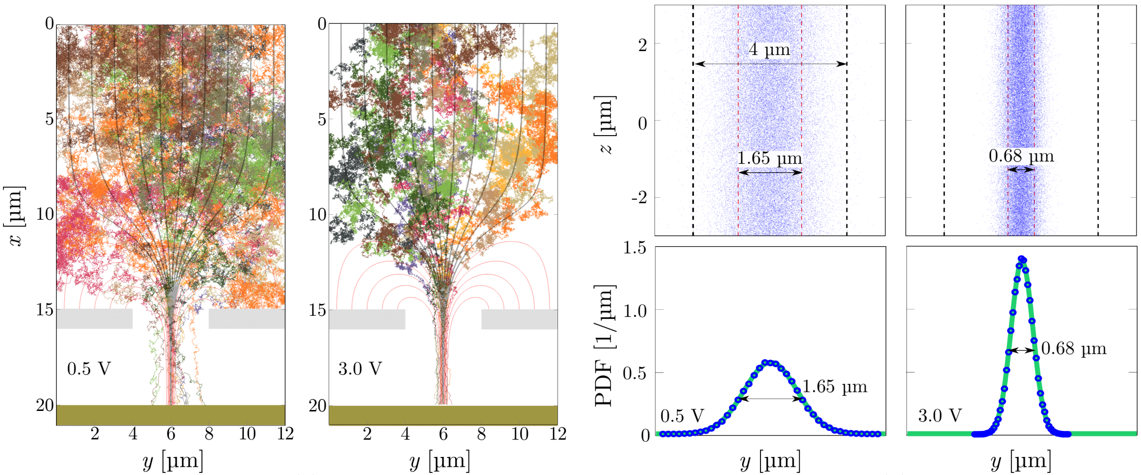

(a) (b)

Figure 6.3: a) The trajectories of eleven nanoparticles are shown as well as the electric field lines between the electrodes for the geometry used in the verification case (see Section 6.5.1) at a potential difference of 0.5 and $3\,\mathrm{V}$, respectively, for an opening diameter of $d_{\mathrm{op}} = 4\,\mu\mathrm{m}$.
b) The final positions of the deposited nanoparticles are shown above. The Gaussian-shaped curves represent the spatial distributions of the deposited nanoparticles in the form of a probability density function (PDF). The green lines are the Gaussian functions fitted to the simulation results represented by the blue points.

6.5.1 Verification

An in-house solver is used to solve the Langevin equation. As verification of the model implementation, the results are compared with the experimental data of Choi et al. 2015. The simulations are carried out using a stencil mask with a slit-shaped opening. The size of the slit (d_{op}) is $4\,\mu\mathrm{m}$ as shown in Figures 6.3 and 6.4. An electrical potential of $-600\,\mathrm{V}$ is applied to the substrate electrode, while a potential is applied to the ceiling and mask electrodes at a higher energy level, so that the desired difference is obtained. In contrast to the simulations of Choi et al. 2015, where the trajectories of 150 nanoparticles were calculated, in this study the motion of $100\,000$ nanoparticles is computed. The impact of the number of particles can be observed from the smoothness of the resulting Gaussian distribution of all particle centers on the printed pattern, as shown in Figure 6.3. In addition, Gaussian-shaped deposits are reproduced on the surface of the substrate in order to evaluate the influence of the 3D structures on the electric field. The structure under consideration is viewed as a continuum. The formation of metal oxides, altering the conductivity of the material, is neglected, which in practice can be achieved by using an inert medium such as molecular nitrogen instead of air. Finally, the height of the deposit H_{c} shown in Figure 6.4 is varied.

The simulation results (Figures 6.5a and 6.5b) are in good agreement with the results of Choi et al. The electric field lines converge towards the Gaussian-shaped structure, which

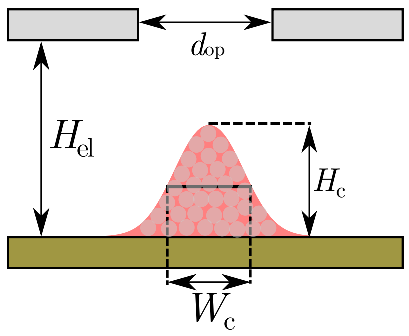

Figure 6.4: Height of the Gaussian-shaped structure H_{c} reconstructed on the surface of the substrate and opening size d_{op}.

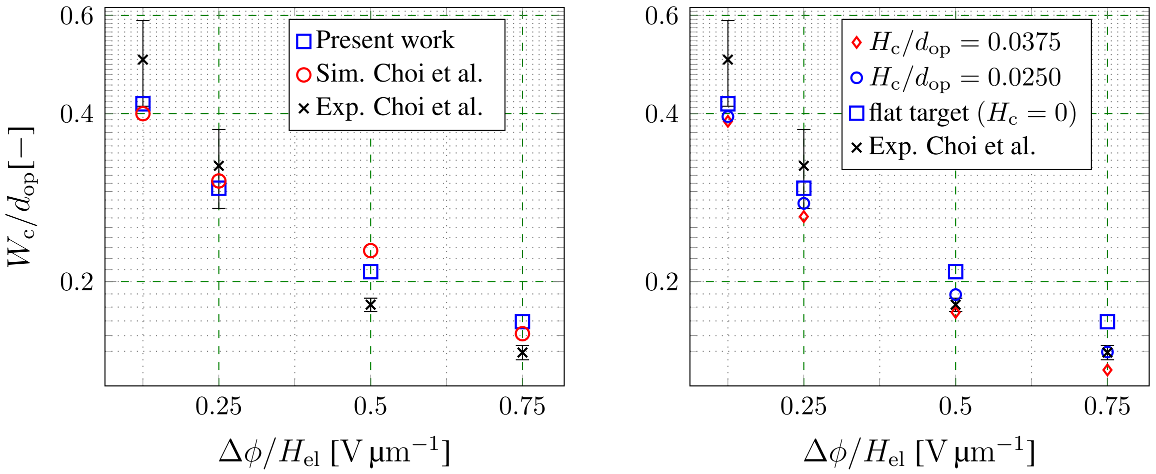

(a) Flat substrate

(b) Effect of H_{c}

Figure 6.5: a & b) Effect of the variation of the potential difference on the focusing effect for a given electrode gap H_{el}. b) Effect of the deposited nanoparticles forming 3D structures with two different heights $H_c/d_{\mathrm{op}} = 0.0250$ and 0.0375 . The results are compared with the experimental and simulation results of Choi et al.[154]

leads to an enhanced focusing effect. This is a consequence of two connected conductors (Gaussian-shaped 3D structure and substrate), which have the same electric potential in equilibrium. However, the electric charge density on the surface of the 3D structures is higher, as they have a smaller surface to distribute the charge. Here the equilibrium assumption is made, which means that the scale of the deposition time is sufficiently large compared to the time the charges take to move within the metallic medium until equilibrium is reached. The enhanced focusing effect due to the shape of the field lines is consistent with the theory of electric fields[160] and with the study by Lee et al. 2017, where an enhanced convergence of the field lines on the printed clusters can be observed.[145]

In the next sections, all the simulations will be referred to the electrode arrangement shown in Figure 6.1 using the values given in Table 6.1. The dimensions of the com-

---

[160] I.S. GRANT & W.R. PHILLIPS. *Electromagnetism*. Manchester Physics Series Wiley, 2013.

Table 6.1: Dimensions for the electrode arrangement considered in the following simulations. All lengths are given in multiples of d_{op}.

Distance	**Length**$/d_{\mathrm{op}}$ $[-]$
H_{D}	3.75
B_{M}	0.25
H_{el}	1.00
S_{op}	3.00

putational domain for the base case are $(H_x/d_{\mathrm{op}})\,\mathrm{X}\;(W_y/d_{\mathrm{op}})\,\mathrm{X}\,(D_z/d_{\mathrm{op}}) = 5\,\mathrm{X}\,3\,\mathrm{X}\,3$ (height, width and depth, respectively). A diameter was discretized by 40 cells.

6.5.2 Effect of size and charge of the nanoparticles

The effect of the size and charge of the nanoparticles is studied by varying their electric charge from 1 to 4 elementary charges and their diameter from $d_{\mathrm{p}} = 5$, 10, 20, to $30\,\mathrm{nm}$. The results in Figure 6.6 imply that the electric charge is the parameter that most influences the deposition of nanoparticles as it directly affects the magnitude of the electric force driving the deposition. Due to the similar correlation of the charge and the potential difference with the electrical force, this influence is explained in more detail below when the effect of the potential difference is discussed.

Within the investigated size range of the particles, no influence on the deposition is observed from the results. This can be explained by the fact that the weaker Brownian motion associated to the larger particles is compensated with the longer deposition time. In other words, the larger particles subject to smaller fluctuations in their movement have also more time to diffuse or spread leading to an increase in pattern width, while the deposition time of the smaller particles is shorter but their fluctuations are stronger also leading to an increase in deposit width. An extended discussion about this size-independent behavior is conducted in Section 6.5.5.

Material-Dependency The material of the nanoparticles was also varied. Nanoparticles made out of copper, silver, and iron with Hamaker constants ranging from 20 to 50×10^{-20} J were considered and evaluated in the simulations. Here, the motion of the particles showed to be material-independent. This can be explained by the fact, that the only material-dependent forces acting on the nanoparticles, the Van der Waals forces, are short-range forces in comparison to the size of the particles and only influence the motion of the nearest particles.[161] As a result, the pattern width is not affected by the choice

---

[161] M.S. SETHI & M. SATAKE. *Chemical Bonding*. Discovery Publishing House, 2010.

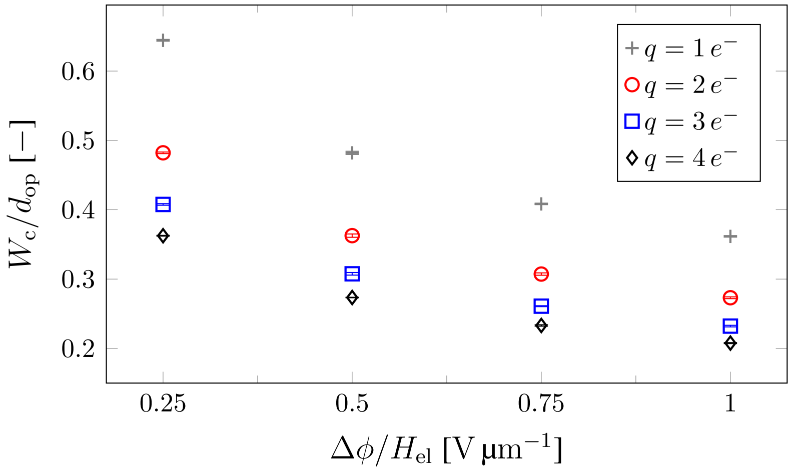

Figure 6.6: Effect of the variation of charge and size of the nanoparticles on the pattern width. The potential difference per electrode gap was varied between 0.25 and $1\,\mathrm{V\,\mu m^{-1}}$.

of material of the metallic nanoparticles. Thus, the influence of the material cannot be observed from the results in Figure 6.6, since these simply overlay each other.

6.5.3 Effect of the electric field: Variation of the potential difference

As shown in figure 6.6, the focusing effect increases with increasing potential difference $\Delta\phi$ for a given electrode gap H_{el}. In accordance with the mathematical model used to describe the electric forces, an increase in potential difference (with constant H_{el}) of the same magnitude as an increase in electric charge will cause the same enhancing effect on the electrostatic forces and thus on the focusing effect. Though, there is an upper limit to the increase of potential difference given by the electrical breakdown of air, which is normally an excellent insulator but when stressed by a sufficiently high electric field strength of about $3\,\mathrm{V/\mu m}$ [162] can begin to break down, becoming partially conductive.

6.5.4 Effect of the electric field: Changes due to geometry modifications

Geometric parameters are considered, whose variation leads to a change in shape and magnitude of the electric field lines. The modified dimensions are the electrode gap H_{el}, the spacing between mask openings S_{op}, the mask thickness B_{M}, and the shape of the mask opening including its cross section.

Electrode gap (H_{el}) Here, two cases are considered. For the first case, the electrode gap H_{el} is increased leaving the potential difference $\Delta\phi$ unchanged, which leads to a decrease in the field strength. This impacts negatively the focusing effect of the system,

---

[162] J.S. Rigden. *Macmillan Encyclopedia of Physics: A-D*. Simon & Schuster Macmillan, 1996.

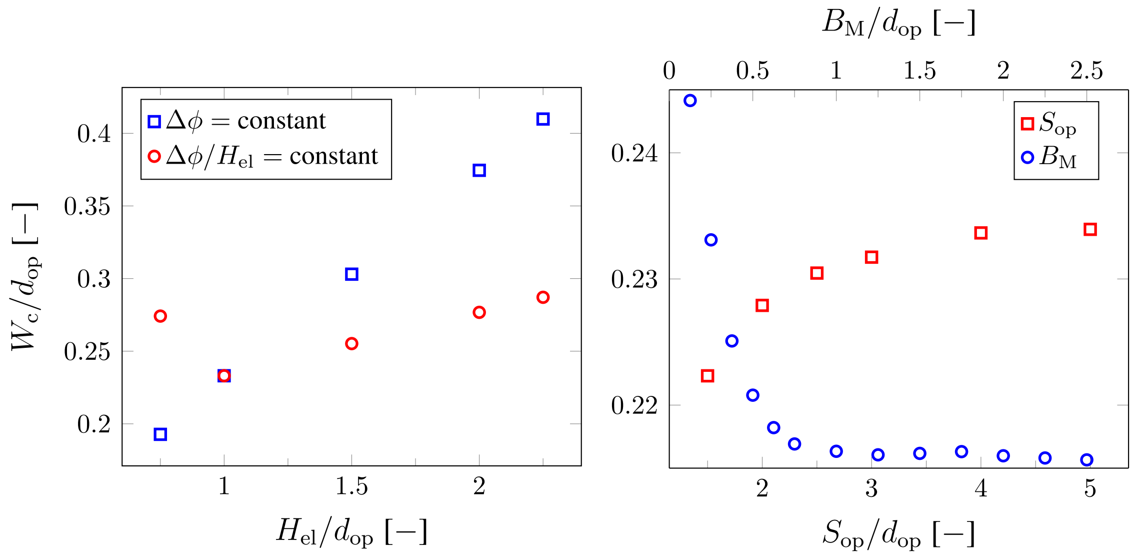

(a) Electrode gap

(b) Spacing and mask thickness

Figure 6.7: a) Effect of varying the spacing between openings and the mask thickness on the pattern width. A potential difference per electrode gap of $\Delta\phi/H_{\text{el}} = 0.75\,\text{V}\,\mu\text{m}^{-1}$ was applied for these two simulation cases. b) Effect of the electrode gap on the pattern width.

resulting in an increase of the pattern width (see Figure 6.7a). The field strength is set at $\frac{\Delta\phi}{d_{\text{op}}} = 0.75\,\text{V}\,\mu\text{m}^{-1}$.

In the second case, the strength of the electric field is kept constant by maintaining the ratio of the potential difference to the distance between electrodes unchanged at $\frac{\Delta\phi}{H_{\text{el}}} = 0.75\,\text{V}\,\mu\text{m}^{-1}$, so that only the effect of the geometry change is recorded in the simulations. In the latter case, the results show an optimal electrode gap at which the pattern width is minimized around $H_{\text{el}} = d_{\text{op}}$.

Mask thickness (B_{M}) Increasing the mask thickness shows a slightly positive effect on the pattern width up to around $B_{\text{M}}/d_{\text{op}} = 3$. From this value the increase in thickness does not alter the focusing effect. The slight changes in pattern width produced by changing the geometry of the mask can be explained by the fact that the field lines show a slightly different convergence on the substrate for a given mask geometry.

Spacing between openings (S_{op}) The spacing between openings was varied, leaving the diameter of the circular opening constant. The simulation results are shown in Figure 6.7b. From this, it can be concluded that increasing the spacing between openings has a slightly negative impact on the focusing effect due to the changes in the convergence of the field lines.

Table 6.2: Considered shapes of the mask openings, trough which the nanoparticles move from the upper to the lower section of the deposition chamber at $\Delta\phi/H_{\mathrm{el}} = 0.75\,\mathrm{V\,\mu m^{-1}}$. a,b and c show the cross sections of the openings evaluated in the simulations (see Fig. 6.8).

Shape of the Mask Opening		Pattern Width [d_{op}]
Square	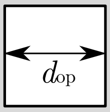	0.248
Rounded square	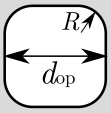	0.245
Circle (a)	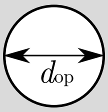	0.233
Funnel (b)	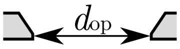	0.240
Inverted funnel (c)	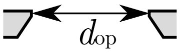	0.243

Opening geometry A circular and a squared opening as well as a rounded square are considered. The latter was generated by rounding the angles of a $4\,\mathrm{\mu m}$ square to arcs with a radius (R) of $1\,\mathrm{\mu m}$. Furthermore, simulations are carried out with different cross sections of the circular opening at $\Delta\phi/H_{\mathrm{el}} = 0.75\,\mathrm{V\,\mu m^{-1}}$. The simulation results can be seen in Table 6.2.

The results show that the corners of the squared opening and the cross section geometry do not considerably affect the focusing effect. The impact of these geometry variations on the field lines is plotted in Figure 6.8. From this Figure, it can be concluded that the field lines emerging from the ceiling of the deposition chamber and, to a significantly lesser degree, those coming from the upper side of the mask make a dominant contribution to the particle motion in the lower section of the deposition chamber, while the field lines emerging from the faces of the mask opening do not significantly alter the motion of the nanoparticles.

6.5.5 Dimensional analysis

The size-independent behavior shown by the particle dynamics implies that the motion is also mass-independent, meaning that the inertia of the metallic nanoparticles is negli-

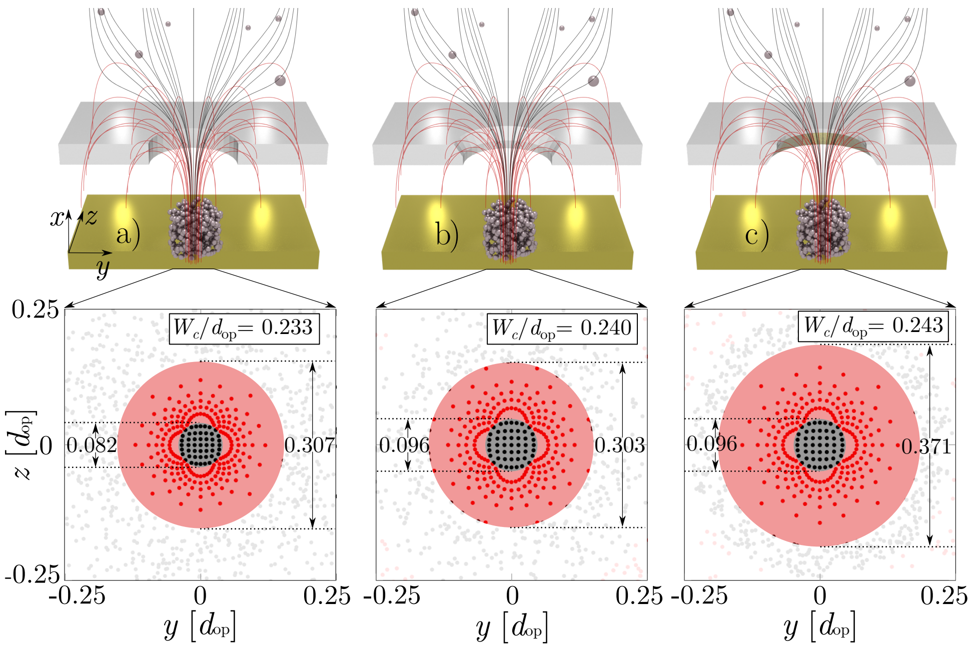

Figure 6.8: Convergence of the field lines onto the substrate. Field lines emerging from the upper face of the mask are in red, whereas the black field lines originate from the ceiling of the deposition chamber. The pattern in the figure represents the points, where selected electric field lines touch the substrate. Here, the red and black contact points correspond to the red and black field lines, respectively. The brighter points outside the red circle correspond to field lines originating from the faces of the mask opening. The pattern width per opening diameter (W_c/d_{op}) is shown for each case.

gible in the time scales and within the particle sizes investigated. This can be explained by the deposition times, which are much longer than the characteristic relaxation time of a Brownian particle (in this work ranging from 0.6 to $28\,\mathrm{ns}$), given by the following equation[65]

$$\tau_{\mathrm{B}} = \frac{m}{\gamma} \approx \frac{m}{12\pi\eta d_p}. \tag{6.3}$$

The inertia-free behavior of the nanoparticles can be analyzed by calculating the Péclet number as a function of the x-direction $\mathrm{Pe}(x)$ for two particles sizes ($d_{\mathrm{p}} = 5$ and $30\,\mathrm{nm}$) at two potential differences per electrode gap ($\Delta\phi/H_{\mathrm{el}} = 0.125$ and $0.75\,\mathrm{V\,\mu m^{-1}}$), applying the following definition for the Péclet number

$$\mathrm{Pe} = \frac{d_{\mathrm{op}}\, v_{\mathrm{Drift}}}{D_\infty} \equiv \frac{\text{Convection}}{\text{Diffusion}}, \tag{6.4}$$

where the drift velocity is given by the average velocity of the particle ensemble in the x-direction $\langle v_x \rangle$. Here, the x-direction is chosen since it is the main direction of the drift exerted by the electric field. For larger time scales of the electrodeposition in compari-

---

[65] Xin Bian et al. *Soft Matter*, **12**: 6331–6346, 2016.

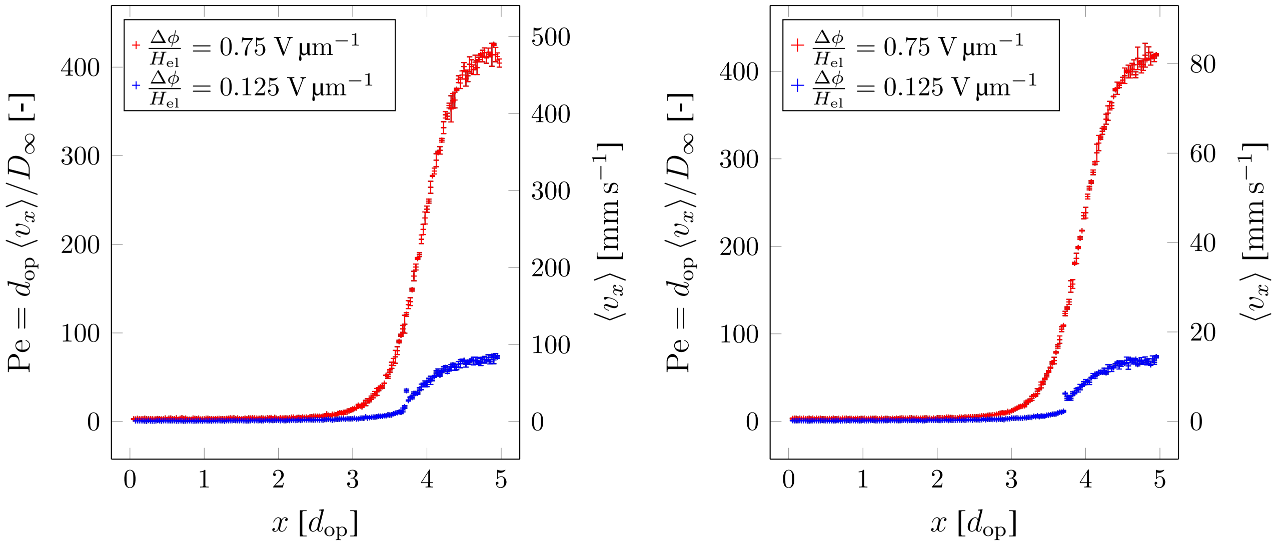

(a) NPs with $d_{\mathrm{p}} = 5\,\mathrm{nm}$

(b) NPs with $d_{\mathrm{p}} = 30\,\mathrm{nm}$

Figure 6.9: Péclet number (Pe) of the nanoparticles (left axis) and average velocity $\langle v_x\rangle$ (right axis) at two particle sizes and potential differences. The velocities are computed for an opening diameter $d_{\mathrm{op}} = 4\,\mathrm{\mu m}$ and an electrode gap $H_{\mathrm{el}} = 4\,\mathrm{\mu m}$. The particles were introduced into the deposition chamber at $x = 0$ and move randomly until they come close to the mask openings located at $x/d_{\mathrm{op}} = 3.75$ where the electrical potential drops sharply. As a result, the potential energy of the particles is abruptly converted to kinetic energy, leading to an abrupt increase of Pe.

son with the relaxation time, the diffusion coefficient can be calculated according to the Einstein relation[13,65]

$$D_\infty = \frac{k_{\mathrm{B}}T}{\gamma}. \tag{6.5}$$

As expected from the intertia-free motion of the nanoparticles, the change of size does not affect the Péclet number, which takes the same values for both particle sizes. Further, the calculated magnitude of the velocities (displayed in the right axis of Fig. 6.9) is in accordance with the explanation given in the previous discussion regarding the variation of particle size, which states that the weaker fluctuations of the larger particles do not lead to sharper deposits, since the slower deposition velocities will ultimately compensate for the resulting width by giving the particles more time to spread.

The $\mathrm{Pe}(x)$-curves for the lower potential difference (blue curves in Fig 6.9) show a discontinuity at $x/d_{\mathrm{op}} = 3.75$ when the nanoparticles come too close to the edge of the opening at the upper face of the mask (e.g. at $x = 15\,\mathrm{\mu m}$ in Figures 6.2 and 6.3). At this x-location, the electric field shows an abrupt change in magnitude (see Figure 6.10) which causes the abrupt change in velocity and Péclet number. Although the electric field shows the same behavior for the potential difference of $0.75\,\mathrm{V\,\mu m^{-1}}$, the nanoparticles do not get that close to the edge, since they are earlier drawn into the mask hole as can be

---

[13] A. Einstein. *Ann. d. Phys.*, **322**: 549–560, 1905.

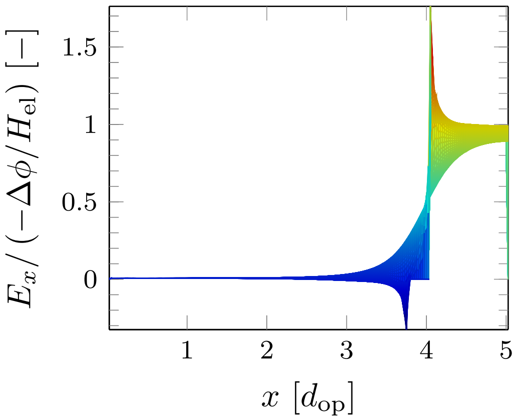

Figure 6.10: Normalized field strength E_x for a given xy-plane at $z = S_{\text{op}}/2$. As a result of the normalization, the normalized field strength is generally valid for any potential difference applied.

seen in Figure 6.3.

Based on the forces acting on the nanoparticles, three dimensionless numbers characterizing the particle motion are proposed and discussed in the following. The thermal driving force F_{th} is selected as a common numerator for the proposed numbers, since its associated fluctuations inversely correlate with the sharpness or width of the resulting deposits. Now, counteracting forces dampening the thermal fluctuations are set as denominator for each dimensionless number, namely the drag F_γ, the electric force F_{el}, and the inertia F_m, which can be thought of as a fictitious force.

$$\frac{F_{\text{th}}}{F_m} \equiv \Omega_m = \frac{k_B T}{m v_{\text{Drift}}^2} \tag{6.6}$$

$$\frac{F_{\text{th}}}{F_\gamma} \equiv \Omega_\gamma = \frac{k_B T}{\gamma \, v_{\text{Drift}} \, d_{\text{op}}} \tag{6.7}$$

$$\frac{F_{\text{th}}}{F_{\text{el}}} \equiv \Omega_{\text{el}} = \frac{k_{\text{B}} T / H_{\text{D}}}{q \left(-\Delta\phi / H_{\text{el}}\right)} \tag{6.8}$$

Under the given isothermal conditions, the magnitude of the thermal driving force does not change. This implies that the particle motion is influenced only by changes in the counteracting forces. An increase in these forces (in the denominator of the Ω numbers) induces a dampening effect of the fluctuations the particles undergo. The dampening of the fluctuations is reflected in a decrease in both the pattern width and the magnitude of the dimensionless numbers considered. This means that the width of the deposits correlates directly with the Ω numbers.

Let's take a look at each dimensionless number. Ω_m is the number that captures the most complete picture of particle motion as it contains the effects of thermal motion and the inertia represented by the term $m v_{\text{Drift}}^2$, which in turn contains the effects of the drag and

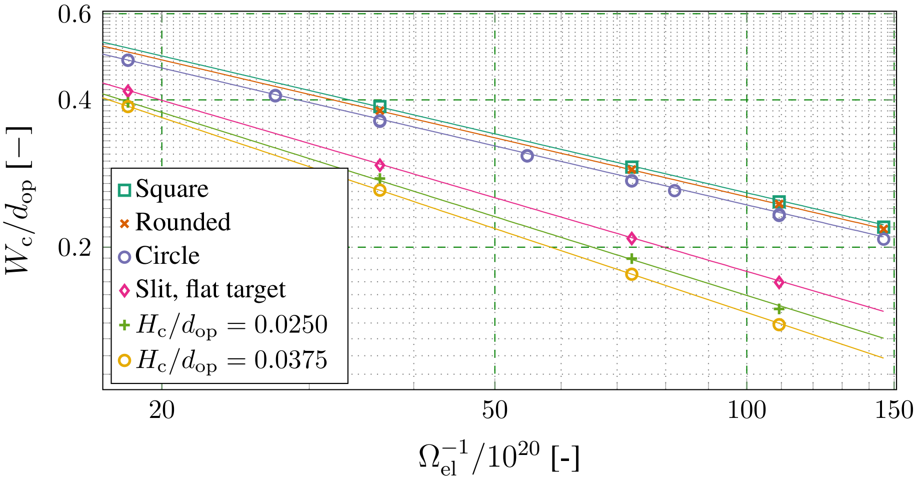

Figure 6.11: Pattern width as a function of the inversed dimensionless number Ω_{el}^{-1}, which under isothermal conditions can be viewed as a dimensionless electric force (W_c/d_{op} vs F_{el}). The solid lines represent the fitting function obtained for each case using the function proposed in Eq. 6.10.

the electric force associated with the drift velocity. Ω_γ is actually the reciprocal of the Péclet number, which can be obtained by rearranging its definition using Eq. 6.5 to

$$\Omega_\gamma = \frac{D_\infty}{v_{\mathrm{Drift}}\, d_{\mathrm{op}}} = \mathrm{Pe}^{-1}. \tag{6.9}$$

As the inertia of the particles can be neglected, this number offers a general description of the particle motion capturing the dominant effects of the drag and electric force. Finally, Ω_{el} gives the most simple but still complete picture of the particle motion in the region of lower electric potential, where the dynamic of the particles is dominated by the electric force. Under the given isothermal conditions (constant thermal driving force), the reciprocal of this number Ω_{el}^{-1} can be thought of as a dimensionless electric force. From this, an indirect correlation of the width of the deposits with Ω_{el}^{-1} can be inferred, meaning that the pattern width will decrease by increasing the dimensionless electric force, as shown in Fig. 6.11, where the pattern width is plotted as a function of Ω_{el}^{-1} for the considered cases of different shapes of the mask opening. These cases have already been presented in Table 6.2 and in the verification case.

Now, a function fitting the results is proposed and plotted in Fig. 6.11. As the pattern width directly correlates with Ω_{el}, a power function is chosen in the form

$$\frac{W_c}{d_{\mathrm{op}}} = C_1\, \Omega_{el}^{C_2}. \tag{6.10}$$

Table 6.3: Coefficients of the power function for the cases studied.

Case	$C_1[-]$	$C_2[-]$
Square	1.63	0.40
Rounded	1.60	0.40
Circle	1.54	0.40
Slit, flat target	1.79	0.50
Slit, $H_\mathrm{c}/d_\mathrm{op} = 0.0250$	1.87	0.54
Slit, $H_\mathrm{c}/d_\mathrm{op} = 0.0375$	2.03	0.57

It should be noted that the factors C_1 and C_2 are also dimensionless and account for the geometry-dependency of the electric field. The latter explains the small changes in the factors of the fitting function from one geometric arrangement to another, as can be seen in Table 6.3. For instance, the factor C_1 takes different values for each opening geometry considered (squared, rounded and circular). The slope of the fitting lines (C_2), on the other hand, is not altered by these modifications of the opening geometry. In contrast, the C_2 factor showed to be sensitive to the changes in the geometry of the target, where a Gaussian-shaped 3D structure with various heights H_c was reproduced on the substrate surface. The influence of these 3D structures on the streamlines of the electric field led to an enhanced focusing effect, which results in greater logarithmic slopes C_2 with increasing structure height.

6.6 Conclusions

In the present study, the motion and electrodeposition of nanoparticles under the influence of an electric field were numerically examined. After injecting the particles into the deposition chamber (an electrode setup), these move spontaneously from a high potential region dominated by random motion to a low potential region where their trajectories are determined by the electric force until they assemble on the surface of the substrate (the electrode with the lowest potential). The simulation results are in good agreement with the numerical and experimental data of Choi et al. 2015.

From the obtained results it was found that the pattern width left behind by the deposited nanoparticles indirectly correlates with the electric force under isothermal conditions (constant thermal motion). Therefore, a reduction of the pattern width is achieved mainly by increasing the magnitude of the electric force, which can be done either by increasing the number of charges per incoming particle or by increasing the potential difference or finally by reducing the electrode gap. Further modifications to the geometry of the electrode setup showed a slight impact on the pattern width, as these only affect the shape of the electric field and not its strength, which is directly related to the magnitude of the electric force. Here, a reduction of the pattern width was observed when the modifications of the geometry led to a narrower convergence of the streamlines of the field on the substrate. This is the case, for example, when the thickness of the mask is increased or the distance between the openings of the mask is reduced.

Furthermore, it was concluded that the choice of material and particle size does not affect the deposition within the examined range. A different material will only locally influence the short-range interactions between the incoming particles and the deposited ones, which does not alter the obtained pattern width. With regard to the size, the weaker Brownian motion of the larger particles is compensated by the longer deposition time, resulting in equal trajectories and pattern widths.

In the final section, an expression for the pattern width as function of a dimensionless number was presented, which relates the pattern width to the ratio between electric and randomly fluctuating forces.

After having established a correlation between the dominant parameters examined and the pattern width, further numerical and experimental research will be done on determining their effect on the height of the structure.

6.7 Notation

d_{op}	µm	opening diameter
d_{p}	nm	particle diameter
H_{el}	µm	gap between mask and substrate
H_{D}	µm	gap between ceiling and mask
H_{c}	µm	height of the 3D-structure
B_{M}	µm	mask thickness
S_{op}	µm	spacing between opening centers
W_{c}	µm	pattern width
$\Delta\phi$	V	potential difference
H_x	µm	height of the computational domain
W_y	µm	width of the computational domain
D_z	µm	depth of the computational domain

Acknowledgment: The authors appreciate the support for this project by the North-German Supercomputing Alliance (HLRN) as well as by the Lower Saxony Ministry of Science and Culture within the PhD program "Self-organizing multifunctional structures for adaptive high performance light-weight constructions". The framework of this coordinated program is the "Campus for Functional Materials and Functional Structures" (https://www.campus-fws.de/de/) which is an institution of the Clausthal University of Technology (TUC) in collaboration with the Deutsches Zentrum für Luft- und Raumfahrt (DLR, German Aerospace Center) in Braunschweig and the Bundesanstalt für Materialforschung und -prüfung (BAM, Federal Institute for Material Testing) in Berlin, completed by the Technical University of Braunschweig (TU BS).

7 Final discussion and conclusions

This chapter discusses the formation of nanoparticulate clusters and how it can be affected by confinement (Chapter 3), mass transport (Chapter 4), pairwise interactions (Chapter 5) as well as external forces (Chapter 6). As the topics and findings addressed in Chapters 3 and 4 are needed to support the suggested formation mechanism and assumptions made in Chapter 5, a special focus is hereby set on the topic of formation of nanoparticulate clusters via evaporation.

As shown in Chapter 5, the formation of nanoparticulate clusters is a complex process that can involve different packing mechanisms leading to structured or unstructured arrangements. It was also shown, that the HCl retention in the porous structure of the forming cluster can be exploited to control the final pore size. This retention is caused by both, mass transport affected by hindered diffusion and the chemical capture of the HCl molecules due to the formation/crystallization of a metallic salt within the pores of the cluster.[12] The former was addressed in Chapter 4, where the pore-size induced, hindered diffusion of molecules was studied. In addition, it was discussed how the structural arrangement of clusters is affected by confinement. Cofinement effects are induced e.g. by the presence of external walls or an interface between two phases. This can play an important role in the formation of nanoparticulate clusters via evaporation of aerosols or emulsions, as it induces polycrystalline structures. Confining forces acting on the nanoparticles (NPs), such as wall normal forces, overcome the thermal forces that drive the Brownian motion of the NPs, resulting in the proliferation of multiple crystallization spots near the interface region. In Chapter 6, a similar effect was observed. Here, external electric forces acting on charged NPs were induced by the potential difference imposed between the electrodes of the deposition chamber. While the strength of the electric forces can be set by the magnitude of the potential difference, the thermal forces are set by controlling temperature. By setting an electric force stronger than the thermal forces, Brownian motion can be inhibited, resulting in sharper deposited clusters.

Regarding the forces involved during the drying of droplets containing NPs, two stages can be identified: A shrinking stage, followed by a consolidation stage. During the first one, colloidal repulsive forces are predominant, as they are responsible for stabilizing the dispersion. The effect of the capillary forces acting at the droplet surface is minimal and can be associated with the interface mechanical flexibility. In the second stage, as the droplet volume approaches the final cluster configuration, the droplet interface loses its spherical shape and water bridges begin to form between the NPs. This induces an attractive force due to capillary effects, which together with the dispersion (attractive) forces contribute to the consolidation of the cluster structure. The latter, however, is not expected to affect the final arrangement, as the sphere packing of NPs is imminently reaching the jammed state.[111]

---

[12] RAVI SHARMA et al. *Chem. Eng. J.*, **381**: 122512, 2020.

For high Péclet numbers, i.e. high evaporation rate and relatively slow NPs diffusivity, kinetic effects play a major role, meaning that the final structures differ from the energetically preferred equilibrium structures, e.g. face-centered cubic (fcc).

The receding droplet surface has a strong effect on the outer shell of the clusters, where the NPs are packed densely.[15] Depending on the mechanical properties of the outer shell, a jammed crust can be formed that determines the final size and shape of the cluster, which can be fully or partially hollow.[14] In some systems the crust collapses, resulting in a buckled geometry.[111] Note that a jammed state, in which the diffusivity of the NPs is severely hindered, can be reached earlier, i.e. at lower volume (packing) fractions Φ, depending on the surface roughness of the NPs or attractive interactions between them.[37]

At intermediate Péclet numbers, due to the higher mobility of the NPs, the outer crust does not prematurely reach a jammed state, but can further recede with the shrinking droplet. If the number of shells or NPs is large enough, the inner region of the cluster will remain unaffected by the compacting and ordering effect of the confining and show a bulk-like, disordered structure.[15]

At low Péclet numbers, i.e. low evaporation rate and relatively high NPs diffusivity, the cluster structure approaches the thermodynamically favored arrangement. Several parallels arise here between the mechanical process of packing hard spheres by compression and thermal colloidal systems. High down to low compression and evaporation rates lead to a disorderd equilibrium configuration known as random close packing (rcp), while significantly low rates allow to overcome the metastable rcp state and reach a highly ordered crystalline structure, which in the case of large clusters corresponds to the fcc configuration.[33,37,163,164] Both the compression and the evaporation-driven processes show surface-induced ordering when pressed by confining walls and similar final equilibrium configurations in bulk structures. Notice that evaporation-driven packings form rcp structures with slightly lower packing densities Φ since they are not constrained to reach a minimum number of contacts with their neighbors, as in the case of compression-driven packings.[37] This is due to the fact that the evaporation process is purely entropy-driven, i.e. constrained solely to gained vibrational degrees of freedom of the individual particles.[34,37,111,112,163]

---

[111] Junwei Wang et al. *Nat. Comm.*, **9**: , 2018.

[15] Michael P. Howard et al. *J. Chem. Phys.*, **149**: 094901, 2018.

[14] M. Mezhericher et al. *Chem. Eng. Sci.*, **66**: 884–896, 2011.

[37] Vasili Baranau et al. *Soft Matter*, **12**: 3991–4006, 2016.

[33] John F. Brady. *J. Fluid Mech.*, **272**: 109–133, 1994.

[163] Vinothan N. Manoharan. *Science*, **349**: 1253751–1253751, 2015.

[164] M. Chaudhuri et al. *Phys. Rev. Lett.*, **119**: , 2017.

The compacting and ordering effect of confining walls is known as a promoter of nucleation/crystallization. Polycrystalline patches evolve early in the outer shell at the droplet interface and propagate rapidly into the nearest inner layers.[111] However, this effect diminishes gradually with each subsequent layer until it completely vanishes at about the 4th to 5th layer in compression-driven packings as shown in Chapter 3.[21,76,79] The latter can be attributed to the propagation of defects from the outer layers.[114] In the case of a flexible confining surface, such as a the droplet interface, confinement effects can be suppressed under given circumstances: when the evaporation time is sufficiently long, e.g. from weeks to over a month as shown by Wang et al. for evaporating droplets in an emulsion.[111] Here, thermodynamically favored bulk crystallization prevails over surface-induced nucleation, as the flexible interface allows the rearrangement and healing of defects, leading to a monocrystalline structure.[111,112]

Another strategy to suppress confinement-induced crystallization is to increase the mobility of the colloidal NPs, for example by reducing their size. In this case, the final structure will be dominated by a bulk-like arrangement, which, as already addressed, involves a rcp configuration for the achievable evaporation times in aerosol drying or a monocrystalline configuration for very long evaporation times, realizable in the drying of emulsions.[111]

The number of NPs comprising a cluster also affects its structure. So, the higher the number of NPs, the more inner layers are formed and the lesser the confinement effect will be, until a point where the inner bulk region dominates over the outer polycrystalline shells. In addition, for small numbers (i.e. $< 10^5$), the most stable bulk structure will adopt crystalline arrangements that differ from the fcc configuration. The exact arrangement geometry depends on the exact amount of NPs, the so-called magic numbers [111, 112].

---

[34] Clara Weis et al. *Sci. Rep.*, **6**: 1–15, 2016.
[112] Bart De Nijs et al. *Nat. Mater.*, **14**: 56–60, 2015.
[21] Hector Rusinque et al. *Comm. Compu. Inf. Sci.*, **1199**: 104–121, 2020.
[76] Stefan Bruns et al. *J. Chromatogr. A*, **1318**: 189–197, 2013.
[79] Robert S. Maier et al. *Phys. Fluids*, **15**: 3795–3815, 2003.
[114] Brian Giera et al. *Langmuir*, **33**: 652–661, 2016.

8 Outlook

In the following, possible research topics as extensions of this work are suggested. Regarding the mass transport of tracers in heterogeneous porous media, it was shown that the performance of continuum approaches, specifically the method of volume averaging (MVA), is superior to particle-based approaches. However, traditional continuous models cannot deal with heterogeneous systems, as they use average properties that are not capable of capturing local particularities of the material structure. As shown in Chapter 3, two dominant regions conforming the heterogeneous material were identified. When considered individually, these regions exhibit homogeneous characteristics. It is therefore proposed to study the feasibility of treating a heterogeneous medium as the combination of smaller homogeneous regions capable of exchanging mass with each other.

The particle-based methods used in this work calculate the displacement of the individual particles in each discretized time step based on external fields and pairwise particle interactions. As shown in Chapter 4, a further option is to estimate the probability of a certain step taking place by a random number, which is generated based on criteria satisfying the corresponding probability. Another example of this was shown by Stylianopoulos et al. with a case of electric repulsive forces [165]. In the first case mentioned, the criterion used was the porosity of an effective medium, which determines the permeability of the medium surface and consequently the probability of a tracer entering the effective medium. Building on this, the probability of a reaction taking place can also be used to model the reaction kinetics, for instance, in heterogeneous catalysis. Here, the well-known Arrhenius equation comes into play, as it can be interpreted as the product of two probabilities: The probability that a given collision involves sufficient energy to overcome the activation energy, which is given by the exponential part of the equation (similar to [165]). And the pre-exponential factor, which gives the probability that colliding particles with enough energy to overcome the activation energy end up effectively reacting.

There is a need for further investigation of packing processes and the consolidation of these structures, for instance, in order to escalate the number of nanoparticles considered so that the effect of both, the confinement and the bulk suspension can be resolve simultaneously in a numerical approach.

List of Figures

1.1 Graphical abstract of publication 1. (a) Porosity profile of a heterogeneous random sphere-packing along the vertical axis. (b) Projection of the particle-center coordinates on the plane perpendicular to the flow. (c) Streamlines through the sphere packing near the top and bottom confining walls as well as in the center of the packing. (d) Green-highlighted hexagonal configurations induced by the confining walls. 7

1.2 Graphical abstract of publication 2. (a) Nanoparticulate cluster. (b),(c),(d) Molecules with different sizes diffusing in individual pores and random walks of these molecules. (e) Schematic representation of the pairwise interactions between a diffusing molecule and the wall atoms hindering diffusion. 8

1.3 Graphical abstract of publication 3. Bulk structure of nanoparticulate clusters at two different solid volume fractions, $\Phi = 0.30$ and $\Phi = 0.45$ and three different electric surface potentials $\psi_{0,2} = 115\,\mathrm{mV}$, $\psi_{0,1} = 50\,\mathrm{mV}$ and $\psi_{0,0} = 0\,\mathrm{mV}$. 9

1.4 Graphical abstract of publication 4. (a) Nanoparticulate cluster (b) Schematic representation of the charged particles, the deposit and the electrodes of the deposition chamber. (c) Random walks of the charged particles. (d) Deposit pattern on the lower electrode (substrate). 10

2.1 Velocity directions of a fluid cell in the D3Q19 model 20

2.2 Relative diffusivity vs. solid fraction. Hard-sphere case, the most studied case in literature. 25

3.1 Periodic unit cell of the in-line cylinder arrangements with a graphic representation of the velocity field for three porosity values. The distance in the x and y axes, and velocities were normalized by the maximal magnitude of the distance and velocity field, respectively, and are hence dimensionless. ε stands for the porosity of the cells 36

3.2 Axial dispersion coefficients as a function of the Péclet number in the in-line cylinder arrangements considered. 37

3.3 Radial dispersion coefficients as a function of the Péclet number in the in-line cylinder arrangements considered (see legend in Figure 3.2). . . . 37

3.4 At the top the sphere packings of finite H/d-ratios are shown. Below, characteristic pathlines close to the wall ($z \approx 0$) and in the middle of the packing ($z = H/2$) are plotted for each packing, respectively. 39

3.5 Axial dispersion coefficients as a function of the Péclet number in the sphere packings considered. 41

3.6 Radial dispersion coefficients as a function of the Péclet number in the sphere packings considered. 41

3.7 (a)–(d) show selected views of the pathlines in the sphere packing with $H/d = 6$: close to the wall at $z \approx 0$ in (b) and (d), and in the middle of the packing at $z = H/2$ in (a) and (c). Additionally in (e), a portion of the periodic sphere packing and its related pathlines are presented. 45

3.8 Porosity profiles along the z-axis and projections of the sphere centers on a plane perpendicular to the walls, also along the z-axis from left to right. 46

4.1 Discretization of the pore walls at the atomic level to calculate the interactions between wall atoms and solute molecules, where r_{co} is the cutoff radius above which the interactions are neglected and $\overline{L}_{ww}$ represents the average bond length between a pair of wall atoms. The chaotic lines within the cylindrical pore represent computed trajectories (random walks) of selected particles. 56

4.2 Local hindrance probability f_j and its complementary probability k_j as a function of the dimensionless distance between diffusing particle and wall atom. 58

4.3 Diffusive hindrance factor K_d in straight cylindrical pores versus the reduced molecular diameter λ. The molecular diameter $2r_m$is given by $2r_m = 2\sigma_{sw}$. 59

4.4 a) Diffusive hindrance factor $K_{d,\mathrm{cyl}}$ as a function of the ratios of the distance σ_{sw} and the pore size x to the mean bond length $\overline{L}_{ww}$, in straight cylindrical pores (circles) with curves fitting the results (solid lines). b) $K_{d,\mathrm{cyl}}$ for cutoff radii $r_{co}/\sigma_{sw} = 2.2$ and $r_{co}/\sigma_{sw} = 3.0$. 60

4.5 Staggered cylinder arrangement confined in a narrow slit. The bulk flow occurs as a consequence of a force or pressure gradient acting in the positive x-axis direction. The velocity field is graphically represented in the lower left corner. 61

4.6 a) Longitudinal diffusivity in a staggered cylinder arrangement as a function of the Péclet number. The effect of the resolution of the lattice used for the discretization of the geometry is also graphically represented. The resolution used in the simulations of Khirevich was 200 grid nodes per cylinder diameter, $d = 200$. b) Taylor dispersion as a function of the Péclet number compared with its analytical solution. 62

4.7 Hierarchic-nanoporous structure used as a medium in the application example. Porescales according to the IUPAC definition for nanoporous materials. 63

4.8 a) Macropores (MP) and mesopores (mP) of the microscale. b) Effective representation of the mesoporous medium. 64

4.9 Time evolution of the diffusivity of a simple cubic arrangement of spheres for the cases of spatially resolved and non-resolved mesopores (see Fig. 8). The parameters considered are $K_d = 1$, $K_\tau = D_{\text{eff,mP}}/D_\infty = 0.729$, $\varepsilon_{m\text{P}} = 0.454$, and $\varepsilon_{\text{MP}} = 1$. 64

4.10 On the left, diffusive hindrance factor K_d in a computer-generated Building-Block BB1. Direct simulation and PSD approximations of K_d based on normal distributions $\mathcal{N}$ centered at $\bar{x} = x_{cyl}$ with different standard deviations. On the right, PSDs $q_3(x)$ considered. The distributions are slightly skewed to the left $\mathcal{N}^-$ and to the right $\mathcal{N}^+$, to a greater extent for $\mathcal{N}^{++}$, without changing $\bar{x}$. 66

4.11 On the left, diffusive hindrance factor K_d in a computer-generated Building-Block BB2. Direct simulation and PSD approximations of K_d based on normal distributions $\mathcal{N}$ centered at $\bar{x} = x_{cyl}$ with different standard deviations. On the right, PSDs $q_3(x)$ considered. The distribution $\mathcal{N}^+$ is slightly skewed to the right without changing $\bar{x}$. 67

4.12 Total hindrance to diffusion, i.e. the obstrucion factor K_τ and diffusive hindrance factor K_d related to the layers made of the Building-Blocks BB1 and BB2. 68

5.1 Pore size distribution of the produced clusters with different nanoparticle sizes. 77

5.2 Relative diffusivity vs. solid volume fraction for a colloidal dispersion of hard-sphere-like particles. 78

5.3 (a) Initial state of a droplet of the atomized dispersion prior to the first evaporation stage. The larger (blue) circle represents a droplet and the inner (gray) circles represent the dispersed nanoparticles. (b) Final state of the first stage and initial state of the second evaporation stage. The change in color of the dispersion medium indicates the transformation from water (in blue) to crystals of hydrated metallic salts (in red). (c) Secondary water reservoir as ultra-pure dispersion medium. The increase in temperature leads to the dehydration of the metallic salts and consequently to the second evaporation stage, where the metallic components agglomerate to form metallic NPs (black circles). (d) Dried nanoparticulate cluster. . . . 80

5.4 Effect of the pore size (or particle size) and cobalt nitrate concentration on the retention of HCl for a cobalt nitrate loading of $3.8\,\%$. 82

5.5 Effect of the pore size and cobalt nitrate concentration on the retention of HCl for a cobalt nitrate loading of $20.0\,\%$. 82

5.6 Structural order vs. surface potential with $\psi_{0,2} = 115\,\mathrm{mV}$, $\psi_{0,1} = 50\,\mathrm{mV}$, $\psi_{0,0} = 0\,\mathrm{mV}$ (i.e. hard spheres) and an ionic strength of $0.01\,\mathrm{mol\,L^{-1}}$. . . . 84

5.7 Relative diffusivity vs. solid volume fraction for different electric surface potentials with the same ionic strength. 85

5.8 Relative diffusivity vs. volume fraction. 91

5.9 Number-weighted particle size distribution of the primary NPs used to produce the clusters. 91

5.10 Comparison of the numerical solution obtained from the PB solver with the Debye-Hückel potential of a NP of radius $a = 130.0\,\mathrm{nm}$, surface potential $\psi_0 = 15\,\mathrm{mV}$ in a solution $0.003\,\mathrm{mol\,L^{-1}}$ of a monovalent salt. The resulting screening Debye length for water at $20\,°\mathrm{C}$ is $\lambda_D = 173.1\,\mathrm{nm}$. 92

5.11 Comparison of the numerical solution obtained from the PB solver with the Debye-Hückel potential of a NP of radius $a = 130.0\,\mathrm{nm}$, surface potential $\psi_0 = 150\,\mathrm{mV}$ in a solution $0.003\,\mathrm{mol\,L^{-1}}$ of a monovalent salt. The resulting screening Debye length for water at $20\,°\mathrm{C}$ is $\lambda_D = 173.1\,\mathrm{nm}$. The surface charge density imposed as boundary condition at the NP surface is calculated with $\sigma = \epsilon_0 \epsilon_r\, \psi_0\,(1 + a/\lambda)/a$ [135]. 93

6.1 Electrode arrangement with potential difference and dimensions. Here, d_{op} stands for the opening diameter of the mask, S_{op} for the spacing between openings, B_{M} for the mask thickness, H_{D} for the distance between the upper electrode (the "ceiling") and the mask electrode in the middle, and H_{el} for the distance between the mask and substrate electrodes (in the following referred as electrode gap). The same potential difference between the mask and the substrate ($\Delta\phi$) is applied between the ceiling and the substrate, so that there is no difference in potential between the ceiling and the mask. 99

6.2 a) The electric field lines (in black) emerging from the ceiling of the deposition chamber run from high to low potential. The equipotential lines (perpendicular to the field lines) are red for high potential and turn yellow, green and blue as the potential goes down. b) Alternatively, the equipotential lines can be seen as a potential surface on which the nanoparticles spontaneously move downhill transforming potential energy into kinetic energy. This example is taken from the results presented in the verification case using a slit-shaped mask opening (see Sec. 6.5.1). 101

6.3 a) The trajectories of eleven nanoparticles are shown as well as the electric field lines between the electrodes for the geometry used in the verification case (see Section 6.5.1) at a potential difference of 0.5 and $3\,\mathrm{V}$, respectively, for an opening diameter of $d_{\mathrm{op}} = 4\,\mu\mathrm{m}$. b) The final positions of the deposited nanoparticles are shown above. The Gaussian-shaped curves represent the spatial distributions of the deposited nanoparticles in the form of a probability density function (PDF). The green lines are the Gaussian functions fitted to the simulation results represented by the blue points. 102

6.4 Height of the Gaussian-shaped structure H_{c} reconstructed on the surface of the substrate and opening size d_{op}. 103

6.5 a & b) Effect of the variation of the potential difference on the focusing effect for a given electrode gap H_{el}. b) Effect of the deposited nanoparticles forming 3D structures with two different heights $H_c/d_{\mathrm{op}} = 0.0250$ and 0.0375 . The results are compared with the experimental and simulation results of Choi et al.[154] 103

6.6 Effect of the variation of charge and size of the nanoparticles on the pattern width. The potential difference per electrode gap was varied between 0.25 and $1\,\mathrm{V}\,\mu\mathrm{m}^{-1}$. 105

---

[154] HOSEOP CHOI et al. *J. Aerosol Sci.*, **88**: 90–97, 2015.

6.7 a) Effect of varying the spacing between openings and the mask thickness on the pattern width. A potential difference per electrode gap of $\Delta\phi/H_{\mathrm{el}} = 0.75\,\mathrm{V\,\mu m^{-1}}$ was applied for these two simulation cases. b) Effect of the electrode gap on the pattern width. 106

6.8 Convergence of the field lines onto the substrate. Field lines emerging from the upper face of the mask are in red, whereas the black field lines originate from the ceiling of the deposition chamber. The pattern in the figure represents the points, where selected electric field lines touch the substrate. Here, the red and black contact points correspond to the red and black field lines, respectively. The brighter points outside the red circle correspond to field lines originating from the faces of the mask opening. The pattern width per opening diameter (W_c/d_{op}) is shown for each case. 108

6.9 Péclet number (Pe) of the nanoparticles (left axis) and average velocity $\langle v_x \rangle$ (right axis) at two particle sizes and potential differences. The velocities are computed for an opening diameter $d_{\mathrm{op}} = 4\,\mathrm{\mu m}$ and an electrode gap $H_{\mathrm{el}} = 4\,\mathrm{\mu m}$. The particles were introduced into the deposition chamber at $x = 0$ and move randomly until they come close to the mask openings located at $x/d_{\mathrm{op}} = 3.75$ where the electrical potential drops sharply. As a result, the potential energy of the particles is abruptly converted to kinetic energy, leading to an abrupt increase of Pe. 109

6.10 Normalized field strength E_x for a given xy-plane at $z = S_{\mathrm{op}}/2$. As a result of the normalization, the normalized field strength is generally valid for any potential difference applied. 110

6.11 Pattern width as a function of the inversed dimensionless number $\Omega_{\mathrm{el}}^{-1}$, which under isothermal conditions can be viewed as a dimensionless electric force ($W_{\mathrm{c}}/d_{\mathrm{op}}$ vs F_{el}). The solid lines represent the fitting function obtained for each case using the function proposed in Eq. 6.10. 111

List of Tables

3.1 Selected descriptors of the porous structure of the in-line cylinders. The diffusive tortuosity values presented were computed with the MVA approach. 38
3.2 Selected descriptors of the porous structure of the sphere packings. The tortuosity values have a standard deviation of 0.03. 42

5.1 Type of cluster configurations and range of their solid volume fractions obtained in this work and by other authors. All the clusters were produced by drying of droplets dispersed as aerosols or emulsions using approximately monodisperse NPs. The prevalent cluster structures are random close packing (rcp), polycrystalline (PC), and monocrystalline (MC) configurations, which appear as fcc or icosahedral (ico) arrangements. 75

6.1 Dimensions for the electrode arrangement considered in the following simulations. All lengths are given in multiples of d_{op}. 104
6.2 Considered shapes of the mask openings, trough which the nanoparticles move from the upper to the lower section of the deposition chamber at $\Delta\phi/H_{\mathrm{el}} = 0.75\,\mathrm{V}\,\mu\mathrm{m}^{-1}$. a,b and c show the cross sections of the openings evaluated in the simulations (see Fig. 6.8). 107
6.3 Coefficients of the power function for the cases studied. 112

[1] J.M.P.Q. DELGADO (AUTH.) FRANK A. COUTELIERIS. *Transport Processes in Porous Media*. 1st ed. Advanced Structured Materials 20 Springer-Verlag Berlin Heidelberg, 2012. (see p. 5)

[2] SIARHEI KHIREVICH, ANTON DANEYKO, ALEXANDRA HÖLTZEL, ANDREAS SEIDEL-MORGENSTERN, & ULRICH TALLAREK. Statistical analysis of packed beds, the origin of short-range disorder, and its impact on eddy dispersion. *Journal of Chromatography A*, **1217**: 4713–4722, 2010. (see p. 5)

[3] H. LIASNEUSKI, D. HLUSHKOU, S. KHIREVICH, A. HÖLTZEL, U. TALLAREK, & S. TORQUATO. Impact of microstructure on the effective diffusivity in random packings of hard spheres. *Journal of Applied Physics*, **116**: 034904, 2014. (see p. 5)

[4] A. A. MOHAMAD. Lattice Boltzmann Method: Fundamentals and Engineering Applications with Computer Codes. Springer–Verlag London, 2011. (see pp. 5, 17, 19–21)

[5] DIETER HÄNEL. Molekulare Gasdynamik: Einführung in die kinetische Theorie der Gase und Lattice-Boltzmann-Methoden. Springer–Verlag Berlin Heidelberg, 2004. (see pp. 5, 17–19, 21)

[6] H. W. HAYNES JR. & L. F. BROWN. Effect of pressure on predicted and observed diffusion rates in constricted poresa theoretical study. *AIChE Journal*, **17**: 491–494, 1971. (see p. 2)

[7] MARVIN F.L. JOHNSON & WARREN E. STEWART. Pore structure and gaseous diffusion in solid catalysts. *Journal of Catalysis*, **4**: 248–252, 1965. (see p. 2)

[8] RICHARD N. FOSTER & JOHN B. BUTT. A computational model for the structure of porous materials employed in catalysis. *AIChE Journal*, **12**: 180–185, 1966. (see p. 2)

[9] ROBERT GÜTTEL & THOMAS TUREK. Improvement of Fischer-Tropsch Synthesis through Structuring on Different Scales. *Energy Technology*, **4**: 44–54, 2016. (see pp. 3, 62, 98)

[10] LI CHEN, RUIYUAN ZHANG, TING MIN, QINJUN KANG, & WENQUAN TAO. Pore-scale study of effects of macroscopic pores and their distributions on reactive transport in hierarchical porous media. *Chemical Engineering Journal*, **349**: 428–437, 2018. (see pp. 3, 62, 98)

[11] JIAN YIN, TIANQI ZHANG, EMILY SCHULMAN, DONGXIA LIU, & JIANQIANG MENG. Hierarchical porous metallized poly-melamine-formaldehyde (PMF) as a low-cost and high-efficiency catalyst for cyclic carbonate synthesis from CO2 and epoxides. *Journal of Materials Chemistry A*, **6**: 8441–8448, 2018. (see pp. 3, 62, 98)

[12] RAVI SHARMA, TIRIANA SEGATO, MARIE PAULE DELPLANCKE, HERMAN TERRYN, GINO V. BARON, JOERI F.M. DENAYER, & JULIEN COUSIN-SAINT-REMI. Hydrogen chloride removal from hydrogen gas by adsorption on hydrated ion-exchanged zeolites. *Chemical Engineering Journal*, **381**: 122512, 2020. (see pp. 3, 81, 115)

[13] A. EINSTEIN. Über die von der molekularkinetischen Theorie der Wärme geforderte Bewegung von in ruhenden Flüssigkeiten suspendierten Teilchen (translated into English under the title: Investigations on the Theory of the Brownian Movement). *Annalen der Physik*, **322**: 549–560, 1905. (see pp. 4, 13, 51, 109)

[14] M. MEZHERICHER, A. LEVY, & I. BORDE. Modelling the morphological evolution of nanosuspension droplet in constant-rate drying stage. *Chemical Engineering Science*, **66**: 884–896, 2011. (see pp. 4, 73, 116)

[15] MICHAEL P. HOWARD, WESLEY F. REINHART, TANMOY SANYAL, M. SCOTT SHELL, ARASH NIKOUBASHMAN, & ATHANASSIOS Z. PANAGIOTOPOULOS. Evaporation-induced assembly of colloidal crystals. *Journal of Chemical Physics*, **149**: 094901, 2018. (see pp. 4, 24, 73–75, 116)

[16] KATARZYNA JABŁCZYŃSKA, JAKUB M. GAC, & TOMASZ R. SOSNOWSKI. Self-organization of colloidal particles during drying of a droplet: Modeling and experimental study. *Advanced Powder Technology*, **29**: 3542–3551, 2018. (see pp. 4, 73, 74)

[17] SABRINA ZELLMER, GEORG GARNWEITNER, THOMAS BREINLINGER, TORSTEN KRAFT, & CARSTEN SCHILDE. Hierarchical Structure Formation of Nanoparticulate Spray-Dried Composite Aggregates. *ACS Nano*, **9**: 10749–10757, 2015. (see pp. 4, 73, 74)

[18] THOMAS BREINLINGER, ADHAM HASHIBON, & TORSTEN KRAFT. Simulation of the spray drying of single granules: The correlation between microscopic forces and granule morphology. *Journal of the American Ceramic Society*, **98**: 1778–1786, 2015. (see pp. 4, 73)

[19] THOMAS BREINLINGER, ADHAM HASHIBON, & TORSTEN KRAFT. Simulation of the influence of surface tension on granule morphology during spray drying using a simple capillary force model. *Powder Technology*, **283**: 1–8, 2015. (see pp. 4, 73)

[20] WENDONG LIU, JIARUL MIDYA, MICHAEL KAPPL, HANS JÜRGEN BUTT, & ARASH NIKOUBASHMAN. Segregation in Drying Binary Colloidal Droplets. *ACS Nano*, **13**: 4972–4979, 2019. (see pp. 4, 73)

[21] HECTOR RUSINQUE, EUGENIA BARTHELMIE, & GUNTHER BRENNER. Numerical Study of Dispersive Mass Transport in Homogeneous and Heterogeneous Porous Media. *Communications in Computer and Information Science*, **1199**: 104–121, 2020. (see pp. 6, 21, 75, 117)

[22] HECTOR RUSINQUE & GUNTHER BRENNER. Mass transport in porous media at the micro- and nanoscale: A novel method to model hindered diffusion. *Microporous and Mesoporous Materials*, **280**: 157–165, 2019. (see pp. 6, 28, 29, 31, 35)

[23] HECTOR RUSINQUE, ALFRED WEBER, ELENA FEDIANINA, & GUNTHER BRENNER. Numerical study of the controlled electrodeposition of charged nanoparticles in an electric field. *Journal of Aerosol Science*, **129**: 28–39, 2018. (see pp. 11, 34, 54)

[24] H G SCHUSTER & WOLFAM JUST. *Deterministic Chaos*. Wiley, 1994. (see pp. 14, 34, 54, 100)

[25] GIORGIO VOLPE & GIOVANNI VOLPE. Simulation of a Brownian particle in an optical trap. *American Journal of Physics*, **81**: 224–230, 2013. (see pp. 14, 34, 54, 100)

[26] G. CHEN. Nanoscale Energy Transport and Conversion: A Parallel Treatment of Electrons, Molecules, Phonons, and Photons. Oxford University Press, 2005. (see pp. 16–19)

[27] S. HARRIS. An Introduction to the Theory of the Boltzmann Equation. Dover Publications, 2012. (see p. 16)

[28] M.C. SUKOP & D.T. THORNE. Lattice Boltzmann Modeling: An Introduction for Geoscientists and Engineers. Springer Berlin Heidelberg, 2010. (see pp. 17, 19)

[29] D. ARUMUGA PERUMAL & ANOOP K. DASS. A Review on the Development of Lattice Boltzmann Computation of Macro Fluid Flows and Heat Transfer. *Alexandria Engineering Journal*, **54**: 955 –971, 2015. (see pp. 19, 20, 30, 47, 49)

[30] Pieter J. In't Veld, Matt K. Petersen, & Gary S. Grest. Shear thinning of nanoparticle suspensions. *Physical Review E - Statistical, Nonlinear, and Soft Matter Physics*, **79**: 10–13, 2009. (see pp. 24, 74, 83)

[31] P. R. Schunk, F. Pierce, J. B. Lechman, A. M. Grillet, P. J. in't Veld, H. Weiss, C. Stoltz, & D. R. Heine. Performance of mesoscale modeling methods for predicting rheological properties of charged polystyrene/water suspensions. *Journal of Rheology*, **56**: 353–384, 2012. (see pp. 24, 74, 83, 90)

[32] Dan S Bolintineanu, Gary S Grest, Jeremy B Lechman, Flint Pierce, Steven J. Plimpton, & P. Randall Schunk. Particle dynamics modeling methods for colloid suspensions. *Computational Particle Mechanics*, **1**: 321–356, 2014. (see pp. 24, 74, 83, 89, 90)

[33] John F. Brady. The long-time self-diffusivity in concentrated colloidal dispersions. *Journal of Fluid Mechanics*, **272**: 109–133, 1994. (see pp. 24, 73–75, 78, 84, 85, 116)

[34] Clara Weis, Claude Oelschlaeger, Dick Dijkstra, Meik Ranft, & Norbert Willenbacher. Microstructure, local dynamics, and flow behavior of colloidal suspensions with weak attractive interactions. *Scientific Reports*, **6**: 1–15, 2016. (see pp. 24, 25, 74, 78, 117)

[35] Heather M. Shewan & Jason R. Stokes. Analytically predicting the viscosity of hard sphere suspensions from the particle size distribution. *Journal of Non-Newtonian Fluid Mechanics*, **222**: 72–81, 2014. (see pp. 24, 74, 84, 85)

[36] Vasili Baranau & Ulrich Tallarek. Random-close packing limits for monodisperse and polydisperse hard spheres. *Soft Matter*, **10**: 3826–3841, 2014. (see pp. 25, 65, 77)

[37] Vasili Baranau, Song Chuan Zhao, Mario Scheel, Ulrich Tallarek, & Matthias Schröter. Upper bound on the Edwards entropy in frictional monodisperse hard-sphere packings. *Soft Matter*, **12**: 3991–4006, 2016. (see pp. 25, 116, 117)

[38] Jörg Baumgartl, Julian Dietrich, Jure Dobnikar, Clemens Bechinger, & Hans Hennig von Grünberg. Phonon dispersion curves of two-dimensional colloidal crystals: the wavelength-dependence of friction. *Soft Matter*, **4**: 2199, 2008. (see p. 25)

[39] Zhengdong Cheng, Jixiang Zhu, William B Russel, & P M Chaikin. Phonons in an entropic crystal. *Physical Review Letters*, **85**: 1460–1463, 2000. (see p. 25)

[40] R. S. Penciu, M. Kafesaki, G. Fytas, E. N. Economou, W. Steffen, A. Hollingsworth, & W. B. Russel. Phonons in colloidal crystals. *Europhysics Letters*, **58**: 699–704, 2002. (see p. 25)

[41] Stephen Whitaker. *The Method of Volume Averaging*. **volume** 13 Theory and Applications of Transport in Porous Media Kluwer Academic Publishers, 1999. 219 (see pp. 27, 29, 31, 32)

[42] F.J. Valdes-Parada & C.G. Aguilar-Madera. Upscaling Mass Transport with Homogeneous and Heterogeneous Reaction in Porous Media. *Chemical Engineering Transactions*, **24**: 1453–1458, 2011. (see pp. 27, 29, 31, 32)

[43] Helen D. Lugo-Méndez, Francisco J. Valdés-Parada, Mark L. Porter, Brian D. Wood, & J. Alberto Ochoa-Tapia. Upscaling Diffusion and Nonlinear Reactive Mass Transport in Homogeneous Porous Media. *Transport in Porous Media*, **107**: 683–716, 2015. (see pp. 27, 29, 31, 32)

[44] Ulrich Hornung, **editor**. *Homogenization and Porous Media*. **volume** 6 Interdisciplinary Applied Mathematics New York: Springer, 1991. 1–279 (see pp. 27, 29)

[45] William G. Gray & Cass T. Miller. Thermodynamically constrained averaging theory approach for modeling flow and transport phenomena in porous medium systems: 1. Motivation and overview. *Advances in Water Resources*, **28**: 161–180, 2005. (see pp. 28, 29)

[46] TOBIAS HEIDIG, THOMAS ZEISER, WILHELM SCHWIEGER, & HANNSJÖRG FREUND. Ortsaufgelöste Simulation des externen Stofftransports in komplexen Katalysatorträgergeometrien. *Chemie-Ingenieur-Technik*, **86**: 554–560, 2014. (see pp. 28, 29, 31, 48, 49)

[47] SIARHEI KHIREVICH, ANTON DANEYKO, ALEXANDRA HÖLTZEL, ANDREAS SEIDEL-MORGENSTERN, & ULRICH TALLAREK. Statistical analysis of packed beds, the origin of short-range disorder, and its impact on eddy dispersion. *Journal of Chromatography A*, **1217**: 4713–4722, 2010. (see pp. 28, 29, 31, 48–50)

[48] HARUN KOKU, ROBERT S MAIER, MARK R SCHURE, & ABRAHAM M LENHOFF. Modeling of dispersion in a polymeric chromatographic monolith. *Journal of Chromatography A*, **1237**: 55–63, 2012. (see pp. 28, 29, 31, 48, 49)

[49] BEHZAD GHANBARIAN, ALLEN G. HUNT, ROBERT P. EWING, & MUHAMMAD SAHIMI. Tortuosity in Porous Media: A Critical Review. *Soil Science Society of America Journal*, **77**: 1461, 2013. (see pp. 29, 33)

[50] P.C. CARMAN. Fluid flow through granular beds. *Chemical Engineering Research and Design*, **75**: S32 –S48, 1937. (see pp. 29, 33)

[51] J. BEAR. *Dynamics of Fluids In Porous Media*. v. 1 American Elsevier, 1972. (see pp. 29, 33)

[52] CARL FREDRIK BERG. Permeability Description by Characteristic Length, Tortuosity, Constriction and Porosity. *Transport in Porous Media*, **103**: 381–400, 2014. (see pp. 29, 33)

[53] S. M.REZAEI NIYA & A. P.S. SELVADURAI. A Statistical Correlation Between Permeability, Porosity, Tortuosity and Conductance. *Transport in Porous Media*, **121**: 741–752, 2018. (see pp. 29, 33)

[54] B.J. KIRBY. *Micro- and Nanoscale Fluid Mechanics: Transport in Microfluidic Devices*. Cambridge University Press, 2010. (see p. 30)

[55] L.G. LEAL. *Advanced Transport Phenomena: Fluid Mechanics and Convective Transport Processes*. Cambridge Series in Chemical Engineering Cambridge University Press, 2010. (see p. 30)

[56] XIAOWEN SHAN. Lattice Boltzmann in micro- and nano-flow simulations. *IMA Journal of Applied Mathematics*, **76**: 650–660, 2011. (see pp. 30, 47, 49)

[57] MARTIN S. ALNÆS, ANDERS LOGG, KRISTIAN B. ØLGAARD, MARIE E. ROGNES, & GARTH N. WELLS. Unified Form Language: A domain-specific language for weak formulations of partial differential equations. *ACM Transactions on Mathematical Software*, **40**: 2014. (see pp. 31, 33, 92)

[58] MARTIN S. ALNÆS, JAN BLECHTA, JOHAN HAKE, AUGUST JOHANSSON, BENJAMIN KEHLET, ANDERS LOGG, CHRIS RICHARDSON, JOHANNES RING, MARIE E. ROGNES, & GARTH N. WELLS. The FEniCS Project Version 1.5. *Archive of Numerical Software*, **3**: 2015. (see pp. 31, 33, 92)

[59] XIAOYI HE & LI SHI LUO. Theory of the lattice Boltzmann method: From the Boltzmann equation to the lattice Boltzmann equation. *Physical Review E*, **55**: 6811–6820, 1997. (see p. 31)

[60] SAURO SUCCI. *The Lattice Boltzmann Equation for Fluid Dynamics and Beyond (Numerical Mathematics and Scientific Computation)*. Numerical mathematics and scientific computation Oxford University Press, USA, 2001. (see p. 31)

[61] DIETER A. WOLF-GLADROW. *Lattice-gas cellular automata and lattice Boltzmann models : an introduction*. Springer, 2000. 308 (see p. 31)

[62] R. ARIS. On the Dispersion of a Solute in a Fluid Flowing through a Tube. *Proceedings of the Royal Society A: Mathematical, Physical and Engineering Sciences*, **235**: 67–77, 1956. (see pp. 33, 37, 61)

[63] A. KOPONEN, M. KATAJA, & J. TIMONEN. Tortuous flow in porous media. *Physical Review E*, **54**: 406–410, 1996. (see p. 33)

[64] ARTUR DUDA, ZBIGNIEW KOZA, & MACIEJ MATYKA. Hydraulic tortuosity in arbitrary porous media flow. *Physical Review E*, **84**: 036319, 2011. (see p. 33)

[65] XIN BIAN, CHANGHO KIM, & GEORGE EM KARNIADAKIS. 111 years of Brownian motion. *Soft Matter*, **12**: 6331–6346, 2016. (see pp. 34, 54, 108, 109)

[66] L. BOLTZMANN. *Vorlesungen über Gastheorie (translated into English as "Lectures on Gas Theory".)* Vorlesungen über Gastheorie J. A. Barth, 1898. (see pp. 34, 53, 54)

[67] W. M. DEEN. Hindered transport of large molecules in liquid-filled pores. *AIChE Journal*, **33**: 1409–1425, 1987. (see pp. 34, 35, 52–54)

[68] GUIHUA ZHANG & TAMAR SCHLICK. Implicit discretization schemes for Langevin dynamics. *Molecular Physics*, **84**: 1077–1098, 1995. (see pp. 35, 58, 100)

[69] N. HOZE & D. HOLCMAN. Statistical methods for large ensemble of super-resolution stochastic single particle trajectories. *bioRxiv*, 227090, 2017. (see p. 35)

[70] D.K. JONES. *Diffusion MRI*. Oxford University Press, 2010. (see p. 35)

[71] PANADDA DECHADILOK & WILLIAM M. DEEN. Hindrance Factors for Diffusion and Convection in Pores. *Industrial and Engineering Chemistry Research*, **45**: 6953–6959, 2006. (see pp. 35, 50, 52, 62)

[72] ROBERT EVANS, GUILHERME DAL POGGETTO, MATHIAS NILSSON, & GARETH A. MORRIS. Improving the Interpretation of Small Molecule Diffusion Coefficients. *Analytical Chemistry*, **90**: 3987–3994, 2018. (see pp. 35, 49)

[73] JIE XIAO & XIAO DONG CHEN. Multiscale modeling for surface composition of spray-dried two-component powders. *AIChE Journal*, **60**: 2416–2427, 2014. (see pp. 35, 49)

[74] PETR DVOŘÁK, MÁRIA ŠOLTÉSOVÁ, & JAN LANG. Microfriction correction factor to the Stokes-Einstein equation for small molecules determined by NMR diffusion measurements and hydrodynamic modelling. *Molecular Physics*, **8976**: 2018. (see pp. 35, 49)

[75] R. ANDREW SHALLIKER, B. SCOTT BROYLES, & GEORGES GUIOCHON. Physical evidence of two wall effects in liquid chromatography. *Journal of Chromatography A*, **888**: 1–12, 2000. (see p. 39)

[76] STEFAN BRUNS, EDWARD G. FRANKLIN, JAMES P. GRINIAS, JUSTIN M. GODINHO, JAMES W. JORGENSON, & ULRICH TALLAREK. Slurry concentration effects on the bed morphology and separation efficiency of capillaries packed with sub-2μm particles. *Journal of Chromatography A*, **1318**: 189–197, 2013. (see pp. 40, 42, 75, 117)

[77] HECTOR RUSINQUE, EUGENIA BARTHELMIE, BRENNER GUNTHER, & ALFRED WEBER. *Skalenauflösende Berechnung der Diffusion und hydrodynamischen Dispersion in inhomogenen porösen Medien*. Technische Universität Clausthal, 2016. (see p. 40)

[78] KENNETH W. DESMOND & ERIC R. WEEKS. Random close packing of disks and spheres in confined geometries. *Physical Review E*, **80**: 051305, 2009. (see p. 40)

[79] ROBERT S. MAIER, DANIEL M. KROLL, ROBERT S. BERNARD, STACY E. HOWINGTON, JOHN F. PETERS, & H. TED DAVIS. Hydrodynamic dispersion in confined packed beds. *Physics of Fluids*, **15**: 3795–3815, 2003. (see pp. 40, 75, 117)

[80] ALEXANDER BUFE, MATTHIAS KLEE, GREGOR WEHINGER, THOMAS TUREK, & GUNTHER BRENNER. 3D Modeling of a Catalyst Layer with Transport Pores for Fischer-Tropsch Synthesis. *Chemie Ingenieur Technik*, **89**: 1385–1390, 2017. (see pp. 47, 49, 55, 61, 63)

[81] SIARHEI KHIREVICH, ALEXANDRA HÖLTZEL, ANTON DANEYKO, ANDREAS SEIDEL-MORGENSTERN, & ULRICH TALLAREK. Structure-transport correlation for the diffusive tortuosity of bulk, monodisperse, random sphere packings. *Journal of Chromatography A*, **1218**: 6489–6497, 2011. (see pp. 48, 49)

[82] ROBERT E BECK & JEROME S SCHULTZ. Hindrance of solute diffusion within membranes as measured with microporous membranes of known pore geometry. *Biochimica et Biophysica Acta*, **255**: 273–3, 1972. (see p. 50)

[83] EUGENE M RENKIN. Filtration, diffusion, and molecular sieving through porous cellulose membranes. *Journal of General Physiology*, **38**: 225–243, 1954. (see p. 50)

[84] M. P. BOHRER, GARY D. PATTERSON, & P. J. CARROLL. *Hindered Diffusion of Dextran and Ficoll in Microporous Membranes*. **volume** 17 1984. 1170–1173 (see p. 50)

[85] CHARLES N. SATTERFIELD, CLARK K. COLTON, & WAYNE H. PITCHER. Restricted diffusion in liquids within fine pores. *AIChE Journal*, **19**: 628–635, 1973. (see p. 50)

[86] JADER ALEAN, JUAN C. MAYA, & FARID CHEJNE. Mathematical model for the mass transport in multiple porous scales. *Journal of Food Engineering*, **233**: 28–39, 2018. (see p. 50)

[87] C.E. BAUKAL, V. GERSHTEIN, & X.J. LI. *Computational Fluid Dynamics in Industrial Combustion*. Industrial Combustion Taylor & Francis, 2000. (see p. 50)

[88] J. E. JONES. On the Determination of Molecular Fields. II. From the Equation of State of a Gas. *Proceedings of the Royal Society A: Mathematical, Physical and Engineering Sciences*, **106**: 463–477, 1924. (see p. 51)

[89] O. REYNOLDS. On the Dynamical Theory of Incompressible Viscous Fluids and the Determination of the Criterion. *Philosophical Transactions of the Royal Society A: Mathematical, Physical and Engineering Sciences*, **186**: 123–164, 1895. (see p. 53)

[90] DON S. LEMONS & ANTHONY GYTHIEL. Paul Langevin's 1908 paper - On the Theory of Brownian Motion - [Sur la théorie du mouvement brownien, C. R. Acad. Sci. (Paris) 146 , 530-533 (1908)]. *American Journal of Physics*, **65**: 1079–1081, 1997. (see p. 54)

[91] P. A. M. DIRAC. Bakerian Lecture. The Physical Interpretation of Quantum Mechanics. *Proceedings of the Royal Society A: Mathematical, Physical and Engineering Sciences*, **180**: 1–40, 1942. (see p. 57)

[92] MARK BURGIN. *Extended probabilities: mathematical foundations*. arXiv, 2009. (see p. 57)

[93] ETHAN A. MASTNY, ERIC L. HASELTINE, & JAMES B. RAWLINGS. Two classes of quasi-steady-state model reductions for stochastic kinetics. *The Journal of Chemical Physics*, **127**: 094106, 2007. (see p. 58)

[94] STEFAN BECKER, HERBERT M. URBASSEK, MARTIN HORSCH, & HANS HASSE. Contact Angle of Sessile Drops in Lennard-Jones Systems. *Langmuir*, **30**: PMID: 25329011, 13606–13614, 2014. (see p. 58)

[95] MICHAELA HEIER, SIMON STEPHAN, JINLU LIU, WALTER G. CHAPMAN, HANS HASSE, & KAI LANGENBACH. Equation of state for the Lennard-Jones truncated and shifted fluid with a cut-off radius of 2.5σ based on perturbation theory and its applications to interfacial thermodynamics. *Molecular Physics*, **116**: 2083–2094, 2018. (see p. 58)

[96] JADRAN VRABEC, GAURAV KUMAR KEDIA, GUIDO FUCHS, & HANS HASSE. Comprehensive study of the vapour-liquid coexistence of the truncated and shifted Lennard-Jones fluid including planar and spherical interface properties. *Molecular Physics*, **104**: 1509–1527, 2006. (see p. 58)

[97] A.B. ABELL, K.L. WILLIS, & D.A. LANGE. Mercury Intrusion Porosimetry and Image Analysis of Cement-Based Materials. *Journal of Colloid and Interface Science*, **211**: 39–44, 1999. (see pp. 59, 60)

[98] W. C. CONNER, J. F. CEVALLOS-CANDAU, E. L. WEIST, J. PAJARES, S. MENDIOROZ, & A. CORTES. Characterization of pore structure: porosimetry and sorption. *Langmuir*, **2**: 151–154, 1986. (see pp. 59, 60)

[99] Siarhei Khirevich, Alexandra Höltzel, & Ulrich Tallarek. Validation of Pore-Scale Simulations of Hydrodynamic Dispersion in Random Sphere Packings. *Communications in Computational Physics*, **13**: 801–822, 2013. (see p. 61)

[100] Siarhei Khirevich. High-Performance Computing of Flow, Diffusion, and Hydrodynamic Dispersion in Random Sphere Packings. *PhD Thesis*, 159, 2011. (see p. 61)

[101] Hamed Eghbali, Vincent Verdoold, Lieselot Vankeerberghen, Han Gardeniers, & Gert Desmet. Experimental investigation of the band broadening arising from short-range interchannel heterogeneities in chromatographic beds under the condition of identical external porosity. *Analytical Chemistry*, **81**: 705–715, 2009. (see p. 61)

[102] M. Sahimi. *Flow and Transport in Porous Media and Fractured Rock: From Classical Methods to Modern Approaches*. Wiley, 2011. (see p. 63)

[103] Donald L. Koch & John F. Brady. Dispersion in fixed beds. *Journal of Fluid Mechanics*, **154**: 399–427, 1985. (see p. 63)

[104] Anton Daneyko, Dzmitry Hlushkou, Vasili Baranau, Siarhei Khirevich, Andreas Seidel-Morgenstern, & Ulrich Tallarek. Computational investigation of longitudinal diffusion, eddy dispersion, and trans-particle mass transfer in bulk, random packings of core-shell particles with varied shell thickness and shell diffusion coefficient. *Journal of Chromatography A*, **1407**: 139–156, 2015. (see p. 65)

[105] Jorge M. Ramirez, Enrique A. Thomann, Edward C. Waymire, Juliette Chastanet, & Brian D. Wood. A note on the theoretical foundations of particle tracking methods in heterogeneous porous media. *Water Resources Research*, **44**: 2008. (see p. 65)

[106] Aurina Martínez Arias & Alfred P. Weber. Aerosol synthesis of porous SiO_2-cobalt-catalyst with tailored pores and tunable metal particle size for Fischer-Tropsch synthesis (FTS). *Journal of Aerosol Science*, **131**: 1–12, 2019. (see pp. 65, 71, 73)

[107] Vasili Baranau, Dzmitry Hlushkou, Siarhei Khirevich, & Ulrich Tallarek. Pore-size entropy of random hard-sphere packings. *Soft Matter*, **9**: 3361, 2013. (see p. 66)

[108] Linda S. Cheng & Yang Ralph T. Improved Horváth-Kawazoe equations including spherical pore models for calculating micropore size distribution. *Chemical Engineering Science*, **49**: 2599–2609, 1994. (see p. 66)

[109] Salil U. Rege & Ralph T. Yang. Corrected Horváth-Kawazoe equations for pore-size distribution. *AIChE Journal*, **46**: 734–750, 2000. (see p. 66)

[110] Poul L Hansen, Jakob B Wagner, Stig Helveg, Jens R Rostrup-Nielsen, Bjerne S Clausen, & Henrik Topsøe. Atom-Resolved Imaging of Dynamic Shape Changes in Supported Copper Nanocrystals. *Science*, **295**: 2053–2055, 2002. (see pp. 71, 73)

[111] Junwei Wang, Chrameh Fru Mbah, Thomas Przybilla, Benjamin Apeleo Zubiri, Erdmann Spiecker, Michael Engel, & Nicolas Vogel. Magic number colloidal clusters as minimum free energy structures. *Nature Communications*, **9**: 2018. (see pp. 73–76, 116, 117)

[112] Bart De Nijs, Simone Dussi, Frank Smallenburg, Johannes D Meeldijk, Dirk J Groenendijk, Laura Filion, Arnout Imhof, Alfons Van Blaaderen, & Marjolein Dijkstra. Entropy-driven formation of large icosahedral colloidal clusters by spherical confinement. *Nature Materials*, **14**: 56–60, 2015. (see pp. 73, 75, 76, 117)

[113] Adolfo J. Banchio, Marco Heinen, Peter Holmqvist, & Gerhard Nägele. Short- and long-time diffusion and dynamic scaling in suspensions of charged colloidal particles. *Journal of Chemical Physics*, **148**: 134902, 2018. (see pp. 73, 74, 83, 90, 91)

[114] BRIAN GIERA, LUIS A. ZEPEDA-RUIZ, ANDREW J. PASCALL, & TODD H. WEISGRABER. Mesoscale Particle-Based Model of Electrophoretic Deposition. *Langmuir*, **33**: 652–661, 2016. (see pp. 74, 117)

[115] A. IMHOF, A VAN BLAADEREN, G MARET, J MELLEMA, & J. K.G. DHONT. A comparison between the long-time self-diffusion and low shear viscosity of concentrated dispersions of charged colloidal silica spheres. *Journal of Chemical Physics*, **100**: 2170–2181, 1994. (see pp. 74, 78)

[116] AMIT KUMAR & JONATHAN J.L. HIGDON. Origins of the anomalous stress behavior in charged colloidal suspensions under shear. *Physical Review E - Statistical, Nonlinear, and Soft Matter Physics*, **82**: 051401, 2010. (see pp. 74, 88)

[117] JEFFREY F. MORRIS & JOHN F. BRADY. Self-diffusion in sheared suspensions. *Journal of Fluid Mechanics*, **312**: 223–252, 1996. (see p. 74)

[118] THANH N. PHUNG, JOHN F. BRADY, & GEORGES BOSSIS. Stokesian dynamics simulation of Brownian suspensions. *Journal of Fluid Mechanics*, **313**: 181–207, 1996. (see pp. 74, 88)

[119] DAVID R. FOSS & JOHN F. BRADY. Self-diffusion in sheared suspensions by dynamic simulation. *Journal of Fluid Mechanics*, **401**: 243–274, 1999. (see pp. 74, 88)

[120] N KOUMAKIS, M LAURATI, S U EGELHAAF, J F BRADY, & G PETEKIDIS. Yielding of hard-sphere glasses during start-up shear. *Physical Review Letters*, **108**: 2012. (see p. 74)

[121] SHENGFENG CHENG & GARY S GREST. Molecular dynamics simulations of evaporation-induced nanoparticle assembly. *Journal of Chemical Physics*, **138**: 64701, 2013. (see p. 74)

[122] N. KOUMAKIS, M. LAURATI, A. R. JACOB, K. J. MUTCH, A. ABDELLALI, A. B. SCHOFIELD, S. U. EGELHAAF, J. F. BRADY, & G. PETEKIDIS. Start-up shear of concentrated colloidal hard spheres: Stresses, dynamics, and structure. *Journal of Rheology*, **60**: 603–623, 2016. (see p. 74)

[123] CARSTEN SCHILDE & ARNO KWADE. Measurement of the micromechanical properties of nanostructured aggregates via nanoindentation. *Journal of Materials Research*, **27**: 672–684, 2012. (see pp. 74, 75)

[124] J. BRADY & GOERGES. BOSSIS. Stokesian Dynamics. *Annual Review of Fluid Mechanics*, **20**: 111–157, 1988. (see pp. 74, 88)

[125] MORTON M. DENN, JEFFREY F. MORRIS, & DANIEL BONN. Shear thickening in concentrated suspensions of smooth spheres in Newtonian suspending fluids. *Soft Matter*, **14**: 170–184, 2018. (see p. 74)

[126] H.E. BERGNA & W.O. ROBERTS. *Colloidal Silica: Fundamentals and Applications*. Surfactant Science CRC Press, 2005. (see p. 76)

[127] S JENKINS, S R KIRK, M PERSSON, J CARLEN, & Z ABBAS. Molecular dynamics simulation of nanocolloidal amorphous silica particles : Part I. *Journal of Chemical Physics*, **224711**: 174704, 2007. (see p. 76)

[128] VALENTINA VALMACCO, MAGDALENA ELZBIECIAK-WODKA, CÉLINE BESNARD, PLINIO MARONI, GREGOR TREFALT, & MICHAL BORKOVEC. Dispersion forces acting between silica particles across water: Influence of nanoscale roughness. *Nanoscale Horizons*, **1**: 325–330, 2016. (see p. 76)

[129] FIONA A WIGZELL & S. DAVID JACKSON. The genesis of supported cobalt catalysts. *Applied Petrochemical Research*, **7**: 9–21, 2017. (see p. 80)

[130] ALEXANDER STUKOWSKI. Structure identification methods for atomistic simulations of crystalline materials. *Modelling and Simulation in Materials Science and Engineering*, **20**: 045021, 2012. (see p. 84)

[131] SITI MACHMUDAH, WAHYUDIONO, HIDEKI KANDA, & MOTONOBU GOTO. *Hydrolysis of Biopolymers in Near-Critical and Subcritical Water*. Elsevier Inc., 2017. 69–107 (see pp. 84, 86)

[132] SAMUEL H. MARON & PERCY E. PIERCE. Application of ree-eyring generalized flow theory to suspensions of spherical particles. *Journal of Colloid Science*, **11**: 80–95, 1956. (see p. 84)

[133] PETER HOLMQVIST & GERHARD NÄGELE. Long-Time dynamics of concentrated charge-stabilized colloids. *Physical Review Letters*, **104**: 2010. (see p. 86)

[134] CIGDEM O METIN, LARRY W LAKE, CAETANO R. MIRANDA, & QUOC P. NGUYEN. Stability of aqueous silica nanoparticle dispersions. *Journal of Nanoparticle Research*, **13**: 839–850, 2011. (see p. 86)

[135] STACEY HARPER, REGHAN J. HILL, JOHN RUMBLE, CHRISTINE OGILVIE HENDREN, FRED KLAESSIG, PHILIP SAYRE, ULF NOBBMANN, ALAN F. RAWLE, & GREGORY V. LOWRY. Guidance to improve the scientific value of zeta-potential measurements in nanoEHS. *Environmental Science: Nano*, **3**: 953–965, 2016. (see pp. 86, 92, 93)

[136] MICHAEL DEAN BYBEE. *Hydrodynamic Simulations of Colloidal Gels: Microstructure, Dynamics, and Rheology*. Ph.D. dissertation. University of Illinois at Urbana-Champaign, 2003. (see p. 88)

[137] AMIT KUMAR. *Microscale dynamics in suspensions of non-spherical particles*. Ph.D. dissertation. University of Illinois at Urbana-Champaign, 2010. (see p. 88)

[138] R EVERAERS & M R EJTEHADI. Interaction potentials for soft and hard ellipsoids. *Physical Review E - Statistical Physics, Plasmas, Fluids, and Related Interdisciplinary Topics*, **67**: 8, 2003. (see p. 89)

[139] K. DILL & S. BROMBERG. *Molecular Driving Forces: Statistical Thermodynamics in Biology, Chemistry, Physics, and Nanoscience*. CRC Press, 2012. (see p. 89)

[140] JIN SI ZHANG, XI ZHANG, ZHONG LIANG ZHANG, & ZHI JIE TAN. Potential of mean force between oppositely charged nanoparticles: A comprehensive comparison between Poisson-Boltzmann theory and Monte Carlo simulations. *Scientific Reports*, **7**: 2017. (see p. 89)

[141] H.J. BUTT, M.K.H.J.B. KARLHEINZ GRAF, H.J.B. BUTT, K. GRAF, K. GRAF, & M. KAPPL. *Physics and Chemistry of Interfaces*. Physics textbook Wiley, 2003. (see p. 89)

[142] K S SCHMITZ, ARUP K MUKHERJEE, & L B BHUIYAN. Screened Coulomb Pair Potential in Colloidal Interactions in Suspensions Revisited. *The Journal of Physical Chemistry B*, **107**: 10040–10047, 2003. (see p. 90)

[143] ZHIHONG NIE, ALLA PETUKHOVA, & EUGENIA KUMACHEVA. Properties and emerging applications of self-assembled structures made from inorganic nanoparticles. *Nature Nanotechnology*, **5**: 15–25, 2010. (see pp. 95, 97)

[144] C. STEPHENSON & A. HUBLER. Stability and conductivity of self assembled wires in a transverse electric field. *Scientific Reports*, **5**: 15044, 2015. (see pp. 95, 97)

[145] KIWOONG LEE, HOSEOP CHOI, DAE SEONG KIM, MIN SEOK JANG, & MANSOO CHOI. Vertical stacking of three-dimensional nanostructures via an aerosol lithography for advanced optical applications. *Nanotechnology*, **28**: 475302, 2017. (see pp. 95, 97, 103)

[146] MAREK GRZELCZAK, JAN VERMANT, ERIC M. FURST, & LUIS LIZ-MARZÁN. Directed Self-Assembly of Nanoparticles. *ACS Nano*, **4**: 3591–3605, 2010. (see p. 97)

[147] DAVID LYON & ALFRED HUBLER. Gap size dependence of the dielectric strength in nano vacuum gaps. *IEEE Transactions on Dielectrics and Electrical Insulation*, **20**: 1467–1471, 2013. (see p. 97)

[148] ALFRED W. HÜBLER & ONYEAMA OSUAGWU. Digital quantum batteries: Energy and information storage in nanovacuum tube arrays. *Complexity*, **15**: 2010. (see p. 97)

[149] N D Denkov, D Velev, P A Kralchevsky, I B Ivanov, +j H Yoshimura, & K Nagayamat. Mechanism of Formation of Two-Dimensional Crystals from Latex Particles on Substrates. *Langmuir*, **8**: 3183–3190, 1992. (see p. 97)

[150] Alexander Böker, Jinbo He, Todd Emrick, & Thomas P Russell. Self-assembly of nanoparticles at interfaces. *Soft Matter*, **3**: 1231, 2007. (see p. 97)

[151] W. Benjamin Rogers, William M. Shih, & Vinothan N. Manoharan. Using DNA to program the self-assembly of colloidal nanoparticles and microparticles. *Nature Reviews Materials*, **1**: 16008, 2016. (see p. 97)

[152] Slavko Kralj & Darko Makovec. Magnetic Assembly of Superparamagnetic Iron Oxide Nanoparticle Clusters into Nanochains and Nanobundles. *ACS Nano*, **9**: 9700–9707, 2015. (see p. 97)

[153] Hoseop Choi & Mansoo Choi. Process for producing 3-dimensional structure assembled from nanoparticles. *US Patent*, US9321633B2, 2014. (see p. 98)

[154] Hoseop Choi, Seunghyon Kang, Wooik Jung, Yoon ho Jung, Sei Jin Park, Dae Seong Kim, & Mansoo Choi. Controlled electrostatic focusing of charged aerosol nanoparticles via an electrified mask. *Journal of Aerosol Science*, **88**: 90–97, 2015. (see pp. 98, 103)

[155] Cedric Boissiere, David Grosso, Alexandra Chaumonnot, Lionel Nicole, & Clement Sanchez. Aerosol route to functional nanostructured inorganic and hybrid porous materials. *Advanced Materials*, **23**: 599–623, 2011. (see p. 98)

[156] Nathan E Motl, Amanda K P Mann, & Sara E Skrabalak. Aerosol-assisted synthesis and assembly of nanoscale building blocks. *Journal of Materials Chemistry A*, **1**: 5193–5202, 2013. (see p. 98)

[157] Sukbeom You & Mansoo Choi. Numerical simulation of microscopic motion and deposition of nanoparticles via electrodynamic focusing. *Journal of Aerosol Science*, **38**: 1140–1149, 2007. (see p. 98)

[158] Sukbeom You, Kyuhee Han, Hyoungchul Kim, Heechul Lee, Chang Gyu Woo, Changui Jeong, Woongsik Nam, & Mansoo Choi. High-resolution, parallel patterning of nanoparticles via an ion-induced focusing mask. *Small*, **6**: 2146–2152, 2010. (see p. 98)

[159] Hyoungchul Kim, Jaehyun Kim, Hongjoo Yang, Jeongsoo Suh, Taeyoung Kim, Bangwoo Han, Sungwon Kim, Dae Seongkim, Peter V. Pikhitsa, & Mansoo Choi. Parallel patterning of nanoparticles via electrodynamic focusing of charged aerosols. *Nature Nanotechnology*, **1**: 117–121, 2006. (see p. 98)

[160] I.S. Grant & W.R. Phillips. *Electromagnetism*. Manchester Physics Series Wiley, 2013. (see p. 103)

[161] M.S. Sethi & M. Satake. *Chemical Bonding*. Discovery Publishing House, 2010. (see p. 104)

[162] J.S. Rigden. *Macmillan Encyclopedia of Physics: A-D*. Simon & Schuster Macmillan, 1996. (see p. 105)

[163] Vinothan N. Manoharan. Colloidal matter: Packing, geometry, and entropy. *Science*, **349**: 1253751–1253751, 2015. (see pp. 116, 117)

[164] M. Chaudhuri, E. Allahyarov, H. Löwen, S. U. Egelhaaf, & D. A. Weitz. Triple Junction at the Triple Point Resolved on the Individual Particle Level. *Physical Review Letters*, **119**: 2017. (see p. 116)

[165] Triantafyllos Stylianopoulos, Ming-Zher Poh, Numpon Insin, Moungi G Bawendi, Dai Fukumura, Lance L Munn, & Rakesh K Jain. Diffusion of Particles in the Extracellular Matrix: The Effect of Repulsive Electrostatic Interactions. 2010. (see p. 119)

Curriculum Vitae

Hector Fernando Rusinque Olaya
from Bogota, Colombia

Education

2017–2020	**PhD** Technische Universität Clausthal, Clausthal-Zellerfeld Germany Main topics: Computational fluid and particle dynamics simulations
10.2014–2016	**Master of Science in Process Engineering/Chemical Engineering** Technische Universität Clausthal, Clausthal-Zellerfeld , Germany Specialization: Chemical Processes
2011–2013	**Bachelor of Engineering in Chemical Engineering** Hochschule München, Munich, Germany
2009–2010	**German Courses: Elementary, intermediate and advanced level** Karlsruher Institut für Technologie, Karlsruhe, Germany

Work and research experience

Since 10.2020	**R&D Engineer** Sympatec GmbH, Clausthal-Zellerfeld, Germany Further development of imaging methods for particle characterization, management of development projects.
2017-2020	**PhD Candidate** Technische Universität Clausthal Doctoral studies with the main topic on the simulation of brownian particles in external fields at the Institute of Applied Mechanics.
06–12.16	**Master Thesis** Technische Universität Clausthal Master thesis with the topic "Pore-resolved calculation of dispersion and diffusion in inhomogeneous porous media" at the Institute of Applied Mechanics.